DEVELOPMENT AND APPLICATION OF A GENERIC FINITE VOLUME MULTIPHASE FLOW SOLVER FOR GAS-PARTICULATE FLOWS

A thesis submitted in partial fulfilment of the requirements
for the degree of

DOCTOR OF PHILOSOPHY

by

SUBRAT KOTOKY
Roll No: 126103008

DEPARTMENT OF MECHANICAL ENGINEERING
INDIAN INSTITUTE OF TECHNOLOGY GUWAHATI
GUWAHATI - 781 039

July, 2018

CERTIFICATE

It is certified that the work contained in the thesis entitled **"Development and Application of a Generic Finite Volume Multiphase Flow Solver for Gas-Particulate Flows"**, by **Subrat Kotoky** has been carried out under our supervision and that this work has not been submitted elsewhere for a degree.

(Amaresh Dalal)
Associate Professor
Department of Mechanical Engineering
Indian Institute of Technology Guwahati

(Ganesh Natarajan)
Associate Professor
Department of Mechanical Engineering
Indian Institute of Technology Guwahati

July 2018

ABSTRACT

Multiphase flow is the simultaneous flow of two or more interacting phases, where the interaction is influenced by the relative motion of the phases. Gas-particulate flow constitutes a class of two phase flows that involve a continuous gas phase and non-evaporating particles. The gas and particle phases are thoroughly mixed with each other in all parts of the flow domain and are not separated by a distinct interface. Such flows are ubiquitous both in nature and industry and find applications in gas-solid fluidized beds, pulverised coal fired combustion systems, powder metallurgy and solid transportation systems etc.

The Eulerian-Eulerian approach is commonly used for numerical modeling of gas-particle flows. In this approach, the properties of the dispersed particle phase are assumed to be continuous like those of the continuous gas phase. The particle phase is solved using fluid-like equations and the interaction between the two phases is taken care by implementing exchange-coefficients which are often calculated empirically. This treatment of handling the particle phase as a whole instead of tracking each particle in the domain makes this approach computationally less expensive.

The present doctoral thesis focuses on the development of a generic finite volume based numerical solver to simulate gas-particle flows using Eulerian-Eulerian two fluid model on collocated grid arrangement. The solver which is capable of handling both orthogonal and non-orthogonal meshes in an efficient manner has been indigenously developed with an emphasis on application to problems involving gas-particle flows. A detailed description of the convective and diffusive flux discretizations are provided as also the descriptions of the drag model and coupling approaches. Validations have been performed for one-way and two-way coupling for dilute flow conditions in the initial phase of the work. Subsequently, the solver is modified to handle non-dilute flows as well as to account for particle-particle and particle wall interactions using the kinetic theory for granular flows (KTGF) model. Two major concerns in numerical implementation of such complex flows pertain to the pressure equation and particle packing limit. The pressure equation for the two-fluid model is derived from the global continuity equation which is obtained by

adding the continuity equations of both the phases. For some practical applications like gas-solid bubbling fluidized beds where the particle volume fraction exceeds a certain critical value and close to the maximum packing limit, the flow physics is dominated mainly by the frictional stresses and KTGF alone is not sufficient to adequately describe the flow. For such cases, frictional stress models are incorporated along with the KTGF model into the flow solver. A detailed validation at all stages of development (including comparisons from Ansys Fluent and OpenFoam) for different problems available in the literature are performed and the results show a reasonably good agreement with the published data.

The flow solver is subsequently applied for parametric studies in three different scenarios and finally applied to the case of bubbling gas-solid fluidized beds. In the first study, a complete parametric study of dispersed laminar gas-particle flows has been carried out assuming a two-way coupling between the phases. This study focuses on the effects of particle diameter (Stokes number), particle phase material density, inlet particle phase volume fraction and inlet slip (or difference of phase velocities at inlet) on the overall flow hydrodynamics of dispersed gas-particle flows. Simulations have been carried out for a wide range of volume fractions of the dispersed phase which varies from a very low value (dilute range) to a moderately high value (dispersed range) and a wide range of particle diameters (Stokes number) in horizontal and vertical channels. Studies reveal that the maximum value of steady state velocity attained by the particle phase inside the domain decreases while that of the gas phase increases with increase in particle Stokes number. Investigations are also carried out to understand the effects of inlet slip (or difference of phase velocities at inlet) on the flow physics inside a horizontal channel which have not been previously studied in detail. Scenarios where the gas inlet velocity is greater than the particle inlet velocity and vice-versa are studied and it is observed that significant changes occur in both phase velocities as well as volume fraction profiles from the flow situation where both the phases enter the domain with the same inlet velocity.

The second study discusses the effects of particle-wall (quantified by specularity coefficient ϕ) and particle-particle (quantified by restitution coefficient e) interactions on the flow hydrodynamics of dispersed gas-particle flows through horizontal channels. Such investigations have also been limited as also discussions on the consequent effects of variations of these two parameters on the phase velocities, volume fractions as well as on the wall shear stress profiles. It has been found that at a particular value of e, both gas and particle velocities at the centerline of the channel increase with increase in the value of ϕ, whereas near the wall, they tend to decrease. At a fixed non-zero value of ϕ, both gas and particle velocities tend to increase with increase in the value of e. But for ϕ equal to zero (which corresponds to free-slip boundary condition for particle velocity), there is no significant variations in gas and particle velocities with changes in e. Numerical simulations also reveal that the

value of average wall shear stress for the particle phase increases with increase in the value of ϕ whereas, for the gas phase, it decreases with increase in the value of ϕ. These insights into the flow hydrodynamics could be valuable for practical situations such as pneumatic conveying.

The third study discussed in this thesis relates to the effects of particle-wall and particle-particle interactions on the recirculation characteristics of dispersed gas-particle flows through a sudden expansion. While there have been reports that the numerical simulations of dispersed gas-particle flows through a sudden expansion carried out assuming particle-particle interactions show closer agreement with experimental results, there have been very few studies which quantitatively examine the effects of both particle-particle and particle-wall interactions on the recirculation characteristics of dispersed gas-particle flows through a sudden expansion. The stretching or shrinking of recirculation zone with changes in the values of e and ϕ could be vital in the design of gas-solid separators, air filters, combustors and diffusers where there exists a distinct possibility of flow separation. Investigations from this study reveal that particle-particle interactions,quantified by restitution coefficient (e) have a greater impact on recirculation characteristics than particle-wall interactions, which are quantified by specularity coefficient (ϕ). Studies also reveal that the recirculation lengths tend to decrease as particle collisions become more elastic (as e tends to unity) while they increase, as the value of ϕ increases. However, the changes in recirculation length is very gradual and less pronounced when only particle-wall interactions are considered as compared to particle-particle interactions. From the range of parametric variations studied in this work, the maximum recirculation length has been found when the value of ϕ is maximum and that of e is minimum.

The last problem discussed in this thesis is the simulation of gas-solid bubbling fluidized bed. After carrying out extensive validations and thorough parametric studies using the developed solver, the more complex but practical problem of bubbling fluidized beds is considered. Simulations are performed for idealized two-dimensional fluidized beds and the results comparing well with previous computational and experimental work. Simulations are performed to study the effects of particle diameter on the fluidization characteristics keeping all other parameters invariant. Significant changes in the time-averaged velocity and volume fraction profiles have been observed with change in the particle diameter.

The thesis presents a comprehensive numerical framework for gas-particulate flows on unstructured meshes which is an indigenous contribution to the field. The thesis concludes with a summary of works carried out and recommendations for future work with emphasis on practical three-dimensional applications.

Dedicated to Pita and Ma

Acknowledgements

If I would have worked single-handedly on the research reported in this thesis, I would have never been able to complete it. Herein, I would like to acknowledge all those who have helped me in various ways during my doctoral study at Indian Institute of Technology, Guwahati.

First and foremost, I would like to express my sincere gratitude to my supervisors, Dr. Amaresh Dalal and Dr. Ganesh Natarajan for their invaluable guidance, continuous motivation and sagacious advice during my thesis work. Their insightful constant monitoring has immensely helped me to carry out my research. I shall always be grateful to them for devoting a large share of their valuable time and knowledge into this work. I am thankful for their kind and amicable behavior which has always been very inspiring.

I would also like to express my sincere gratitude and humble respect to my doctoral committee members: Dr. Niranjan Sahoo, Dr. Arnab Kumar De and Dr. Anugrah Singh for their suggestions and insightful comments on my work. My special thanks goes to the faculty members of the department of Mechanical Engineering from whom I learnt the basics of fluids and thermal engineering. Specially, the advanced course on CFD taught by Dr. Arnab Kumar De was very helpful for me in learning how to write CFD codes which helped in pursuing my research. I am also thankful to Dr. Pankaj Saha from NETL, USA and Dr. Vikrant Verma from Technical University, Delft Netherlands for a fruitful discussion during the course of my work. I also extend my thanks to the individuals in the Department who have helped me one way or another. In addition to this, I would also like to acknowledge the partial funding provided by DAE-BRNS, Government of India.

These acknowledgements would not be complete without mentioning my research lab colleagues Saurabh, Mukul, Preetirekha, Vinod, Mayank and all the present and passed out M.Tech. students of our Anupravaha Laboratory. It was really a great pleasure working with all of them and I thank all of them for their support. Special thanks goes to my seniors Dr. Pitambar Randive, Dr. Sathisha H. M. and Dr. Jai Manik for helping me in learning things required for my work. I would also like to take this opportunity to thank Mrs. Soumita Dalal for providing us a homely atmosphere here in the IITG Campus away from home.

I am grateful to my friends Kiran Saikia, Seim Timung, Ashim Malakar, Bhaskar jyoti Sharma, Mriganka Borah, Shuvra Shankar Kalita, Hiranya Deka who always gave me time, company and help during my stay in the IIT Guwahati campus. I am also thankful to my friends Indranuj Khound and Amlan Jyoti Chakravorty who always remained in touch and motivated me to do my work. I would also take this opportunity to thank Anirban Goswami, Sushree Shila P. Goswami, Dr. Sidananda

Sarma and Mrs. Lavita Sarma for their love and affection and for helping me whenever I needed.

Finally, I would like to say that this work would not have been possible without the blessings of the Almighty and the constant support of my family members. Specially my parents, for whom I think whatever I do will be less compared to the support, good wishes and blessings they have bestowed upon me. Thanks will be a very small word for acknowledging them. I express my gratitude to Papu da, Sum ba, Kiku da, Rajib da, Junjun bou, Babu da, Ron, Mon, Gungun and Aalful for their love and continuous support. I am also thankful to my grandparents, uncles and aunts for their constant blessings and motivations.

Subrat Kotoky

Contents

List of Figures

List of Tables

Nomenclature

English Symbols

Symbol	Definition
C_d	Drag coefficient
C_{LR}	Lift coefficient due to rotation
d_s	Particle diameter
$\overline{\overline{D}}_s$	Viscous stress tensor of solid phase velocity
e	Particle-particle restitution coefficient
$\mathbf{g}$	Gravitational vector
$\mathbf{F}_l$	Lift force
$\mathbf{F}_{mag}$	Magnus force
$\mathbf{F}_{vm}$	Vietual mass force
g_0	Radial distribution function
k_g	Turbulent kinetic energy for gas phase
K_{gs}	Interphase momentum exchange coefficient
L_s	Characteristic length of a system.
$\dot{m}$	Mass flow rate
p	Hydrodynamic pressure
p_s	Solid pressure
$q_{\theta,s}$	Granular energy flux
Re	Gas phase Reynolds number
Re_p	Particle Reynolds number
$\mathbf{S}_f$	Surface area vector
St	Particle Stokes number
t	Time
Δt	Time step
u, v, w	Velocity components in x, y, z directions
$\mathbf{u}$	Velocity vector
ΔV	Volume of a cell
x, y, z	Cartesian coordinates
$\mathbf{x}$	Position vector
$\hat{\mathbf{x}}$	Unit vector

Greek Symbols

Symbol	Definition
α	Volume fraction
$\alpha_{s,max}$	Packing limit
$\alpha_{s,min}$	Minimum volume fraction
ϵ	Rate of dissipation of turbulent kinetic energy
θ	Granular temperature of the particle phase

κ	Granular conductivity of the solid phase
λ	Solid phase bulk viscosity
μ_g	Dynamic viscosity of the gas phase
μ_s	Solid phase shear viscosity
ν_g	Kinematic viscosity of the gas phase
ρ	Material density of a phase
τ	Shear stress
τ_f	Characteristic fluid time scale
τ_p	Particle relaxation time
ϕ	Specularity coefficient

Subscripts

Symbol	Definition
co	Value of cell centroid of owner cell
f	Value at a face of a cell
g	Gas phase
nb	Value of cell centroid of neighbor cell
s	Particle phase

Superscripts

Symbol	Definition
$n, n+1$	Time levels
*	Intermediate time level between n and $n+1$

Abbreviations

Symbol	Definition
CDS	Central Difference Scheme
CFD	Computational Fluid Dynamics
$CGNS$	CFD General Notation System
FVM	Finite Volume Method
$KTGF$	Kinetic Theory for Granular Flows
LIS	Library of Iterative Solvers
$SIMPLE$	Semi-Implicit Method for Pressure Linked Equations
UDS	Upwind Scheme

Chapter 1

Introduction

Multiphase flow is the simultaneous flow of two or more interacting phases, where the interaction is influenced by the relative motion of the phases. Two phase flow is the simplest case of multiphase flows. The subject of two phase flow is very important in a number of engineering systems like power systems (such as nuclear reactors), heat transfer systems (such as heat exchangers, spray cooling towers, dryers), process systems (such as chemical reactors, fluidized beds), transport systems (such as air-lift pump, pipeline transport of gas and oil mixtures, pulverised solid particles) and many other applications for their optimum design and safe operations. The existence of two phase flows can be seen even in many natural and biological phenomena like sedimentation, soil erosion and transport by wind, formation and motion of rain droplets and many more.

1.1 Classification of two phase flows

There are different classifications of two phase flows suggested in the literature. But the more general classification is given by Ishii and Hibiki [1] which is based on constituents and topology of the flow. Based on the constituents of the flow, two phase flows are classified as

1. Gas-solid flow (flow of dust particles inside a room, fluidized beds)
2. Gas-liquid flow (bubbly flows, slug flows)
3. Solid-liquid flow (slurry flows, sediment transport)
4. Liquid-liquid (flow of immiscible liquids)

Based on the topology of the flow, two phase flows are classified as

1. Separated flow
2. Mixed or transitional flow
3. Dispersed flow

Separated two phase flows are the flows in which the two phases are separated by a distinct interface and are not mixed with each other. The typical regimes of this type of flows are shown in Fig. 1.1. Flow of two immiscible fluids like oil and water or air and water falls in this category.

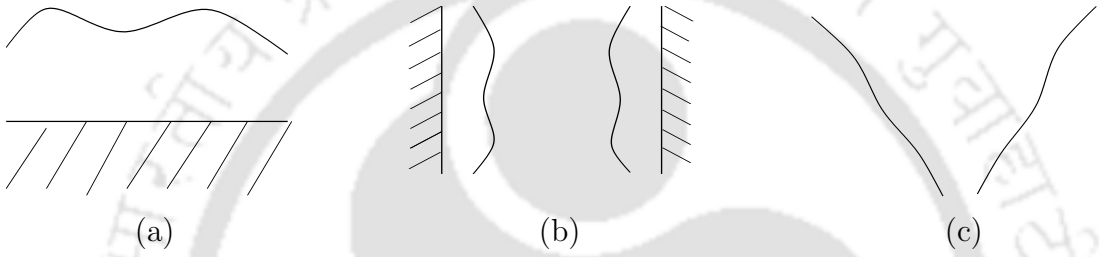

Figure 1.1: Separated flow, (a) film flow, (b) annular flow, (c) jet flow

In mixed or transitional flows, the two phases are not separated by a sharp interface in the entire flow domain. They may be mixed with each other in some or all parts of the domain. The typical regimes for this type of flows are shown in Fig. 1.2. This type of mixed flows may be observed in steam generators, boiling nuclear reactor channels etc.

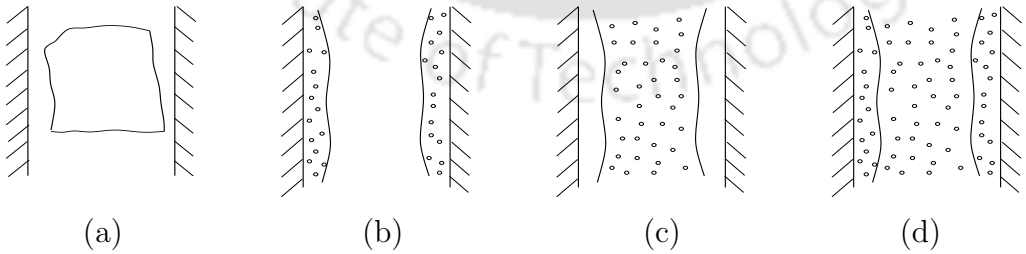

Figure 1.2: Mixed or transitional flow (a) slug flow, (b) bubbly annular flow, (c) droplet annular flow, (d) bubbly droplet annular flow

Dispersed flows are characterized by the continuous and thorough mixing of both the phases with each other in all the parts of the flow domain and the two phases are not at all separated by any interface in any part of the domain. The typical regimes of this type of flows are given in Fig. 1.3. Examples of this type of flow can be observed in the flow of dust particles in air, spray cooling and in fluidized beds. Gas-particle flows, which is the topic of interest of this thesis, falls in the category of dispersed flows.

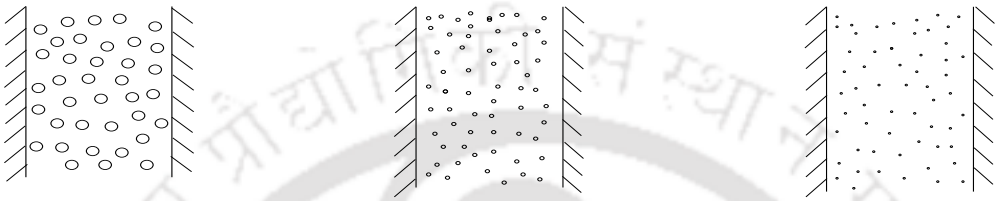

(a) (b) (c)

Figure 1.3: Dispersed flow, (a) bubbly flow, (b) droplet flow, (c) particulate flow

1.2 Study of two phase flow problems

The study of the problems involving two phase or multiphase flows has been going on both experimentally and numerically since decades. One of the first significant experimental works was carried out by Starkey [2] who carried out experiments to find out the trajectories of the suspended particles in a laminar stream of fluid through a horizontal tube. Since then, many other significant experimental works have been carried out by Booras et al. [3], Sinclair et al. [4], Kashinsky et al. [5], Nakoryakov et al. [6], Luo et al. [7] and Schindler et al. [8] in the field of two phase flows. On the other hand, in order to model two phase flows numerically, the following modeling approaches have been proposed.

- Homogeneous equilibrium model
- Drift flux model
- Two-fluid model

1.2.1 Homogeneous equilibrium model

In this model, the flow is analyzed by treating the mixture as a single fluid. The physical properties are represented by the average values of the mixture which are

calculated based on the properties of the constituents as well as the proportion of the constituents present in the mixture. Both the phases are assumed to possess the same velocity or in other words, the slip between the phases is neglected. This model is mathematically simpler and is generally applied in solving flows such as bubbly flow of water in air or flow of steam at high pressures.

1.2.2 Drift flux model

The drift flux model is similar to the homogeneous equilibrium model in all respects except that it considers the slip taking place between the phases in modeling a two phase flow problem. As a result, additional terms appear in the equations which make it somewhat complicated than the homogeneous equilibrium model. The homogeneous equilibrium model and the drift flux model are sometimes together referred to as mixture model.

1.2.3 Two-fluid model

The two-fluid model is formulated by considering each of the two constituting phases separately. In this model, the two phases have their own independent velocity fields and other physical properties. Hence, this model is expressed in terms of two sets of conservation equations governing the balance of mass, momentum and energy of each phase. The interaction between the phases is taken care of by introducing extra source terms known as exchange coefficients in the governing equations of both the phases. This model is more complicated than the mixture models in terms of the number of equations involved. But its real importance lies in the fact that it can take into account the dynamic and non-equilibrium interactions between the phases.

1.3 Gas-particle flow

Gas-particle flow falls in the category of dispersed flows in which the phases are thoroughly mixed with each other and are not separated by a sharp interface. In this class of flows, the interactions between the particle phase and gas phase play an important role in governing the physics of the flow [9]. The particle phase may be solid or non-evaporating liquid. Particles are called the dispersed phase and the

fluid in which the particles move is called the continuous phase.

Gas-particle flows are encountered in a variety of engineering applications as well as natural phenomena. In nature, flow of dust particles in atmospheric air is a typical example of gas-particle flow. In practical application fields, existence of gas-particle flows may be seen in gas-solid fluidized beds where the finely crushed coal particles consist the solid phase. Likewise, gas-particle flows are observed in pulverised coal fired combustion systems, powder metallurgy and solid transportation systems.

1.4 Basic terminology related to gas-particle flows

In this Section, the various terminology associated with gas-particulate flows have been discussed which will be extensively used in the current thesis. The important terms related to gas-particulate flows are discussed below.

1.4.1 Volume fraction (α)

As already mentioned, there is no distinct interface between the two phases in gas-particle flows and both the phases co-exist in all parts of the domain. Therefore, the concept of volume fraction is introduced which refers to the relative amount of each phase present in the flow domain. The volume fraction of a particular phase is defined as the ratio of volume occupied by that phase to the total volume under consideration. The volume fraction of a phase is mathematically represented as

$$\alpha = \lim_{\triangle V \to 0} \frac{\triangle V_p}{\triangle V}. \tag{1.1}$$

In this equation, α denotes the volume fraction of a particular phase, $\triangle V_p$ denotes the volume occupied by that particular phase in the volume under consideration and $\triangle V$ is the total volume under consideration occupied by the two phases together. Based on the volume fraction of the particle phase, gas-particle flows are classified to be dilute, dispersed or dense.

1.4.2 Phase coupling

In gas-particle flows, the interaction between the continuous gas phase and the dispersed particle phase is termed as phase coupling. The interaction between the

particle phase and the gas phase plays an important role in the overall hydrodynamics of this type of flows. 'One-way coupling' means that the particle phase is affected by the continuous gas phase, but there is no reverse effect. Generally, when the volume fraction is in the range of $10^{-4} - 10^{-3}$ [10, 11], the particles hardly have any effect on hydrodynamics of the continuous gas phase. So, a one-way coupling is enough for numerical modeling in such a situation. But as the volume fraction increases upto a range of 10^{-2}, the effects of particle phase on the gas should also be taken into consideration. This is referred to as 'two-way coupling' between the phases. Loth [12] suggested that the flow in this range can be considered as 'dilute' as the effects of particle-particle interactions are not significant. As in one-way and two-way coupling, particle-particle interactions are not considered, so the flow in this range can be considered as 'dilute'.

As the particle phase volume fraction further increases beyond 10^{-2}, particle-particle interactions gradually become significant. When the particle phase volume fraction is in the range of 0.1 or more, along with the mutual interaction between the phases, particle-particle interactions also become significant. This is referred to as 'three-way coupling'. The flow in this situation is considered as 'non-dilute' or 'dispersed' and often influenced by particle-particle and particle-wall interactions. Even at higher particle phase volume fraction close to 0.5, the hydrodynamics of the flow is mainly influenced by the frictional stresses generated due to the close packing of the particles. The flow under these conditions is termed as 'dense' and additional models are to be incorporated in order to take care of the frictional stresses.

1.4.3 Stokes number (St)

Another important parameter related to the hydrodynamics of gas-particle flows is the particle Stokes number. It is a dimensionless number corresponding to the behavior of the particles suspended in a fluid flow. Stokes number is defined as the ratio of characteristic particle relaxation time to the characteristic fluid time scale, i.e.,

$$St = \frac{\tau_p}{\tau_f} \tag{1.2}$$

where τ_p is the particle relaxation time defined as the time required by a particle falling from rest in a quiescent fluid to reach $(1 - 1/e)$ times of its terminal velocity,

where e is a mathematical constant whose value is approximately equal to 2.71828. τ_p is calculated as

$$\tau_p = \frac{\rho_s d_s^2}{18\mu_g} \tag{1.3}$$

where ρ_s is the density of the particle phase, μ_g is dynamic viscosity of the gas phase and d_s is the particle diameter. A macroscopic Stokes number can be defined when the fluid time scale τ_f is determined from the characteristic length (L_s) and the characteristic velocity (V_s) of the system under consideration, i.e.,

$$\tau_f = \frac{L_s}{V_s} \tag{1.4}$$

Hence, from Eqs. 1.3 and 1.4, we can mathematically define Stokes number as

$$St = \frac{\rho_s d_s^2 V_s}{18\mu_g L_s} \tag{1.5}$$

On the other hand, a microscopic Stokes number can be defined when the fluid time scale τ_f is calculated as a function of turbulence time scale [13] as

$$\tau_f = C\frac{k_g}{\epsilon_g} \tag{1.6}$$

where k_g is the gas-phase turbulent kinetic energy and ϵ_g is the dissipation rate of turbulent kinetic energy and C is a constant.

The Stokes number physically indicates how readily the particle phase responds to the changes in the gas phase flow field. Particles with Stokes number much smaller than unity tend to follow the gas phase streamlines and they quickly respond to the gas phase velocity fluctuations. But particles with Stokes number of the order unity have a higher inertia and their behavior is effected mostly by their initial velocity and gravitational forces. They tend to pass through the fluid without much deflection in their initial trajectories.

1.4.4 Particle-wall specularity coefficient (ϕ)

In case of wall-bounded gas-particle flows (like flow inside channels), there is always an interaction between the solid wall and moving particles. Depending upon the roughness of the wall, there is always some loss of particle momentum due to the interactions with the wall. To quantify this loss, a parameter termed as specularity

coefficient (ϕ) is introduced which is the ratio of the momentum loss due to particle-wall collisions to the total momentum of the particles. A value of ϕ equal to zero refers to a perfectly smooth wall where there is no loss of particle momentum due to particle-wall collisions (specular collisions, leading to free-slip condition for particle velocity) and a value equal to unity leads to totally diffusive collisions where the particle momentum is completely lost due to collisions with the wall. The boundary conditions for particle velocity, based on the value of ϕ are derived from Johnson and Jackson [14] model.

1.4.5 Particle-particle restitution coefficient (e)

In case of gas-particle flows where the particle phase volume fraction is sufficiently high, there is always a loss of particle momentum due to particle-particle collisions which effects the overall flow hydrodynamics. This loss in particle momentum is quantified by introducing particle-particle restitution coefficient (e) which is a measure of momentum loss due to particle-particle collisions. A value of e equal to unity refers to perfectly elastic collisions where no momentum is lost due to collisions and a value of e equal to 0.8 means that 20% of the particle momentum is lost due to collisions.

1.4.6 Packing limit ($\alpha_{s,max}$)

In case of dense gas-particle flows, there is a limit or upper bound on the value of particle phase volume fraction even for closely packed flow situations. This value is referred to as the packing limit. Generally, for spherical particles, it is taken as 0.63.

1.4.7 Minimum volume fraction ($\alpha_{s,min}$)

In dense gas-particle flow scenarios, it is defined as the volume fraction above which the frictional stresses become dominant in the overall hydrodynamics of the flow. Generally, in case of spherical particles, it is taken as 0.5.

1.5 Concept of fluidization

Fluidization is referred to as the process of transforming solid particles into a fluid-like state by suspending them in a gas medium. Generally, this process takes place when a gas flow is introduced from the bottom of a bed containing solid particles at a certain velocity large enough such that the gas drag on the particles can overcome gravity [15]. The solid particles in fluidized state can be easily transported and also, intense mixing obtained due to fluidization results in high mass-transfer rates. Due to these advantages, the concept of fluidization is applied in industrial process systems like gas-solid fluidized beds. The smallest value of inlet gas velocity at which fluidization occurs is referred to as minimum fluidization velocity.

The behavior of the particles fluidized by gas mainly depends upon their material density and mean size. Geldart [16] classified the particles based on their density and mean size into four clearly recognizable groups. Group A contains particles having material density less than 1.4 g/cm^3 and particle size is in the range of 20-100 μm. In group B, the particle size typically lies between 40-500 μm and the particle density between 1.4-4 g/cm^3. Group C contains extremely fine and the most cohesive particles with a size of 20 to 30 μm; while in Group D, the particle size is above 600 μm and the particles have very high values of material density. Distinguishable differences in the fluidization characteristics can be observed for all the four groups of solid particles.

In a broader sense, the gas-solid fluidized beds can be classified on the basis of the flow behavior inside. The general classifications are given below.

Bubbling gas-solid fluidized beds: In these types of fluidized beds, the inlet velocity of the fluidizing gas is relatively low (generally of the order or few times higher than the minimum fluidization velocity) and so, the fluidization zone is relatively stationary with very few particles being entrained from the bed. Due to the low values of gas inlet velocities, interphase forces other than the drag force (like lift force and virtual mass force) become insignificant in case of these beds and the resulting flow inside the bed can be considered as laminar [17].

Circulating fluidized beds: In this type of beds, gas enters at a higher velocity

sufficient to suspend the bed of the particles. Due to the higher kinetic energy of the gas, larger number of particles can be entrained from the bed and the entrained particles are made to recirculate through an external loop back to the bed.

Vibratory fluidized beds: These are the beds in which an additional mechanical vibration is added to increase the particle entrainment.

Transport or flash reactors: These beds are subjected to a relatively higher values of gas velocity (higher than circulating fluidized beds) in order to encourage a continuous particle distribution throughout the domain. The slip between the gas and the solid phase is significantly reduced providing a positive impact on the overall heat and mass transfer rates.

Annular fluidized beds: In these types of beds, there is a large nozzle at the center of the bed which introduces gas at a high speed and additional fluidized gas is introduced through an annular nozzle ring which facilitates intense mixing of the gas and the solid particles in the bottom part of the chamber.

1.6 Solution methods

In a broader sense, there are two approaches for numerically solving gas-particle flows.

1. Eulerian-Eulerian approach (two-fluid model)
2. Eulerian-Lagrangian approach (discrete element model, discrete parcel model)

1.6.1 Eulerian-Eulerian approach

In this approach the two phases (i.e, the gas phase and the particle phase) are considered as inter-penetrating continua. The two phases coexist in all parts of the flow domain, but cannot coexist at a point. The interaction between the two phases is taken care of by implementation of exchange-coefficients which often need to be specified empirically [18]. To find out the relative amount of each phase present in the flow domain, the concept of volume fraction (Eq. 1.1) is adopted in this approach. The volume fraction α is a continuous variable with a value at all the

points in the domain and often transport equations are solved for it.

In Eulerian-Eulerian approach, the properties of the dispersed particle phase are assumed to be continuous like those of a fluid. The particle phase is solved using fluid-like equations and so it becomes relatively easy to implement, solve and interpret the particle phase along with the fluid phase equations [19]. It also takes relatively less computational time in simulating the flow. Due to these advantages this approach is extensively used in simulations of gas-particle flows. In the work reported in this thesis, this approach is used to solve gas-particulate flows.

But there are also some inherent difficulties in the use of Eulerian-Eulerian model for gas-particle flows. The main difficulty is the modeling of surface boundary conditions for the particle phase. To overcome this problem, Tu et al. [13] established a set of Eulerian formulation with generalized wall-boundary conditions and developed a particle wall collision model to better represent the particle wall momentum transfer. The most commonly used model in order to implement the boundary conditions for particle velocity is the Johnson and Jackson [14] model.

1.6.2 Eulerian-Lagrangian approach

In this approach the gas phase is treated as a continuum as in the Eulerian-Eulerian approach but the particle phase is treated using Lagrangian approach, i.e., instead of treating the particle phase as a whole, it is represented by discrete particles. In discrete element method (DEM), the motion of each individual particle is tracked inside the computational domain. Each particle is considered as one distinct element in the particle cloud and the equations of motion for all the elements are solved. In discrete parcel method (DPM), a parcel of particles is considered which moves through the field and equations of motion for such parcels are solved. Eulerian-Lagrangian approach provides detailed description of particle motion including the details of history and takes into account all the forces acting on the particles. One advantage of this approach is that the implementation of exchange coefficients as in the case of Eulerian-Eulerian approach is not required. But as the number of particles in the flow domain increases, this approach becomes much more robust and computationally very much expensive.

1.7 Review of literature

This doctoral thesis is about the development of a generic finite volume based flow solver for gas-particulate flows using Eulerian-Eulerian approach and its application to several problems including parametric studies. Therefore, an extensive review of literature has been carried out on the use of Eulerian-Eulerian two-fluid model for gas-particulate flows and associated challenges, role of different particle phase properties, effects of particle-particle and particle-wall interactions and finally on the gas-particulate flows in gas-solid fluidized beds.

1.7.1 Eulerian-Eulerian approach

In this approach, the particle phase is simulated using fluid-like equations and the interactions between the phases are taken care by introducing interphase exchange terms in the governing equations of both the phases. This approach has been widely used by various researchers over the years to solve different problems involving gas-particulate flows. Danon et al. [20] carried out numerical simulations to study a two phase round jet and studied the particle phase effects on different carrier phase quantities. Chen and Wood [21] started from Danon et al. [20] and simulated dilute gas-particle flows in a round jet assuming a two-way coupling between the phases and proposed new a closure model to take care of gas phase velocity fluctuations. A similar approach was taken by Mostafa and Mongia [22] in the simulations of a round gaseous jet laden with solid particles. Shauen et al. [23] carried out studies on wall-free flows and measured the mean and fluctuating velocities of both phases as well as the particle mass-fluxes in a dilute particle-laden jet injected into a still environment. Mostafa et al. [24] also carried out studies for an axisymmetric gaseous jet laden with evaporating liquid droplets. Similar studies on dilute gas-particle axisymmetric jet was carried out by Chen et al. [25].

In addition to these wall-free flows (jet flows), Eulerian-Eulerian two fluid model has also been used extensively in case of wall bounded flows like pipe flows. Tu and Fletcher [26] studied the effects of particle phase velocity fluctuations in case of confined gas-particulate flows. A two-way coupling between the phases were considered and the additional dissipation of energy due to the particle velocity fluctuations is taken care by adding extra source terms in the corresponding governing equa-

tions. The results obtained were compared with the experimental data of Tsuji et al. [27]. Again, Tu and Fletcher [13] carried out numerical computation of dilute gas-solid flow in a square-sectioned 90° bend and the results were compared with the laser doppler velocimetry (LDV) results of Kliafas and Holt [28]. The particle-wall momentum exchange was taken care of by introducing an extra source term in the governing equations of the particle phase and also a set of generalized Eulerian boundary conditions for the particle phase at the solid wall was derived in this work which can be written in a generic form

$$a\phi_w + b\left[\frac{\partial\phi}{\partial n}\right]_w = c \qquad \text{where} \quad \phi = [u_s^N, u_s^T, \rho_s] \tag{1.7}$$

where u_s^N and u_s^T are the average particle velocities normal and tangential to the wall respectively and ρ_s is the particle density. This simulation showed a satisfactory agreement with the experimental data. Tu [29] combined this model with the overlapped grid technique and successfully simulated dilute gas-particle flows over a backward-facing step and a T-junction channel. A comparative study on the various existing models was carried out by Enwald et al. [30].

Ferry and Balachandar [31] proposed a new Eulerian method for disperse two phase flows which was basically applicable to the particles with very small values of Stokes number (i.e., particles with small response time τ_p, Eq. 1.2). It was concluded that provided the particle response time (τ_p) normalized by the fluid time-scale is less than 1, the particle velocity field approaches a unique equilibrium field, independent of initial conditions. In this case, the particle velocity field depends only on the local fluid properties and can be expressed as an expansion of τ_p. Therefore, the necessity to solve additional partial differential equations for the particle phase gets avoided and hence, the method becomes much faster than the standard Eulerian method. But the applicability is limited only to very small size particles. Moukalled et al. [32] presented a new algorithm for predicting both incompressible and compressible multi-phase flow phenomena. The method was formulated on a non-orthogonal co-ordinate system with collocated arrangement of primitive variables. The main difference of this algorithm with the earlier ones was that pressure was selected as a dependent variable ahead of density as the changes in pressure are significant at all speeds contrary to variations in density, which becomes very small for low Mach number compressible flows. MCBA (Mass Conservation Based Algorithms)-SIMPLE algorithm was used in the overall solution procedure which

is an extension to single phase SIMPLE algorithm. Pressure correction equation is derived from the overall mass-conservation equation which is obtained by adding the mass conservation equations for all the phases. This algorithm was found to be equally applicable in the subsonic, transonic and supersonic regimes.

Tian et al. [33] simulated dilute gas-particle flows over a backward facing step and observed that in case of particle flow predications, the results obtained using Eulerian-Eulerian model were closer to the measured experimental data. Mohanarangam et al. [34] used the models developed by Tu and Fletcher [13] and Tu [29] and simulated gas-particle flows in a 90° bend. For the particle concentration distribution along the bend, a remarkable qualitative agreement with the experimental data was found. In a similar study, Mohanarangam et al. [18] compared the above results with those obtained by using Eulerian-Lagrangian approach and concluded that the results obtained by using Eulerian-Eulerian approach were closer to the experimental data of Kliafas and Holt [28]. Benavides et al. [35] carried out a numerical study of dispersed gas-particle flow in a two-dimensional vertically oriented backward facing step. In this work, the kinetic energy associated with the fluctuations in the particle phase velocity was expressed incorporating the kinetic theory for granular flows (KTGF) model and represented by the particle phase granular temperature (θ). So, a balance equation to solve θ has been applied along with the governing equations of both the phases. Akbarinia and Laur [36] studied the effects of particle size on the laminar flow inside a curved tube. Kalteh et al. [37] used Eulerian-Eulerian two fluid model in the simulation of laminar forced convection heat transfer of a copper–water nanofluid inside an isothermally heated microchannel.

1.7.2 Gas-particle flows considering two-way coupling

Different physical properties of the particle phase have significant effects on the flow hydrodynamics of gas-particle flows. To gain insights into the effects of change of these properties, a number of parametric studies have been carried out till date. Majority of these studies have been either in recirculating flow conditions (such as flow over a backward facing step) or in plain Poiseuille flows (such as flows through vertical and horizontal channels). Barton [38] carried out a numerical computation of dilute particulate laminar flow over a backward facing step which was an exten-

sion to the the numerical study done by him for single phase flow [39]. The particle phase was treated with Lagrangian approach and the behavior of the flow for various inlet values of Reynolds number, Stokes number and void fraction was studied. It was found that for a particular value of volume fraction of the particles at the inlet, particles with low Stokes number tend to increase lower recirculation region and decrease the upper recirculation region; while the particles with high Stokes number, dominated by their initial inlet velocity and gravitational force, tend to deposit on the lower boundary compressing the lower recirculation region. Both upper and lower recirculation lengths were found to increase with increase in particle phase volume fraction for a certain value of particle Stokes number. Barton [40] also proposed a new predictor-corrector based exponential Lagrangian particle tracking scheme which showed a better performance in terms of accuracy and computational efforts. Barton [41] studied particle gladden laminar flow with a stream of hot particles over a backward-facing step. The thermal effects considered in that case were buoyancy and themophoresis effect. It was found that the buoyancy effects suppress the various factors that cause reattachment for the main recirculation region behind the backward facing step and the thermophoresis effect drives the particles away from the hot fluid towards colder regions, which subsequently effects the flow field. Yu et al. [42] carried out extensive studies on the effects of inlet slip (or difference of velocities of the phases at inlet) between the phases in case of dispersed gas-particle flow in a single-side backward facing step flow. It was observed that the dispersion of the particles with Stokes number in the range of unity is less sensitive to the changes in inlet slip than the higher Stokes number particles.

Similar studies have also been carried out for flows through vertical and horizontal channels. Significant work in simulations of dilute laminar gas-particle flows was carried out by Passalacqua and Fox [43]. In this work, a third order quadrature based moment method coupled with a fluid solver has been applied to simulate dilute gas-particle flow in a vertical channel with particle phase volume fractions between 0.0001 and 0.01. The effect of particle phase volume fraction on particle velocity has been studied. Similar work was carried out by Passalacqua et al. [44] in which numerical simulations of laminar gas-particle flows were carried out for particle Stokes numbers 0.061 and 0.61 in a 2-D vertical channel and results are compared with those obtained from two-fluid model. Zhao et al. [45] studied the effects of particle slip velocity in wall bounded turbulent flows and found that the

slip velocity fluctuations exhibit a monotonic increase with increasing particle Stokes number. Deshmukh et al. [46] used particle image velocimetry to study the velocity distribution and profiles of mean velocities and volume fractions of particles in a gas-solid mixture through horizontal channels. It was found from the experiments that the small diameter particles are better dispersed in the channel than the larger ones. In general, in the above studies, the effects of particle-particle and particle-wall interactions on the overall hydrodynamics have not been taken into account in detail and so, largely, they assumed a two-way coupling between the phases.

1.7.3 Particle-particle and particle-wall interactions in channel flows

Along with physical properties of the particle phase, particle-particle and particle-wall interactions also play a significant role in case of gas-particle flows through channels. So, a number of studies have been carried out to investigate the effects of these interactions on the hydrodyanamics of such flows. Sommerfeld and Kussin [47] carried out experimental study on pneumatic conveying of spherical particles in a narrow horizontal channel using two-component phase doppler anemometry where wall roughness was considered in the range of 2-17 μm. It was found that increasing the degree of wall roughness resulted in higher loss of particle momentum near the wall. Similar type of study has been carried out by Lain and Sommerfeld [48] both numerically and experimentally considering a wide range of particle diameter and wall roughness value. Zhu et al. [49] concluded that particle-wall interactions had a more significant effect on the flow dynamics for particles with higher diameter than for smaller particles. Eskin [50] numerically carried out study on dilute turbulent gas-particle flows in flat horizontal channels using an approach of tangential restitution coefficient, but the study was done for low particle phase volume fractions. Passalacqua and Fox [43] used the solver MFIX to simulate dilute gas-particle flow in a vertical channel with particle phase volume fractions between 0.0001 and 0.01. The wall boundary conditions are set to be specularly reflective, i.e., no particle momentum is lost due to collisions with the wall and the particle-particle collisions are considered to be perfectly elastic. Soleimania et al. [51] modified the twoPhaseEulerFoam solver of OpenFOAM using the modified boundary conditions given by Li and Benyahia [52] and studied the effects of these modifications in the particle phase ve-

locity profiles in channels. Li et al. [53] observed that the simulations carried out considering particle-particle interactions showed closer agreement with experimental results for dispersed gas-particle flows through a sudden expansion. Zhao et al. [54] proposed a new semi-analytical and flow-dependent model for specularity coefficient based on the measurable particle properties and the model was integrated to the open-source code MFIX.

1.7.4 Gas-particle flows subjected to recirculation

From the point of view of fluid mechanics, whenever there is an expansion in the area of cross-section of the flow, generally there is flow separation and a recirculation zone is obtained. The best examples are flow over a backward facing step and flow through a sudden expansion. Gas-particle flows have applications in coal combustors, cyclone separators and air filters where there exist possibilities of flow separation. Therefore, prediction of the complex flow behavior inside the recirculation zone and the effects of the presence of particles in the overall hydrodynamics in case of separating gas-particle flows is of utmost importance. This has fuelled research activities in this field for many years to better understand the flow physics of this class of flows.

Arefmanesh and Michaelides [55] carried out an experimental study on the pressure changes of air-solid flows through a sudden expansion. Ruck and Makiola [56] studied the dispersion of particles in a backward facing step of expansion ratio 1:2 and found that the recirculation zone length gets decreased as the particle size increased. Barton [38] in his numerical study observed that recirculation length tends to decrease with increase in particle Stokes number, whereas it increases with increase in particle phase volume fraction and flow Reynolds number. Fessler and Eaton [57] studied the modifications brought about by particles in the carrier phase turbulence and observed an increase in the modulation of carrier phase with increase in particle Reynolds number, Stokes number and volume fraction. Yu et al. [42] studied effects of particle Stokes number and inlet velocity slip between the carrier phase and dispersed phase in case of flow over a backward facing step using large eddy simulation technique. Terekhov and Pakhomov [58] performed a comparative analysis with available data for gas-dispersed flows through a pipe with sudden expansion which was further extended for swirling gas-dispersed flows through sudden

expansion by Terekhov and Pakhomov [59]. Gundogdu et al. [60] proposed a new analytical model called as slip flow model for determination of pressure drops inside a sudden expansion geometry. Mohanarangam et al. [61] carried out numerical study of dilute gas-particle flows through a sudden expansion geometry and investigated the effects of step height and particle Stokes number on the recirculation characteristics and overall flow hydrodynamics where particle-particle and particle-wall interactions were not taken into account. Mergheni et al. [62] predicted the axial mean velocity and turbulent kinetic energy of both the phases using Runge-Kutta method for Lagrangian tracking of particles. Li et al. [53] observed that the simulations carried out considering particle-particle interactions showed closer agreement with available experimental results. But the effects of particle-particle interactions on the recirculation length past the step have not been taken into account. Love et al. [63] carried out numerical analysis within a double expansion and found two large recirculation zones in opposing corners of the domain for increasing mass loading and particle Stokes number.

1.7.5 Gas-particle flows in fluidized beds

The main application of gas-particle flows is seen in gas-solid fluidized beds where the solid particles are transformed into a fluid like state by suspending them in gas. Gas-fluidized beds consist of fine granular materials (usually smaller than 5 mm) which are subjected to a gas flow from the below, large enough so that the gas drag on the particles can overcome gravity, and the particles fluidize. A lot of research has been carried out in the simulation of gas-particle flows in fluidized beds. Chisea et al. [64] carried out a computational study of the flow behavior of a lab-scale fluidized bed. In this work, the sub-grid scale (SGS) model proposed by Deardorff [65] has been used to resolve small length scale fluid motions. The results obtained from Eulerian-Eulerian approach were compared with the results obtained from the Eulerian-Lagrangian approach and was found that the CPU time required in Eulerian-Lagrangian approach was four order of magnitude higher than the Eulerian-Eulerian approach. Lindborg et al. [66] carried out simulations of bubbling gas-solid flows in fluidized beds using finite-volume method with time-splitting approach on a staggered grid arrangement. The velocities in both the phases were solved using partial elimination algorithm proposed by Spalding [67]. Particle motion, bubble size and bubble rise velocity were found to be the important

parameters in governing the physics of such type of flow situations. Duarte et al. [68] performed simulations using Eulerian-Eulerian multiphase model to find out the fluid dynamic behavior of spouted beds with two different geometries which were conical-cylindrical and conical respectively. Spouted beds are the fluidized beds in which particles having a wide size distribution and particles having rough and adhesive strength can be fluidized which cannot be fluidized in conventional fluidized beds.

The boundary conditions for particle velocities and granular temperature (θ) are derived by Johnson and Jackson [14]. Wachem et al. [69] used kinetic theory for granular flows (KTGF) model to investigate the dynamic characteristics of the gas-solid behavior at different superficial gas velocities. Taghipour et al. [70] studied the hydrodynamics of gas-solid fluidized beds experimentally in a fluidized bed containing spherical glass beads of 250-300 μm in diameter. Numerical study was done using Fluent software. Passalacqua and Marmo [71] studied the effects of frictional stress among the particles on the flow dynamics of gas-solid fluidized beds using different frictional stress models. Loha et al. [17] studied the effect of different drag models in simulating bubbling fluidized bed hydrodynamics. Time-averaged particle axial velocity profiles and solid volume fraction profiles have been studied using different drag models. Lindborg et al. [66], Beniyahia et al. [72] and Loha et al. [17] also studied the effect of turbulence modeling of the gas phase in calculation of bed hydrodynamics of bubbling gas-solid fluidized beds. It has been found that very little changes in time-averaged velocity profiles and solid phase volume fraction profiles occur as the gas flow field is changed from laminar to turbulent by applying suitable turbulence models in case of bubbling gas-solid fluidized beds.

Loha et al. [73] studied the influence of specularity coefficient (ϕ) on the hydrodynamic behavior of gas-solid fluidized bed. Different values of ϕ resulted in different particle velocity, granular temperature and particle volume fraction both close to the wall and in the central region. Similar type of study was done by Loha et al. [74] to check the effect of variation of particle-particle restitution coefficients on the flow characteristics of gas-solid fluidized beds. All these studies [17], [73] and [74] were performed numerically using commercial CFD software FLUENT. Verma et al. [75] studied the effects of changing the bed size (diameter) on the hydrodynamics in gas-solid fluidized beds. Zinani et al. [76] studied the effects of changing

the drag model on the fluidization characteristics of bubbling gas-solid beds. Noticeable variations in some cases have been observed in the results with different drag models. Alamolhoda et al. [77] carried out an experimental study and used the vibration characteristics of a wall of bubbling fluidized bed to investigate the effect of change in particle size on fluidized bed hydrodynamics. In this study, variation of total energy and particle spectral density function with particle size have been investigated for particles with different mean sizes.

1.8 Motivation and objectives

A careful analysis of the review of literature presented in the previous section reveals that although a considerable amount of studies have already been carried out in case of gas-particle flows both numerically and experimentally, yet there remain certain important points which are less discussed. Firstly, it has been observed that almost all the numerical works studied in this field have been carried out using commercial solvers (Ansys Fluent [78]), opensource solvers (OpenFOAM [79]) or specialized solvers (MFIX [80]). Very few numerical studies have been found which have been carried out using indigenously developed inhouse flow solvers. Apart from this, it has also been observed that very few studies are available in which a complete parametric study of laminar dispersed flows have been carried out through channels which involve the study of effects of particle diameter (Stokes Number), particle phase material density, inlet particle phase volume fraction together; assuming two-way coupling between the phases. Also, the effects of inlet slip (or difference of velocities of the phases at inlet) for laminar dispersed flows through horizontal channels have not been reported.

While particle-particle and particle-wall effects have been reported to be more significant for higher diameter particles and at higher particle volume fractions [49], no studies have been found which quantitatively analyze these effects, quantified by ϕ and e, individually as well as in combination for a detailed hydrodynamic study of dispersed particulate flows through horizontal channels. Also, the effects of variation of these two parameters on the steady state phase velocities, volume fraction and average wall shear stress have hardly been discussed.

Furthermore, the review of literature on recirculating gas-particulate flows reveals that majority of the studies focus on the effects of variations of flow Reynolds number, particle diameter, particle volume fraction, inlet phase slip and step height on the overall hydrodynamics. It has also been found that phase velocities obtained in case of flow through a sudden expansion match closer with experimental data for simulations in which particle-particle interactions have been taken into account [53]. But, very few studies have been found in which the effects of both particle-particle and particle-wall interactions on recirculation characteristics have been carried out quantitatively in case of recirculating gas-particulate flows. The stretching or shrinking of recirculation zone with change in e and ϕ could be vital in the design of gas-solid separators, air filters and diffusers where there exists a distinct possibility of flow separation.

While the applications of two-fluid model have largely focussed on analyzing the gas-particulate flows in gas-solid fluidized beds and the effects of inlet gas velocity, bed dimensions, frictional stresses, change in drag models, particle-particle and particle-wall interactions have widely been studied in studies like [17, 70, 72, 75], there are very few studies which help in understanding the effects of variations of particle diameter on the overall fluidization characteristics of bubbling gas-solid fluidized beds. In particular, the changes in the time-averaged phase velocity and volume fraction profiles due to the change in particle diameter have not been discussed in details in literature.

With the above motivation, the objectives of the present thesis have been framed as given below.

Solver development

The primary objective of this thesis is to develop an indigenous finite volume method based flow solver to simulate gas-particle flows capable of handling all flow situations (ranging from dilute to dense) on both orthogonal and non-orthogonal meshes in the framework of Eulerian-Eulerian two-fluid model. Kinetic theory for granular flows and frictional stess models will be incorporated into the solver to care of particle-particle and particle-wall interactions. A detailed validation of the flow solver for a vast spectrum of problems of gas-particulate flows will be carried out to evaluate its

robustness and viability for practical flow scenarios.

Parametric study considering two-way coupling between the phases

The flow solver will be used to simulate dispersed laminar gas-particle flows in horizontal and vertical channels assuming two-way coupling between the phases in order to study the effects of various parameters including particle diameter (Stokes Number), particle phase material density, inlet particle phase volume fraction in details. The effects of inlet slip (or difference of velocities of the phases at inlet) for laminar dispersed flows through horizontal channels will be studied separately.

Effects of variation of ϕ and e in flows through horizontal channels

The effects of variation of specularity coefficient (ϕ) and particle-particle restitution coefficient (e) on the hydrodynamics of dispersed gas-particle flows through horizontal channels will be investigated. The effects of variation of ϕ on the steady state phase velocities and volume fraction profiles for a particular value of e will be studied and vice-versa. Analysis will also be carried out on the effects of variation of ϕ on the average wall shear stress of both the phases.

Effects of variation of ϕ and e in flows subjected to recirculation

In this study, the effects of variation of ϕ and e on the recirculation length will be studied for dispersed gas-particle flows through a sudden expansion. The variations in the recirculation lengths with change in the value of e at a particular value of ϕ will be studied and vice-versa. Also, the combined effects of different combinations of ϕ-e pairs on recirculation characteristics of dispersed gas-particle flows through a sudden expansion will be studied.

Effects of particle diameter on fluidization characteristics

This study will be on the effects of variation of particle diameter on the fluidization behavior inside bubbling gas-solid fluidized beds. The effects of change in the particle diameter on time-averaged phase velocity and volume fraction profiles at different sections inside the fluidized bed reactor will be analyzed keeping all other flow and

physical properties invariant. Also, the changes in the time-averaged particle phase volume fraction contours occurring with change in the particle diameter will be investigated.

1.9 Thesis overview

The remainder of the work discussed is this thesis is organized in the following chapters.

Chapter 2 presents the details of the governing equations and discretization procedure adopted in the development of the inhouse gas-particle flow solver. Different models incorporated into the solver to take care of the presence of the particle phase as well as the empirical relations used to calculate different particle phase properties have been explained. The chapter concludes with the details of the solution algorithm.

Chapter 3 is dedicated to the validation of the developed solver. As the solver is indigenously developed, it is extensively validated with available published data at every stage of the development. In cases where standard benchmark data is not available, some test cases have also been validated with available commercial or opensource solvers.

In Chapter 4, a detailed parametric study of dispersed laminar gas-particle flows through vertical and horizontal channels have been carried out assuming two-way coupling between the phases. The effects of various particle properties like particle diameter (Stokes number), particle material density, inlet particle phase volume fraction on the hydrodynamics of dispersed laminar gas-particle flows have been discussed. Also, the effects of inlet slip (or difference of phase velocities at the inlet) on the steady state phase velocity and volume fraction profiles have been studied for laminar dispersed flows through horizontal channels.

Chapter 5 focusses on the effects of variation of specularity coefficient (ϕ) and particle-particle restitution coefficient (e) on the overall hydrodyanamics of dispersed gas-particle flows through horizontal channels. Also, the combined effects of these

two parameters on the steady state phase velocities and volume fraction profiles have been studied. Investigations have also been carried out to study the effects of variation of ϕ on the average wall shear stress of both the phases.

Chapter 6 discusses the effects of specularity and particle-particle restitution coefficients on the recirculation characteristics of dispersed flows through a sudden expansion. Studies have been carried out to find the effects of variation of e at a particular value of ϕ and vice-versa. Also, the combined effects of different values of ϕ-e pairs on recirculation characteristics have been studied.

In chapter 7, the developed solver is first used to simulate different cases of bubbling gas-solid fluidized beds and a detailed validation of the results obtained from the developed solver have been compared with the available numerical and experimental data. After that, the solver is used to study the effects of particle diameter on the overall fluidization characteristics of bubbling gas-solid fluidized beds keeping all other flow and physical parameters invariant.

Chapter 8 concludes the work presented in the thesis along with scopes for future work.

Chapter 2

Governing equations and discretization procedure

In this chapter, an overview of the governing conservation equations along with the details of the numerical discretization technique used for the development of the finite volume gas-particulate flow solver have been discussed. Collocated grid arrangement has been used where all the dependent variables are defined at the centroid of each individual cell. Both the phases are treated using Eulerian approach where the conservation equations for mass and momentum are solved for the gas and particle phases separately and interaction is taken care by inter-phase exchange term. Kinetic theory for granular flows (KTGF) model has been used in combination with Eulerian-Eulerian two fluid model in order to take care of particle phase velocity fluctuations. In order to account for the frictional stresses generated due to the close packing of particles, frictional stress model is incorporated into the solver.

2.1 Governing equations

The general assumptions while formulating the governing equations of both the phases are given below.

1. The particles are assumed to be uniform spheres of constant diameter.
2. There is no mass or momentum transfer over the surface of the particles due to particle-particle interactions.

3. The flow field is isothermal and the physical properties of both phases are constant.

Based on these assumptions, the generalized governing equations of both the phases are formulated as given below. The details of derivation of these equations can be found in the work of Jackson [81].

Gas phase continuity equation

$$\frac{\partial(\alpha_g \rho_g)}{\partial t} + \nabla \cdot (\alpha_g \rho_g \mathbf{u}_g) = 0 \tag{2.1}$$

where α_g is the gas phase volume fraction, ρ_g is the gas phase material density and $\mathbf{u}_g$ is gas phase velocity vector. There is no mass exchange between the phases and the material densities of the individual phases remain constant. As the material density of a particular phase remains constant, so Eq. 2.1 can be re-written as

$$\frac{\partial \alpha_g}{\partial t} + \nabla \cdot (\alpha_g \mathbf{u}_g) = 0 \tag{2.2}$$

Gas phase Momentum Equation

The gas phase momentum equation is given by the Navier-Stokes equations, modified to incorporate the effect of the presence of the particle phase.

$$\frac{\partial(\alpha_g \rho_g \mathbf{u}_g)}{\partial t} + \nabla \cdot (\alpha_g \rho_g \mathbf{u}_g \mathbf{u}_g) = -\alpha_g \nabla p + \nabla \cdot \overline{\overline{\tau_g}} + \alpha_g \rho_g \mathbf{g} + K_{gs}(\mathbf{u}_s - \mathbf{u}_g) \tag{2.3}$$

here p is the hydrodynamic pressure, $\overline{\overline{\tau_g}}$ is the viscous stress tensor of the gas phase, $\mathbf{g}$ is the acceleration due to gravity and K_{gs} is the momentum exchange coefficient between the phases. The gas phase being assumed as a Newtonian fluid, the stress tensor $\overline{\overline{\tau_g}}$ is expressed using the following expression.

$$\overline{\overline{\tau_g}} = \alpha_g \mu_g [\nabla \mathbf{u}_g + (\nabla \mathbf{u}_g)^T] - \frac{2}{3} \alpha_g \mu_g (\nabla \cdot \mathbf{u}_g) \mathrm{I} \tag{2.4}$$

where μ_g is the dynamic viscosity of the gas phase and $\mathbf{I}$ is the unit tensor.

The term containing K_{gs} in Eq. 2.3 gives the amount of drag acting on the gas phase due to the presence of the particles. This term is insignificant in case of

one-way coupling, as for one-way coupling the particle phase volume fraction is too small to have any effect on the gas phase flow fields. But as volume fraction of the particle phase increases gradually, the drag force term appearing in Eq. 2.3 becomes significant in the overall hydrodynamics of the flow. Different models are available to calculate the value of the momentum exchange coefficient (K_{gs}) between the phases.

In Eulerian-Eulerian approach, the governing equations for the particle phase are also written in a similar manner as the governing equations of the gas phase. Additional terms are incorporated to take care of interaction among the particles. The governing equations for the particle phase can be written as given below.

Particle phase continuity equation

$$\frac{\partial(\alpha_s\rho_s)}{\partial t} + \nabla\cdot(\alpha_s\rho_s\mathbf{u}_s) = 0 \tag{2.5}$$

where α_s is the particle phase volume fraction, $\mathbf{u}_s$ is the velocity vector of the particulate phase and ρ_s is its material density which remains constant as there is no mass exchange among the phases. So, the continuity equation can be written as

$$\frac{\partial\alpha_s}{\partial t} + \nabla\cdot(\alpha_s\mathbf{u}_s) = 0 \tag{2.6}$$

Particle phase momentum equation

$$\frac{\partial(\alpha_s\rho_s\mathbf{u}_s)}{\partial t} + \nabla\cdot(\alpha_s\rho_s\mathbf{u}_s\mathbf{u}_s) = -\alpha_s\nabla p - \nabla p_s + \nabla\cdot\overline{\overline{\tau_s}} + \alpha_s\rho_s\mathbf{g} + K_{gs}(\mathbf{u}_g - \mathbf{u}_s) \tag{2.7}$$

where p_s is the solid pressure and $\overline{\overline{\tau_s}}$ is the solid phase shear stress tensor. Like the gas phase shear stress tensor $\overline{\overline{\tau_g}}$, $\overline{\overline{\tau_s}}$ is expressed as

$$\overline{\overline{\tau_s}} = \alpha_s\mu_s[\nabla\mathbf{u}_s + (\nabla\mathbf{u}_s^T)] + \alpha_s(\lambda_s - \frac{2}{3}\mu_s)(\nabla\cdot\mathbf{u}_s)\mathbf{I} \tag{2.8}$$

where μ_s is the particle phase shear viscosity and λ_s is the solid bulk viscosity. In case of one-way and two-way coupling between the phases, the viscous stresses ($\overline{\overline{\tau_s}}$) and the solid pressure (∇p_s) terms in Eq. 2.8 are not taken into account. These two terms take care of the particle-particle interactions and hence, are considered for the simulations assuming three-way coupling. the calculation of these two quantities are done based on some empirical relations which are derived from the KTGF model.

2.2 Kinetic theory for granular flows model

In this work, kinetic theory for granular flow (KTGF) model has been used in combination with Eulerian-Eulerian two fluid model in order to take care of particle phase velocity fluctuations. According to this model, the total energy (E) per unit mass of a granular or particulate phase is composed of three parts [14] which are

$$E = E_{MK} + E_{PT} + E_h \tag{2.9}$$

where E_{MK} is the kinetic energy associated with the local average velocity, E_h is the true thermal internal energy of the solid material and E_{PT} is the pseudo kinetic energy associated with the deviations of the motion of the individual particles from the local average. In KTGF model, the kinetic energy associated with the fluctuations of the particle velocity from the local average value (E_{PT}) is represented by a by a new variable called **granular temperature** (θ) which is defined below as given in [14]

$$E_{PT} = \frac{1}{2}\overline{v}^2 = \frac{3}{2}\theta \tag{2.10}$$

where $\overline{v}^2$ is the mean square of the velocity fluctuations about the local average value $\mathbf{u}$.

A separate partial differential equation is written for θ which is written as

$$\frac{3}{2}\left[\frac{\partial}{\partial t}(\alpha_s \rho_s \theta) + \nabla \cdot (\alpha_s \rho_s \mathbf{u}_s \theta)\right] = (-p_s \overline{\overline{I}} + \overline{\overline{\tau_s}}) : \nabla \mathbf{u}_s + \nabla \cdot (\kappa \nabla \theta) - \gamma \tag{2.11}$$

where the first term in the right hand side of the above equation is the conversion of energy due to pressure and shear in the particle phase, second one is the conductivity of granular temperature (θ) and the last one is the dissipation due to inelastic collisions. The value of θ obtained from Eq. 2.11 is used to calculate the values of solid pressure (p_s) and solid phase viscosity (μ_s) via empirical relations, and those values are used in the particle phase momentum equation (Eq. 2.7) in order to take care of particle-particle interactions.

2.2.1 Algebraic form of θ equation

In this work, instead of solving the PDE for granular temperature (θ) given in Eq. 2.11, an algebraic form of expression (given by Lun et al. [82]) has been used to calculate the value of granular temperature (θ). This form of expression for

θ has already been used earlier in literature [69, 83, 84]. This algebraic form of θ has been derived assuming that θ is dissipated locally and thus neglecting the convection and diffusion terms and retaining only the dissipative and the source terms of the corresponding PDE, given in Eq. 2.11. The advantage of using this algebraic expression for θ is that the value of θ at all the cell centers can be calculated directly without solving any PDE, also without sacrificing a significant amount of accuracy and with some less amount of computational cost. Hence, in this work, θ is calculated using the following algebraic expression given in Lun et al. [82] and Syamlal [85].

$$\theta = \left(\frac{-k_1 \alpha_s tr(\overline{\overline{D}}_s) + \sqrt{{k_1}^2 {\alpha_s}^2 tr^2(\overline{\overline{D}}_s) + 4k_4\alpha_s(k_2 tr^2(\overline{\overline{D}}_s) + 2k_3 tr(\overline{\overline{D}}_s^2))}}{2\alpha_s k_4} \right)^2 \tag{2.12}$$

In Eq. 2.12, $tr(\overline{\overline{D}}_s)$ is the trace of the viscous stress tensor of the solid phase velocity and the coefficients k_1 , k_2 , k_3 and k_4 are calculated as given below.

$$k_1 = 2(1+e)\rho_s g_0 \tag{2.13}$$

$$k_2 = \frac{4}{3\sqrt{\pi}} d_s \rho_s (1+e)\alpha_s g_0 - \frac{2}{3}k_3 \tag{2.14}$$

$$k_3 = \frac{d_s \rho_s \sqrt{\pi}}{6(3-e)} \left(1 + \frac{2}{3}(1+e)(3e-1)\alpha_s g_0 \right) + \frac{8 d_s \rho_s \alpha_s g_0 (1+e)}{10\sqrt{\pi}} \tag{2.15}$$

$$k_4 = \frac{12(1-e^2)\rho_s g_0}{d_s \sqrt{\pi}} \tag{2.16}$$

where e is the particle-particle restitution coefficient, g_0 is the radial distribution function related to the dimensionless distance of the particles and d_s is the particle diameter. The value of θ obtained from Eq. 2.12 is used to calculate solid pressure (p_s) and solid phase shear viscosity (μ_s) using some empirical relations.

2.2.2 Calculation of solid pressure and radial distribution function

The value of solid pressure (p_s) is calculated using the empirical relation given in Lun et al. [82] which is calculated based on the value of θ obtained from the Eq. 2.12 and the gradient of the solid pressure (∇p_s) is used in particle momentum equation (Eq. 2.7).

$$p_s = \rho_s \alpha_s \theta [1 + 2(1+e) g_o \alpha_s] \tag{2.17}$$

Here, g_0 is the radial distribution function which is related to the dimensionless distance between the particles and is given by Sinclair and Jackson [4] as

$$g_0 = \frac{3}{5}\left[1 - \left(\frac{\alpha_s}{\alpha_{s,\max}}\right)^{\frac{1}{3}}\right]^{-1} \tag{2.18}$$

where $\alpha_{s,max}$ is the maximum allowable packing limit for particles which means that the particle volume fraction cannot exceed beyond that value. Generally, for gas-solid bubbling fluidized bed applications, its value is taken as 0.63.

2.2.3 Calculation of solid phase shear viscosity

The solid phase shear viscosity (μ_s) arises due to translational (kinetic) motion and collisional interactions of the solid particles. Hence, the solid phase shear viscosity can be written as

$$\mu_s = \mu_{s,col} + \mu_{s,kin} \tag{2.19}$$

where $\mu_{s,col}$ refers to the component of solid phase shear viscosity due to collisions among the particles and $\mu_{s,kin}$ is the component due to translational motion of the particles. Several empirical models are available for calculation of the effective solid phase shear viscosity (μ_s) which are described below.

Gidaspow Model: In this model proposed by Gidaspow [86], μ_s is calculated as

$$\mu_s = \frac{4}{5}{\alpha_s}^2\rho_s d_s g_o(1+e)\sqrt{\frac{\theta}{\pi}} + \frac{2}{(1+e)g_o}\frac{5\sqrt{\pi}}{96}\rho_s d_s \theta^{\frac{1}{2}}\left[1 + \frac{4}{5}(1+e)g_o\alpha_s\right]^2 \tag{2.20}$$

The first part of the right hand side of Eq. 2.20 represents the collisional part while the second part is due to the translational motion of the particles. This model for solid phase shear viscosity can be applied to dilute and moderately dilute dispersed flows and also suitable for simulations of dense fluidized bed applications. In the work described in this thesis, the expression given in Eq. 2.20 has been used to calculate μ_s.

Syamlal Model: In this model proposed by Syamlal [80], the collisional part of the solid phase shear viscosity is the same as that of Gidaspow model [86] whereas

the expression for the translational part is different. Here, μ_s is calculated as

$$\mu_s = \frac{4}{5}{\alpha_s}^2\rho_s d_s g_o(1+e)\sqrt{\frac{\theta}{\pi}} + \frac{\alpha_s d_s \rho_s \sqrt{\theta\pi}}{6(3-e)}\left[1+\frac{2}{5}(1+e)(3e-1)\alpha_s g_0\right] \tag{2.21}$$

This model is good for a wide range of applications ranging from dilute to dense flow scenarios.

Sinclair Model: The value of solid phase shear viscosity (μ_s), in this model [87], is calculated as

$$\mu_s = \frac{5d_s\rho_s\sqrt{\theta\pi}}{96\alpha_s}\left\{\left[\frac{8\alpha_s}{5(2-\eta)}\right]\left[1+\frac{8}{5}\eta(3\eta-2)\alpha_s g_o\right] + \frac{768}{25\pi}\eta\alpha_s^2 g_o\right\} + \frac{5d_s\rho_s\sqrt{\theta\pi}}{96\alpha_s\eta(2-\eta)g_o}\omega\left[1+\frac{8}{5}\eta(3\eta-2)\alpha_s g_o\right] \tag{2.22}$$

where

$$\eta = (1+\alpha_s)/2 \tag{2.23}$$

This model of solid phase shear viscosity is particularly suitable for dilute and dense pneumatic transport lines and risers. Generally, it is not largely applied in simulations involving gas-solid fluidized beds.

The solid phase bulk viscosity (λ_s) accounts for the resistance of the granular particles to compression and expansion which is expressed as suggested by Gidaspow [86].

$$\lambda_s = \frac{4}{3}{\alpha_s}^2\rho_s d_s g_o(1+e)\sqrt{\frac{\theta}{\pi}} \tag{2.24}$$

In this work, the values of μ_s and λ_s are calculated using Eqs. 2.20 and 2.24 which are used to calculate the particle phase stress tensor ($\overline{\overline{\tau_s}}$).

2.3 Use of frictional stress model

In case of practical flow situations like gas-solid bubbling fluidized beds, there exist regions where the particles are closely packed. Under those circumstances, the flow physics is influenced more by the frictional stresses generated due to close packing of particles and only KTGF model is not sufficient to adequately describe the flow behavior. Hence, in such flow scenarios, frictional stress model must be

necessarily incorporated into the flow solver in order to obtain physically consistent and stable numerical solutions. Like solid kinetic stresses, the solid frictional stresses also consist of frictional shear stress and frictional normal stress (or frictional solid pressure) [88]. These solid frictional stresses are added to the solid kinetic stresses (p_s and μ_s) calculated using KTGF when the solid volume fraction exceeds a critical minimum value $\alpha_{s,min}$. Generally, the value of $\alpha_{s,min}$ is taken to be 0.5, i.e, if the particle volume fraction exceeds the value 0.5, then only the frictional stresses comes into effect. So, in these cases, the net solid pressure and the net solid phase shear viscosity can be expressed as

$$p_s = p_{s,KTGF} + p_{s,f} \tag{2.25}$$

and

$$\mu_s = \mu_{s,KTGF} + \mu_{s,f} \tag{2.26}$$

The terms $p_{s,KTGF}$ and $\mu_{s,KTGF}$ are calculated using Eqs. 2.17 and 2.20, respectively, whereas frictional solid pressure $p_{s,f}$ is calculated as given by Schaeffer [89] and $\mu_{s,f}$ is calculated as given by Johnson and Jackson [14].

$$p_{s,f} = Fr\frac{(\alpha_s - \alpha_{s,\min})^n}{(\alpha_{s,\max} - \alpha_s)^p} \tag{2.27}$$

$$\mu_{s,f} = p_{s,f}\sin\phi_f \tag{2.28}$$

where the coefficient Fr is taken as a function of $\alpha_{s,min}$ as Fr=0.1$\alpha_{s,min}$, n=2, p=5 and ϕ_f is the internal frictional angle.

2.4 Interphase interaction forces

In two phase flows, there are two mutually interacting phases and the interaction between the phases is greatly influenced by the relative motion between the phases. Due to the mutual interactions, various interphase forces get generated between the phases depending upon physical and flow conditions of the continuous and dispersed phases. The main interphase forces influencing the two phase flow characteristics are

Virtual mass force: In two-phase or multiphase flows, virtual mass force comes into existence when a secondary phase (such as solid particles or droplets or bubbles)

accelerates relative to a primary gas phase. The inertia of the gas phase mass encountered by the accelerating particles (or droplets or bubbles) exerts a virtual mass force on the particles. Mathematically, it is expressed in [68] as

$$\mathbf{F}_{vm} = 0.5\alpha_s\rho_g\left(\frac{d\mathbf{u}_g}{dt} - \frac{d\mathbf{u}_s}{dt}\right) \tag{2.29}$$

The virtual mass effect is significant when the secondary phase density is much smaller than the primary phase density. In case of simulations carried out in this thesis, the secondary phase consists of solid particles which have very high density in comparison to the continuous gas phase. So, this force is not considered in the simulations.

Lift force: This force acts on a secondary dispersed solid phase particles mainly due to the velocity gradients in the primary-phase flow field. The mathematical expression for lift force is given in [68] as

$$\mathbf{F}_l = -0.5\rho_g\alpha_s(\mathbf{u}_g - \mathbf{u}_s)(\nabla \times \mathbf{u}_g) \tag{2.30}$$

The inclusion of this term in the governing equation is justified when the particle size is relatively large (is of the order of 10 mm), as in the case in spouted beds or in case of flows where there is a quick separation of the phases. In other cases, where the particle size is of the order of several hundred microns, the lift force is insignificant compared to the interphase drag force.

Basset force: The Basset force term accounts for the viscous effects of the phases and addresses the temporal delay in boundary layer development as the relative velocity of the phases change with time. It is also known as the history term. This term is significant only in case of unsteady flow conditions where the secondary particles accelerate at a very high rate.

Magnus Force: The magnus force is the lifting force developed due to the rotation of the particles. This effect is caused by a pressure differential between both sides of the particle resulting from the velocity differential due to rotation. The lift produced by the magnus force can be quantified in the following way as given in [10].

$$\mathbf{F}_{mag} = 0.5\rho_g C_{LR} A|\mathbf{u}_s - \mathbf{u}_g|(\mathbf{u}_s - \mathbf{u}_g) \tag{2.31}$$

where A is the projected area and C_{LR} is the lift coefficient due to rotation. This force is significant mainly in case of particles with very large sizes.

Thermophoretic Force: It is an interphase force which comes into existence due to a temperature gradient in the continuous phase. As in this thesis, the flow field is considered to be completely isothermal (mentioned in the assumptions), so this force is not taken into account.

Drag force: It is the force which acts opposite to the relative motion of any object moving with respect to a surrounding fluid. In case of two phase flows, it comes into existence due to the relative motion of the two phases. This force is extremely significant when the ratio of the density of the dispersed phase to the continuous phase (ρ_s/ρ_g) is greater than 100 kg/m^3 [9] and the size of the dispersed phase particles lies in the range of below 700 μm. In the work described in this thesis, the properties of both the phases lies in this range and so, drag force becomes the only significant force out of all these interphase forces.

The drag force acting on a single sphere moving through a fluid medium is well studied and empirically correlated to a wide range of particle Reynolds numbers [68]. However, in case of dispersed gas-particle flows, the drag or interphase momentum exchange is affected by the presence of other particles. To take care of this interphase momentum exchange term (K_{gs}, appearing in Eqs. 2.3 and 2.7) between the gas and particle phases, a number of models have been proposed in different literature. A few of them are Syamlal-O'Brien drag model [90], Gidaspow drag model [86], McKeen model [91] and Kolev's model [92] which are described below.

Gidaspow drag model: In the model proposed by Gidaspow [86], K_{gs} is calculated as

$$K_{gs} = \frac{3}{4} C_d \frac{\alpha_s \alpha_g \rho_g |\mathbf{u}_g - \mathbf{u}_s|}{d_s} {\alpha_g}^{-2.65} \quad \text{if} \quad \alpha_g > 0.8 \tag{2.32}$$

$$K_{gs} = 150 \frac{{\alpha_s}^2 \mu_g}{\alpha_g {d_s}^2} + 1.75 \frac{\alpha_s \rho_g |\mathbf{u}_g - \mathbf{u}_s|}{d_s} \quad \text{if} \quad \alpha_g \leq 0.8 \tag{2.33}$$

where C_d is the drag coefficient between the phases and d_s is the particle diameter.

C_d is given by Kolev [86] as

$$C_d = \begin{cases} \frac{24}{\mathrm{Re}_p} \;\; if \;\; \mathrm{Re}_p \leq 1 \\ \frac{24}{\mathrm{Re}_p}\left(1 + 0.15\mathrm{Re}_p^{0.687}\right) \;\; if \;\; 1 \leq \mathrm{Re}_p \leq 1000 \end{cases} \tag{2.34}$$

Here the particle Reynolds number (Re_p) is defined as

$$Re_p = \frac{\rho_g |\mathbf{u}_g - \mathbf{u}_s| d_s}{\mu_g} \tag{2.35}$$

In Eq. 2.35, μ_g is the dynamic viscosity of the gas phase. This model is very widely used in case of gas-particle flow simulations as it can be used in all the flow conditions ranging from dilute to dense and also are very efficient in simulating complex flows like flows in gas-solid fluidized beds. In this work, the model proposed by Gidaspow [86] has been used in most of the cases.

Syamlal-O'Brien drag model: In this model, the interphase momentum exchange coefficient (K_{gs}) is calculated as follows.

$$K_{gs} = \frac{3}{4} C_d \frac{\alpha_s \alpha_g \rho_g |\mathbf{u}_g - \mathbf{u}_s|}{V_r^2 d_s} \tag{2.36}$$

where the drag coefficient C_d is calculated as

$$C_d = \left(0.63 + 4.8\sqrt{\frac{V_r}{\mathrm{Re_p}}}\right)^2 \tag{2.37}$$

The relative velocity (V_r) is calculated as

$$V_r = 0.5\left[a - 0.06\mathrm{Re_p} + \sqrt{(0.06\mathrm{Re_p})^2 + 0.12\mathrm{Re_p}(2b - a) + a^2}\right] \tag{2.38}$$

where

$$a = \alpha_g^{4.14} \tag{2.39}$$

and

$$b = \begin{cases} 0.8\alpha_g^{1.28} \; if \; \alpha_g <= 0.85 \\ \alpha_g^{2.65} \; if \; \alpha_g > 0.85 \end{cases} \tag{2.40}$$

This model can also be used in a wide range of flow scenarios ranging from dilute to dense. In some of the cases, this model has been used in this work to calculate the interphase momentum exchange coefficient (K_{gs}).

Wen and Yu drag model: In this model proposed by Wen and Yu [93], K_{gs} is calculated as

$$K_{gs} = \frac{3}{4} C_d \frac{\alpha_s \alpha_g \rho_g |\mathbf{u}_g - \mathbf{u}_s|}{d_s} {\alpha_g}^{-2.65} \tag{2.41}$$

where the drag coefficient C_d is calculated as

$$C_d = \frac{24}{\alpha_s \mathrm{Re}_p} \left[1 + 0.15(\alpha_s \mathrm{Re_p})^{0.687}\right] \tag{2.42}$$

This model is generally appropriate for dilute flow conditions.

Kolev drag model: The interphase drag force (f_p) acting between the phases per unit volume is calculated by Kolev [92]as

$$f_p = \rho_g \alpha_s \frac{1}{d_s} \frac{3}{4} C_d |\mathbf{u}_g - \mathbf{u}_s| (\mathbf{u}_g - \mathbf{u}_s) \tag{2.43}$$

This model is appropriate in case of simple dilute flow conditions and not used for dense flow situations like flows in gas-solid fluidized beds.

McKeen drag model: In this model [91], the interphase exchange coefficient is calculated as

$$K_{gs} = C \left(\frac{17.3}{Re_s} + 0.336\right) \frac{\rho_g |\mathbf{u}_s - \mathbf{u}_g|}{d_s} \alpha_s \alpha_g^{-1.8} \tag{2.44}$$

where C is a constant. In earlier published works like Visuri et al. [94], Loha et al. [17], the effects of changing these drag models to calculate the interphase exchange coefficients have been thoroughly discussed for liquid-solid and gas-solid fluidized bed systems. In those studies, it has been found that the results obtained by using Gidaspow [86] and Syamlal-O'Brien [90] drag model were closer to the available experimental data. In the present studies, the effects of changing the drag models have been examined for the problem discussed in Chapter 5 (Section 5.6) and it is found that, for that particular problem, very little difference can be observed when either of Gidaspow and Syamlal-O'Brien models has been used.

2.5 Boundary conditions

The boundary conditions play a major role in obtaining accurate numerical solutions for any set of partial differential equations. The importance of boundary conditions

in case of two-fluid model is significant as there are two distinct phases available in all parts of the domain. In this work, at the inlet of the flow domain, a Dirichlet boundary condition is specified for all the variables other than pressure whereas for pressure, a homogeneous Neumann boundary condition is specified. On the other hand, at outlet, pressure is considered to be atmospheric while all other variables are specified a homogeneous Neumann boundary condition. At solid boundaries, a no-slip condition is specified for the gas phase; whereas for the particle phase, to take care of the momentum loss due to particle-wall collisions, the velocity boundary conditions at solid walls are derived as functions of wall shear stress as given by Johnson and Jackson [14]. It is given as,

$$\tau_{s,w} = -\frac{\pi}{6}\frac{\alpha_s}{\alpha_{s,\max}}\phi\rho_s g_o\sqrt{3\theta}\mathbf{u}_{s,w} \tag{2.45}$$

From Eq. 2.45, the value of $\mathbf{u}_s$ at the wall is calculated. As already stated, ϕ is the specularity coefficient between the particle phase and the wall and g_0 is the radial distribution function which is defined in Eq. 2.18. The value of ϕ can be varied form zero (for perfectly specular collisions, where no momentum is lost) to a value equal to 1 (where the complete particle momentum is lost due to collisions with the wall). Hence, the boundary conditions for the particle velocity on the wall changes according to the value of ϕ. For the volume fraction α_s and α_g of the phases, a homogeneous Neumann boundary condition is specified at the walls. The boundary conditions for particle granular temperature (θ) is given by Johnson and Jackson [14] as

$$q_{\theta,s} = \frac{\pi}{6}\frac{\alpha_s}{\alpha_{s,\max}}\phi\rho_s g_o\sqrt{3\theta}|u_{s,w}|^2 - \frac{\pi}{4}\frac{\alpha_s}{\alpha_{s,\max}}(1-{e_{s,w}}^2)\rho_s g_o\sqrt{3\theta^3} \tag{2.46}$$

where $q_{\theta,s}$ is the granular energy flux at the wall and it can be expressed in terms of θ as

$$q_{\theta,s} = \kappa\frac{\partial\theta}{\partial n} = \frac{\pi}{6}\frac{\alpha_s}{\alpha_{s,\max}}\phi\rho_s g_o\sqrt{3\theta}|u_{s,w}|^2 - \frac{\pi}{4}\frac{\alpha_s}{\alpha_{s,\max}}(1-{e_{s,w}}^2)\rho_s g_o\sqrt{3\theta^3} \tag{2.47}$$

Hence, from Eq. 2.47, the boundary values of θ at the wall are calculated. The values of θ and $\mathbf{u_s}$ at the wall follow from Eqs. 2.46 and 2.47 respectively and are computed using simple explicit finite difference. In Eqs. 2.46 and 2.47, the term $\alpha_{s,max}$ is the maximum packing limit of the particles whose value is taken as 0.63.

2.6 Numerical methodology

In order to solve coupled higher order partial differential equations, numerical techniques such as finite difference method (FDM), finite volume method (FVM) and finite element method (FEM) are usually employed. Finite volume method, owing to its attractive conservation properties, is largely adopted for simulating fluid flow problems. In this work also, this method has been used to solve the governing equations of both the phases.

In finite volume method, the domain is decomposed into a number of non-overlapping small control volumes (also referred to as cells). This process is termed as grid generation and in this work, the unstructured grid generation software GAMBIT [95] is used for this purpose. The geometric information pertaining to the grid needs to be derived to be used in the finite volume framework and this is precisely the role of the preprocessor. The preprocessor calculates all geometric information pertaining to the grid, such as the volume, face areas and surface normals as well as the co-ordinates of the centroids, which appear in the discrete form of the governing equations. In the present work, the focus being on a generic solver, all elemental topologies are handled in a unified manner. The cell shapes could be arbitrary convex polygons but largely consist of tetrahedra, hexahedra, prisms and pyramids for three dimensional scenarios and quadrilateral and triangle for two dimensional scenarios or a combination of two or different types. Figure 2.1 shows different types of cells can be used in the solver. The surface area normal for a polygonal face with n vertices can be calculated as the sum of the cross product of the coordinate vectors of its nodes $\mathbf{V}$ taken in a cyclic manner.

$$\mathbf{S}_f = \sum_{i=1}^{n} \mathbf{V}_i \times \mathbf{V}_{i+1} \tag{2.48}$$

A general approach to volume calculation is also adopted based on the Gauss theorem which defines the cell volume as

$$\Delta V = \frac{1}{3} \sum_{i=1}^{nf} \mathbf{x}_i \cdot \hat{\mathbf{n}}_i \; A_i$$

where nf represents the number of faces, and $\mathbf{x}_i$ is the face center, $\hat{\mathbf{n}}_i$ is its unit normal vector and A_i is the area magnitude of the i^{th} face. The cell centroids are calculated as average of the vertex coordinates and the distance between cell centers

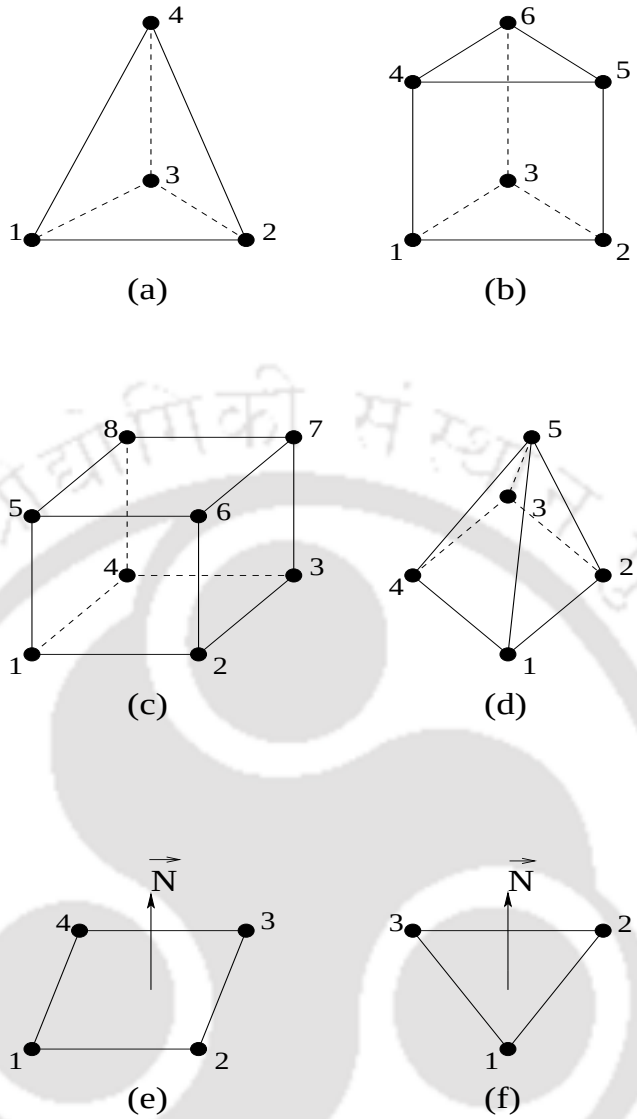

Figure 2.1: Different types of cell. (a) tetrahedron, (b) prism, (c) hexahedron, (d) pyramid, (e) quadrilateral, (f) triangle

sharing a face as well as the normal distance between the center of each cell and its faces are also calculated and stored a priori.

Interpolation

In this work, a collocated arrangement of variables is adopted where all the variables are calculated at cell centers of each control volume. So, in order to calculate the values at the faces of the control volumes, as and when required, interpolation

technique has to be used. Figure 2.2 shows the face "abc" which is shared by two neighboring cells having centers marked as *co* and *nb*. The values of general variable

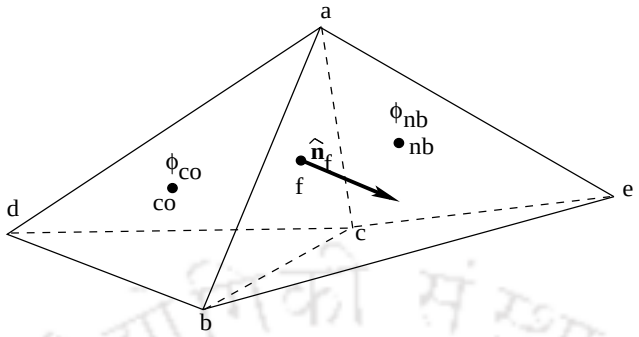

Figure 2.2: Pictorial representation of interpolation technique

ϕ at those cells centroids are denoted as ϕ_{co} and ϕ_{nb} respectively. To calculate the corresponding value of ϕ at the face center f of the face "abc", an inverse volume-weighted linear interpolation method is used which can be written as

$$\phi_f = \frac{\Delta V_{nb}\phi_{co} + \Delta V_{co}\phi_{nb}}{\Delta V_{nb} + \Delta V_{co}} \tag{2.49}$$

where ΔV_{co} and ΔV_{nb} denotes the volumes of the cells having centers *co* and *nb* respectively.

2.7 Discretization procedure

In the present study, the discretization of all the equations is performed using finite volume method (FVM) where the entire solution domain is sub-divided into number of cells (finite volumes). Collocated grid arrangement is used where all the dependent variables are defined at the centroid of the individual cells. FVM uses the integral form of the governing equations. On integrating the differential form of governing equations over the entire flow control volume and applying the Gauss Divergence theorem, the integral form of the governing equations are obtained which may be written for each of the cells based on the following assumptions.

- A cell averaged value is ascribed to the centroid of each control volume.
- A single-point Gauss quadrature is employed for the surface integrals which requires only the face mid-point value of all variables.

A SIMPLE-like algorithm solves the Navier-Stokes equations of both the phases with a face-based data structure and the momentum, volume fraction and pressure equations are solved using a semi-implicit method. The pressure equation is derived from the overall continuity equation which is obtained by adding the continuity equations of both the phases [32] and the pressure-velocity coupling is achieved through momentum interpolation [96]. The numerical approach and the discretization procedure followed in this work are along the lines of Dalal et al. [97]. The details of the solution methodology has been discussed in the subsequent sections with an emphasis on the implementation aspects specific to gas-particulate flows. The general integral forms of the continuity and momentum equations can be written as follows.

Continuity Equation:

The integral form of the continuity equation given in Eq. 2.1 is integrated as shown below.

$$\int_{\Delta V} \frac{\partial \alpha}{\partial t} dV + \int_{\Delta V} \nabla \cdot (\alpha \mathbf{u}) dV = 0 \tag{2.50}$$

Here α and $\mathbf{u}$ will have the suffixes of g and s for gas phase and particle phase, respectively.

Momentum Transport Equation:

The integral form of the momentum equation for a general variable ϕ can be written as

$$\int_{\Delta V} \frac{\partial (\alpha \rho \phi)}{\partial t} dV + \int_{\Delta V} \nabla \cdot (\alpha \rho \mathbf{u} \phi) dV = \int_{\Delta V} -\alpha \nabla p dV + \int_{\Delta V} (\nabla \cdot \alpha \mu \nabla \phi) dV + \int_{\Delta V} S_\phi dV \tag{2.51}$$

2.7.1 Discretization of the continuity equation

The terms in the continuity equation (Eq. 2.1 and Eq. 2.6) are discretized for each cell as given below.

Temporal term

$$\int_{\Delta V} \frac{\partial \alpha}{\partial t} dV \approx \frac{{\alpha_{co}}^{n+1} - {\alpha_{co}}^{n}}{\Delta t} \Delta V_{co} \tag{2.52}$$

where *co* is the cell center of a particular cell of volume ΔV_{co} and ϕ is the value at the cell center *co*.

Convective term

$$\int_{\Delta V} \nabla \cdot (\alpha \mathbf{u}) dV = \int_{\Delta S} (\alpha \mathbf{u}) \cdot d\mathbf{S} \approx \sum_f \alpha_f \mathbf{u}_f \cdot \mathbf{S}_f = \sum_f F_f \alpha_f \tag{2.53}$$

$\mathbf{u}_f$ is the velocity defined at the face center f, $\mathbf{S}_f$ is the surface vector representing the area of that face. F_f is the outward volume flux through face f which is given as

$$F_f = \mathbf{u}_f \cdot \mathbf{S}_f \tag{2.54}$$

The details of the discretization of the convective flux has been discussed later in Section 2.7.2.

2.7.2 Discretization of the momentum equation

The details of the discretization of the temporal term, convective and diffusive fluxes of the momentum equations have been discussed below in details.

Temporal term

The unsteady or temporal term of the momentum equation can be discretized as

$$\int_{\Delta V} \frac{\partial(\alpha\rho\phi)}{\partial t} dV \approx \frac{(\alpha\rho\phi)_{co}^{n+1} - (\alpha\rho\phi)_{co}^{n}}{\Delta t} \Delta V_{co} \tag{2.55}$$

where ΔV_{co} is the volume of the owner cell *co* and the cell-centroidal values of any variable ϕ are assumed to be equal to the cell-averaged quantities.

Treatment of the Convection Fluxes

The convective fluxes are discretized by first converting the volume integral to a surface integral and approximating the later with a single point Gauss quadrature.

$$\int_{\Delta V} \nabla \cdot (\alpha\rho\mathbf{u}\phi) dV = \int_{\Delta S} (\alpha\rho\mathbf{u}\phi) \cdot d\mathbf{S} \approx \sum_f \alpha_f \rho_f \phi_f (\mathbf{u} \cdot \mathbf{S})_f = \sum_f \alpha_f \rho_f F_f \phi_f \tag{2.56}$$

Here the values of ρ_f and α_f are obtained from the cell-centered value using inverse volume-weighted interpolation. ϕ_f is the value of ϕ at the center of face f. Now, in

order to calculate the value of $F_f\phi_f$ for a face f, a weighted average of upwind and central difference scheme is used following the deferred correction approach of Khosla and Rubin [98], so that the problems relating to numerical diffusion and numerical dispersion can be avoided. For a face f, the convective flux can be estimated as a linear combination of upwind and central difference scheme as given below.

$$F_f\phi_f = {(F_f\phi_f)_{UDS}}^{n+1} + \gamma\left[{(F_f\phi_f)_{CDS}}^{n} - {(F_f\phi_f)_{UDS}}^{n}\right] \tag{2.57}$$

where γ is the deferred constant whose value varies in between 0 and 1. Fluxes at faces due to first order upwind scheme (UDS) and central difference scheme (CDS) can be expressed in the following manner.

$${F_f\phi_f}^{UDS} = \phi_{co}[|F_f, 0|] - \phi_{nb}[|-F_f, 0|] \tag{2.58}$$

Here $[|F_f, 0|]$ denotes the the maximum of the two arguments and ϕ_{nb} denotes the value of the variable ϕ in the corresponding neighbor cell. On the other hand, the flux at the face f using CDS can be calculated using inverse volume-weighted interpolation as given below.

$${F_f\phi_f}^{CDS} = F_f\left(\frac{\Delta V_{nb}}{\Delta V_{nb}+\Delta V_{co}}\phi_{co} + \frac{\Delta V_{co}}{\Delta V_{nb}+\Delta V_{co}}\phi_{nb}\right) \tag{2.59}$$

where ΔV_{co} is the volume of the owner cell co and ΔV_{nb} is the volume of the corresponding neighbor cell nb. The first term, i.e., the upwind part at $(n+1)$ time level in Eq. 2.57 is incorporated in the coefficients of the unknown velocity during pressure velocity iteration while the second part is incorporated as source term of the same equation and are evaluated using previous iteration values. The deferred correction approach enhances the diagonal dominance of the coefficient matrix to enhance the stability of the solution algorithm.

Treatment of the diffusive fluxes

The diffusive term in the momentum equation is computed using Green-Gauss reconstruction which is second order accurate. Using Gauss divergence theorem, the diffusive fluxes for a general variable ϕ for a particular face f is calculated in the following manner.

$$\int_{\mathrm{V}} \nabla\cdot(\mu\alpha\nabla\phi)\,\mathrm{dV} = \int_S (\mu\alpha\nabla\phi)\cdot\mathrm{d}\mathbf{S} \approx \sum_f (\mu\alpha\nabla\phi\cdot\mathbf{S})_f = \sum_f F_{d\phi f}$$

where $\mathbf{S}_f$ is the face area vector with a magnitude of A_f and its direction is given by unit vector $\hat{\mathbf{n}}_f$. For orthogonal grid arrangement, this face area vector is parallel to the line joining the adjacent cell centers whereas for non-orthogonal grids, this face area vector is inclined to the line joining the adjacent cell centers as shown in Fig. 2.3. and thus giving rise to the non-orthogonal component of diffusive

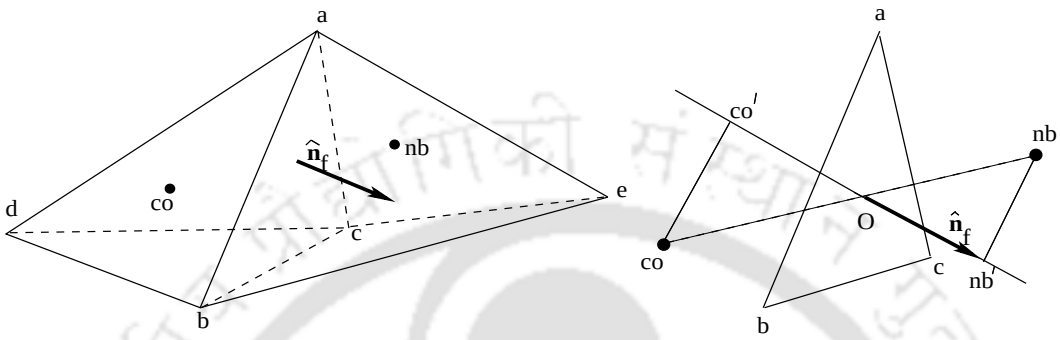

Figure 2.3: Pictorial representation of diffusive flux calculation.

fluxes. This is explained with the help of Fig. 2.3 where the face "abc" is shared by two neighboring tetrahedral cells with centers marked as *co* and *nb*. It can be clearly understood from Fig. 2.3 that the face unit normal represented by $\hat{\mathbf{n}}_f$ is not parallel to the line joining the cell centers *co* and *nb* and thus for this case, along with the normal diffusion, there will be a component of diffusive flux for this non-orthogonality. Projecting the cell centers over the surface normal will result in two more points co' and nb'. For a particular face, the diffusive fluxes for a variable ϕ can be calculated as,

$$(\nabla\phi)_f \cdot \mathbf{S}_f = A_f \, (\nabla\phi)_f \cdot \hat{\mathbf{n}}_f = A_f \frac{(\phi_{\mathrm{nb}'} - \phi_{\mathrm{co}'})}{\Delta n} \tag{2.60}$$

where Δn is the distance between points co′ and nb′. ϕ'_{nb} and ϕ'_{co} are the values of ϕ at the points nb' and co' respectively which can be approximated from the values of ϕ at the points *co* and *nb* using Taylor series expansion, neglecting higher order terms as given below.

$$\phi_{nb'} = \phi_{nb} + \nabla\phi_{nb} \cdot \overrightarrow{nb\ nb'} \tag{2.61}$$

$$\phi_{co'} = \phi_{co} + \nabla\phi_{co} \cdot \overrightarrow{co\ co'} \tag{2.62}$$

Substituting Eqs. 2.61 and 2.62 in Eq. 2.60, finally the expression for the net diffusive flux can be found out as

$$(\nabla\phi)_f \cdot \mathbf{S}_f = A_f \left[\frac{(\phi_{nb} - \phi_{co})}{\Delta n} + \frac{\nabla\phi_{nb} \cdot \overrightarrow{nb\ nb'} - \nabla\phi_{co} \cdot \overrightarrow{co\ co'}}{\Delta n} \right] \tag{2.63}$$

The first part of Eq. 2.63 is the normal or orthogonal component of diffusive fluxes while the second part is mainly appearing due to non-orthogonality of the grids. It is to be noted that for calculating value at the face for any variable ϕ, inverse volume weighted interpolation technique employed by Dalal et al. [97] is used unless otherwise stated.

Source terms and their discretization

In the momentum equations of both the phases, source terms appear and consist of pressure gradient, gravity, drag force terms in both the phases and solid pressure gradient in particle phase alone. The drag force term appearing in the momentum equations of both the phases is treated volumetrically. The gradient of solid pressure term appearing in the particle phase momentum equation is treated using standard Green Gauss approach. The numerical treatment of all the above mentioned source terms appearing in the momentum equation are discussed below.

Pressure gradient and gravity

In this work, in order to obtain a proper force balance between pressure and gravity, a variant of the method first proposed by Perot [99] has been adopted. In this approach, the centroidal quantities are calculated from the respective face centered values, wherein the face normal velocities are utilized to calculate the cell centroidal velocity vector. This concept has been utilized by Manik [100], but instead of calculating the cell centered velocity vector, this method has been successfully applied to calculate cell centroidal values of pressure gradients and other cell centered quantities like gravity forces for interfacial multiphase flows. This approach is termed as Modified Green Gauss (MGG) in [100] and is used for the treatment of pressure and gravity terms in this work. Hence, the pressure gradient at the cell centroid is calculated as

$$\int_{\Delta V} (\alpha\nabla p) dV = \alpha\nabla p \Delta V_{co} = \sum_f \left\{ \alpha_f \left(\frac{\partial p}{\partial n} \right)_f (\mathbf{x}_f - \mathbf{x}_{co}) |\mathbf{S}_f| \right\} \tag{2.64}$$

where the subscripts "*co*" and "*f*" denotes the values at cell center and faces respectively. In a similar way, the gravity term is treated as follows.

$$\int_{\Delta V} (\alpha\rho\mathbf{g})dV = \alpha\rho\mathbf{g}\Delta V_{co} = \sum_f \left\{ \alpha_f \rho_f (\mathbf{g}\cdot\hat{\mathbf{n}})_f (\mathbf{x}_f - \mathbf{x}_{co}) |\mathbf{S}_f| \right\} \tag{2.65}$$

In Eqs. 2.64 and 2.65, $\mathbf{x}$ denotes the co-ordinates of face and cell centroids and $|\mathbf{S}_f|$ represents magnitude of face area vector.

Gradient of solid pressure term

This term exists only in the particle phase momentum equation and the Green Gauss reconstruction is used to discretize it as follows.

$$\int_{\Delta V} -\nabla p_s dV = -\int_S p_s d\mathbf{S} \approx -\sum_f p_{sf}\mathbf{S}_f \tag{2.66}$$

Where p_{sf} is the solid pressure at the face center of and $\mathbf{S}_f$ is the surface area vector of face f. For evaluating solid pressure at the face center, inverse volume interpolation method is used.

Drag force term

This term is present in the momentum equations of both the phases and it is treated volumetrically. This term (denoted by S_ϕ) is integrated over the cell volume as

$$\int_{\Delta V} S_\phi dV \approx (S_\phi)_{co} \Delta V_{co} \tag{2.67}$$

2.8 Discretized form of the governing equations

Using the details of the discretization procedure discussed in Section 2.7, the governing equations of both the phases are discretized. The momentum equations of both the phases have been modified using the idea of partial elimination algorithm (PEA) proposed by Spalding [67]. According to this algorithm, instead of taking the phase velocities of the interphase drag term in previous time step (n) levels in both the equations, it is taken as $K_{gs}(\mathbf{u}_s^n - \mathbf{u}_g^{n+1})$ in gas phase momentum equation and as $K_{gs}(\mathbf{u}_g^n - \mathbf{u}_s^{n+1})$ in particle phase momentum equation.

The momentum equation of the gas phase solved herein in discretized form at $(n+1)$ time level can be written as,

$$\frac{(\rho_g\alpha_g\mathbf{u}_g)_{co}^{n+1}-(\rho_g\alpha_g\mathbf{u}_g)_{co}^{n}}{\Delta t}\Delta V_{co}+\sum_f F_{gf}^{n+1}(\rho_g\alpha_g\mathbf{u}_g)_f^{n+1}+\sum_f F_{dg\mathbf{u}f}^{n+1}= -(\alpha_g\nabla p)_{co}^{n+1}\Delta V_{co}+\{K_{gs}(\mathbf{u}_s^n-\mathbf{u}_g^{n+1})_{co}\Delta V_{co}+(\rho_g\alpha_g^{n+1}\mathbf{g})_{co}\Delta V_{co} \quad (2.68)$$

This may be rearranged to read as,

$$\left(\frac{\rho_g\alpha_g^{n+1}}{\Delta t}+K_{gs}\right)_{co}\Delta V_{co}\mathbf{u}_{g,co}^{n+1}-\left(\frac{\rho_g\alpha_g^{n+1}}{\Delta t}\right)_{co}\Delta V_{co}\mathbf{u}_{g,co}^{n}+\sum_f F_{gf}^{n+1}(\rho_g\alpha_g\mathbf{u}_g)_f^{n+1}+\sum_f F_{dg\mathbf{u}f}^{n+1}=-(\alpha_g\nabla p)_{co}^{n+1}\Delta V_{co}+(K_{gs}\mathbf{u}_s^n)_{co}\Delta V_{co}+(\rho_g\alpha_g^{n+1}\mathbf{g})_{co}\Delta V_{co} \quad (2.69)$$

where the term F_{gf}^{n+1} is the volume flux and $F_{dg\mathbf{u}f}^{n+1}$ is the diffusive flux for the gas phase at a particular face f.

Similarly, the solution form of the particle phase momentum equation can be written as

$$\frac{(\rho_s\alpha_s\mathbf{u}_s)_{co}^{n+1}-(\rho_s\alpha_s\mathbf{u}_s)_{co}^{n}}{\Delta t}\Delta V_{co}+\sum_f F_{sf}^{n+1}(\rho_s\alpha_s\mathbf{u}_s)_f^{n+1}+\sum_f F_{ds\mathbf{u}f}^{n+1}= -(\alpha_s\nabla p)_{co}^{n+1}\Delta V_{co}-(\nabla p_s)_{co}^{n+1}\Delta V_{co}+\{K_{gs}(\mathbf{u}_g^n-\mathbf{u}_s^{n+1})\}_{co}\Delta V_{co}+(\rho_s\alpha_s^{n+1}\mathbf{g})_{co}\Delta V_{co} \quad (2.70)$$

which on rearrangement reads,

$$\left(\frac{\rho_s\alpha_s^{n+1}}{\Delta t}+K_{gs}\right)_{co}\Delta V_{co}\mathbf{u}_{s,co}^{n+1}-\left(\frac{\rho_s\alpha_s^{n+1}}{\Delta t}\right)_{co}\Delta V_{co}\mathbf{u}_{s,co}^{n}+\sum_f F_{sf}^{n+1}(\rho_s\alpha_g\mathbf{u}_s)_f^{n+1}+\sum_f F_{ds\mathbf{u}f}^{n+1}=-(\alpha_s\nabla p)_{co}^{n+1}\Delta V_{co}-(\nabla p_s)_{co}^{n+1}\Delta V_{co}+(K_{gs}\mathbf{u}_g^n)_{co}\Delta V_{co}+(\rho_s\alpha_s^{n+1}\mathbf{g})_{co}\Delta V_{co} \quad (2.71)$$

where the term F_{sf}^{n+1} is the volume flux and $F_{ds\mathbf{u}f}^{n+1}$ is the diffusive flux for the particle phase at a particular face f. This leads to a linear system of equations for both the gas and particle phase flow variables which are solved using the pre-conditioned krylov solvers with the help of library of iterative solvers (LIS) [101].

2.9 Momentum interpolation technique

In this work, a collocated grid arrangement has been used where all the variables are calculated at the cell-centers. In order to avoid the pressure checker board problem in collocated meshes, momentum interpolation technique which is similar to the method proposed by Rhie and Chow [96] has been used. In this approach, a fractional step methodology has been used as in [97] and therefore, the governing equation for an intermediate step (*) between n and $(n+1)$ time levels is constructed by dropping the pressure and gravity terms which reads

$$\left(\frac{\rho_g\alpha_g{}^{n+1}}{\Delta t}+K_{gs}\right)_{co}\Delta V_{co}\mathbf{u}^*_{g,co}-\left(\frac{\rho_g\alpha_g{}^{n+1}}{\Delta t}\right)_{co}\Delta V_{co}\mathbf{u}^n_{g,co}+\sum_f F^*_{gf}(\rho_g\alpha_g\mathbf{u}_g)^*_f+$$

$$\sum_f F^*_{dg\mathbf{u}f}=(K_{gs}\mathbf{u}^n_s)_{co}\Delta V_{co} \tag{2.72}$$

Subtracting Eq. 2.72 from Eq. 2.69 and assuming that the differences in the convective and diffusive terms between the (*) and $(n+1)$ levels may be neglected, we get for a cell with centroid co,

$$\left(\frac{\rho_g\alpha_g{}^{n+1}}{\Delta t}+K_{gs}\right)\mathbf{u}^{n+1}_g-\left(\frac{\rho_g\alpha_g{}^{n+1}}{\Delta t}+K_{gs}\right)\mathbf{u}^*_g=-\alpha^{n+1}_g\nabla p^{n+1}+\rho_g\alpha^{n+1}_g\mathbf{g} \tag{2.73}$$

or

$$\mathbf{u}^{n+1}_g-\mathbf{u}^*_g=-A\nabla p^{n+1}+A\rho_g\mathbf{g} \tag{2.74}$$

where A is defined as

$$A=\left(\frac{\alpha^{n+1}_g}{\frac{\rho_g\alpha_g{}^{n+1}}{\Delta t}+K_{gs}}\right) \tag{2.75}$$

Taking divergence of both the sides of Eq. 2.74 and integrating gives,

$$\int_{\Delta V}\nabla\cdot\mathbf{u}_g{}^{n+1}dV-\int_{\Delta V}\nabla\cdot\mathbf{u}_g{}^*dV=-\int_{\Delta V}\nabla\cdot(A\nabla p)^{n+1}dV+\int_{\Delta V}\nabla\cdot(A\rho_g\mathbf{g})dV \tag{2.76}$$

This may be simplified using Gauss-Divergence theorem to get,

$$\int_{\Delta S}\mathbf{u}_g{}^{n+1}\cdot d\mathbf{S}-\int_{\Delta S}\mathbf{u}_g{}^*\cdot d\mathbf{S}=-\int_{\Delta S}(A\nabla p^{n+1})\cdot d\mathbf{S}+\int_{\Delta S}(A\rho_g\mathbf{g})\cdot d\mathbf{S} \tag{2.77}$$

Rewriting Eq. 2.77 by replacing the surface integrals by Gauss quadrature gives,

$$\sum_f\mathbf{u}^{n+1}_{gf}\cdot\mathbf{S}_f=\sum_f\mathbf{u}^*_{gf}\cdot\mathbf{S}_f-\sum_f(A\nabla p^{n+1})_f\cdot\mathbf{S}_f+\sum_f(A\rho_g\mathbf{g})_f\cdot\mathbf{S}_f \tag{2.78}$$

The final form of the equation therefore reads,

$$\sum_f F_{gf}^{n+1} = \sum_f F_{gf}^{*} - \sum_f \left(A\nabla p^{n+1}\right)_f \cdot \mathbf{S}_f + \sum_f \left(A\rho_g \mathbf{g}\right)_f \cdot \mathbf{S}_f \tag{2.79}$$

which is the momentum interpolation formula for the gas phase where F_{gf}^{n+1} and F_{gf}^{*} are the fluxes of $\mathbf{u}_g^{n+1}$ and $\mathbf{u}_g^{*}$ respectively.

In an exactly similar way, the momentum interpolation formula for the particle phase can be derived and is obtained as

$$\sum_f F_{sf}^{n+1} = \sum_f F_{sf}^{*} - \sum_f \left(B\nabla p^{n+1}\right)_f \cdot \mathbf{S}_f + \sum_f \left(B\rho_s \mathbf{g}\right)_f \cdot \mathbf{S}_f \tag{2.80}$$

where B is defined as

$$B = \left(\frac{\alpha_s^{n+1}}{\dfrac{\rho_s \alpha_s^{n+1}}{\Delta t} + K_{gs}} \right) \tag{2.81}$$

2.10 Derivation of the pressure equation

The pressure equation for this type of flow is obtained from the overall continuity equation which is obtained by adding the continuity equations of both the phases [32]. Thus adding the continuity Eqs. 2.2 and 2.6 and integrating gives,

$$\int_{\Delta V} \frac{\partial \alpha_g}{\partial t} dV + \int_{\Delta V} \nabla \cdot (\alpha_g \mathbf{u}_g) dV + \int_{\Delta V} \frac{\partial \alpha_s}{\partial t} dV + \int_{\Delta V} \nabla \cdot (\alpha_s \mathbf{u}_s) dV = 0 \tag{2.82}$$

Replacing the temporal derivatives using volume averaged quantities (as shown in Eq. 2.52) and applying Gauss-Divergence Theorem on the divergence terms (as shown in Eq. 2.53) give,

$$\frac{\left({\alpha_g}^{n+1} + {\alpha_s}^{n+1}\right) - \left({\alpha_g}^{n} + {\alpha_s}^{n}\right)}{\Delta t} \Delta V_{co} + \sum_f {\alpha_{gf}}^{n+1} {F_{gf}}^{n+1} + \sum_f {\alpha_{sf}}^{n+1} {F_{sf}}^{n+1} = 0 \tag{2.83}$$

which may be further simplified by applying that at any cell centroid, the term $\alpha_g + \alpha_s$ is equal to 1 at all time levels which leads to,

$$\sum_f {\alpha_{gf}}^{n+1} {F_{gf}}^{n+1} + \sum_f {\alpha_{sf}}^{n+1} {F_{sf}}^{n+1} = 0 \tag{2.84}$$

Substituting the mometum interpolation formulae (Eqs. 2.79 and 2.80) into Eq. 2.84 and after rearranging, the final form of the pressure equation is obtained as given below.

$$\sum_f {\alpha_{gf}}^{n+1} {F_{gf}}^* + \sum_f {\alpha_{sf}}^{n+1} {F_{sf}}^* + \sum_f \left(A\alpha_g\rho_g\mathbf{g}\right)_f \cdot \mathbf{S}_f + \sum_f \left(B\alpha_s\rho_s\mathbf{g}\right)_f \cdot \mathbf{S}_f = \sum_f \left\{ \left(A\alpha_g + B\alpha_s\right)_f \left(\nabla p\right)_f^{n+1} \cdot \mathbf{S}_f \right\} \quad (2.85)$$

2.11 Solution algorithm

As already mentioned, the overall solution approach of the gas-particulate flow solver developed in this work is based on fractional step methodology in a collocated finite volume framework. The overall solution algorithm of the solver may be summarized as follows.

1. Initialize all variables.
2. At the start of (n+1) time step, it is assumed that ${F_{gf}}^{n+1}={F_{gf}}^*$ and ${F_{sf}}^{n+1}={F_{sf}}^*$.
3. Solve for the particle phase volume fraction equation (Eq. 2.6) to calculate ${\alpha_s}^{n+1}$.
4. Calculate gas phase volume fraction as ${\alpha_g}^{n+1}=1-{\alpha_s}^{n+1}$.
5. Solve the granular temperature (θ) using Eq. 2.12 and calculate the values of solid pressure (p_s) and solid phase viscosity (μ_s) using Eqs. 2.17 and 2.20.
6. Solve for provisional velocities ($\mathbf{u}_g{}^*$) for the gas phase by iterating the gas phase velocity equations without pressure and gravity term and calculating flux for the provisional velocities as $F^*_{gf} = \mathbf{u}_{gf}{}^* \cdot \mathbf{S}_f$.
7. Solve for provisional velocities ($\mathbf{u}_s{}^*$) for the particle phase by iterating the particle phase velocity equations without pressure and gravity term and calculating flux for the provisional velocities as $F^*_{sf} = \mathbf{u}_{sf}{}^* \cdot \mathbf{S}_f$.
8. Solve the pressure equation (Eq. 2.85) to get the updated pressure p^{n+1}.

9. Calculate the volume fluxes (F_{gf}^{n+1} and F_{sf}^{n+1}) for the gas and the particle phases by momentum interpolation formulae given in Eqs. 2.79 and 2.80 respectively.

10. Calculate the phase velocities (${\mathbf{u}_g}^{n+1}$ and ${\mathbf{u}_s}^{n+1}$) using the updated pressure and the fluxes using the following expressions.

$$\mathbf{u}_g^{n+1} - \mathbf{u}_g^{*} = -A\nabla p^{n+1} + A\rho_g \mathbf{g} \tag{2.86}$$

and

$$\mathbf{u}_s^{n+1} - \mathbf{u}_s^{*} = -B\nabla p^{n+1} + B\rho_s \mathbf{g} \tag{2.87}$$

11. Repeat steps (2) to (10) till stopping criterion is satisfied.

This solution algorithm is implemented to develop the indigenous finite volume flow solver for gas-particulate flows and the various stages of development of the solver can be listed as follows.

- **Stage 1**: Development of laminar dilute gas-particle flow solver using one-way coupling between the phases.
- **Stage 2**: Development of laminar dilute gas-particle flow solver using two-way coupling between the phases.
- **Stage 3**: Development of the generalized gas-particle flow solver which can handle all ranges of flow conditions.
- **Stage 4**: Development of the dispersed gas-particle flow solver using three-way coupling between the phases (Addition of KTGF model).
- **Stage 5**: Addition of frictional stress model into the solver in combination with KTGF model to take care of dense gas-particle flows.
- **Stage 6**: Application of the solver in the flows in bubbling gas-solid fluidized beds.

These six stages represent the chronological order of development, validation and application of the flow solver and forms the core of the present thesis.

2.12 Closure

In this chapter, the details of the governing equations of both the phases and their discretization procedure have been discussed. The importance of implementing the KTGF model, frictional stress model and different drag models have also been discussed. The details of derivation of the momentum interpolation formulae for both the phases and the derivation of the pressure equation from the phase continuity equations have also been illustrated in details. The chapter ends with the details of the solution algorithm.

Chapter 3

Validation of the flow solver

In this chapter, a detailed validation of the inhouse flow solver which is developed using the Eulerian-Eulerian two-fluid model (as discussed in Chapter 2) has been presented. As the solver has been indigenously developed, so during the course of the development of the solver, it has been validated at each and every stage to check its accuracy. In this chapter, the stage by stage validation of the flow solver is presented for all range of flow conditions (ranging from dilute to dense) considering one-way, two-way and three-way coupling between the phases. The importance of the KTGF model and the need of including the frictional stress model for dense gas-particulate flow situations are also demonstrated.

3.1 Validation for one-way coupling

As already discussed in Chapter 1, one-way coupling refers to the flow scenario where particle phase is affected by the continuous gas phase but not vice-versa. In order to validate the flow solver for one-way coupling, the following two test cases have been considered.

- Particles released at a very low velocity into a uniform fluid flow field.
- Particles falling freely into a quiescent gas medium.

In both the cases, the solution obtained from the developed solver is compared with the solution of the Lagrangian formulation given in Dasgupta [102].

3.1.1 Particles released at a very low velocity into a uniform fluid flow field

In this test case, it is considered that the dispersed phase particles enter with a low velocity into a wall-free gas flow domain as shown in Fig. 3.1, where the continuous

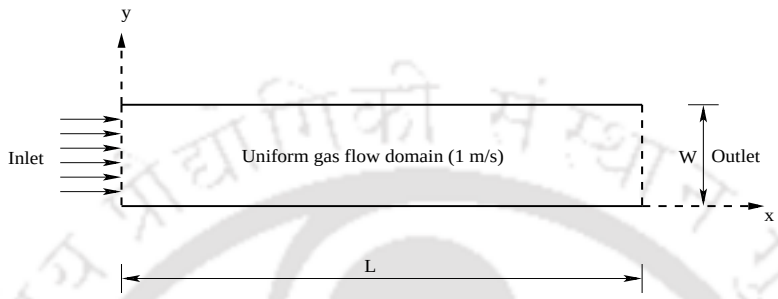

Figure 3.1: The schematic of particles entering at a low velocity into a uniform gas flow domain.

gas phase flows with a uniform horizontal velocity of 1 m/s. The particles enter the domain with a velocity of 0.1 m/s and inlet volume fraction of 0.005. The gas phase is considered to be air with density 1.2 kg/m^3 and the particle phase is considered to have a density of 665 kg/m^3. The length of the channel (L) is 4 m and width (W) is 0.5 m. The effect of gravity is not considered in this problem.

For the above stated parameters, the variations of particle phase velocity along the the length of the domain are studied for two sets of particle diameters of 200 μm and 400 μm respectively and compared with the results obtained by using Lagrangian model in Figs. 3.2 (a) and (b). In order to check the ability of the solver to handle both orthogonal and non-orthogonal meshes, two grids are considered, a Cartesian mesh with 1600 quadrilateral cells and a non-orthogonal mesh with 3474 triangular cells, keeping the the grid resolution almost same for both the cases. It can be observed that for both the meshes, the particles having a higher diameter have to move a greater distance downstream of the domain before attaining a constant velocity. A very good agreement with the results obtained from the Lagrangian model given in Dasgupta [102] can be observed in Figs. 3.2 (a) and (b) for both the values of particle diameters.

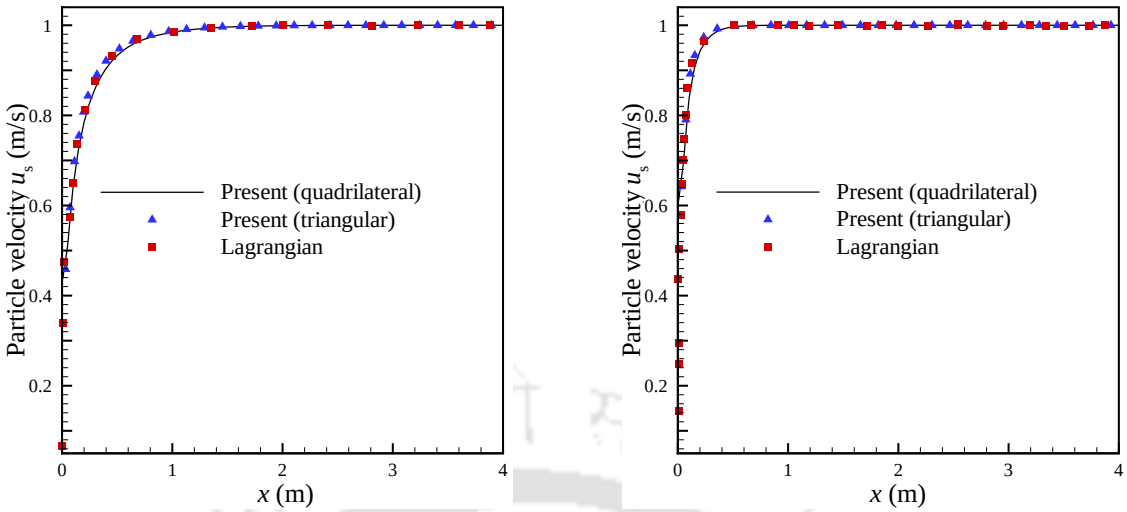

Figure 3.2: Particle phase velocity variation along the length of the domain for particles with a diameter of (a) 400 μm, (b) 200 μm compared with [102].

3.1.2 Particles falling freely into a quiescent gas medium

The second test considers the case of particles falling freely under the effect of gravity into a quiescent gas medium. The schematic diagram of the problem is shown in Fig. 3.3. In this case, the quiescent fluid medium is considered to be air with

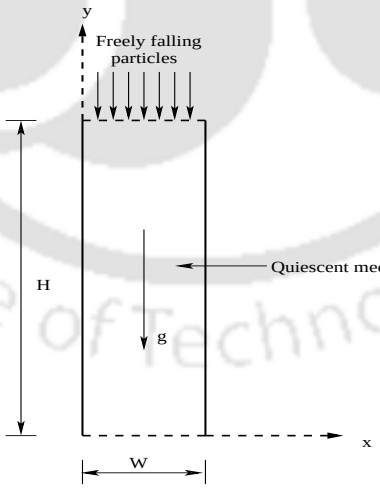

Figure 3.3: The schematic of particles falling freely into a quiescent medium.

density 1.2 kg/m^3. The height of the domain (H) is taken to be equal to 4 m and

the width (W) has been considered as 0.5 m. Simulations have been carried out on a computational grid having 1600 uniform quadrilateral cells. The solver has been tested for two different particle densities- 665 kg/m^3 and 2990 kg/m^3 respectively. The former corresponds to the density of n-heptane particles and the later is close to the density of glass beads. The dispersed phase particles are released into the quiescent air medium at a very low velocity (equal to 0.0001 m/s). The particles move under the influence of gravity.

The test is performed for two sets of particle diameters 200 μm and 400 μm and the numerical solutions obtained from the developed solver and Lagrangian model given in Dasgupta [102] are compared in Figs. 3.4 (a) and (b). The solutions show a

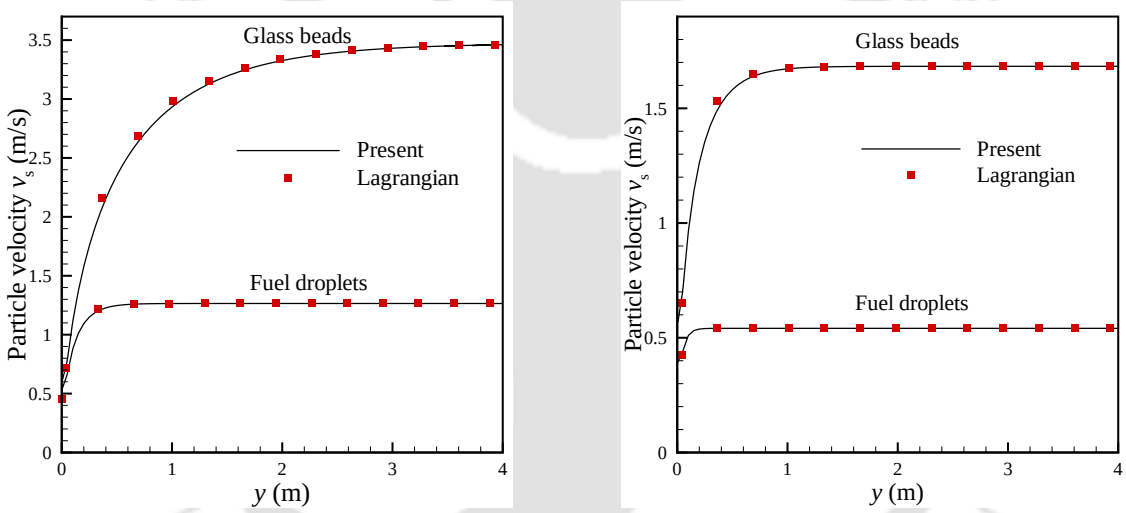

Figure 3.4: Particle phase velocity variation along the flow direction for freely falling particles for a diameter of (a) 400 μm, (b) 200 μm compared with [102].

very good agreement, thereby demonstrating that the solver is capable of simulating dilute laminar gas-particle flows.

These two test cases together conclusively demonstrate that the implementation of one-way coupling in the proposed flow solver is indeed correct and the solver can be used to simulate dilute laminar gas-particle flows quite accurately.

3.2 Validation for two-way coupling

As already discussed, two-way coupling refers to the flow situation where both gas and particle phases have effect on each other. The test case of dispersed laminar gas-particle flow over a two dimensional backward facing step has been considered in order to study the two-way coupling characteristics of the proposed flow solver. It is to be marked that in this case, the interactions of both the phases on each other are taken into account. However, particle-particle and particle-wall interactions are not considered.

The problem of dispersed laminar gas-particle flow past a backward facing step (given in Barton [38]) is simulated using the flow solver. The schematic of the domain has been shown in Fig. 3.5. In this problem, an entrance length of $3h$ is added to prevent downstream effects travelling upstream, where h is the height of the step with the main channel being $32h$ long. Figure 3.5 also illustrates the lower recirculation length x_1 and upper recirculation lengths x_2 and x_3 respectively inside the domain. A flow situation is considered where both the phases have an equal

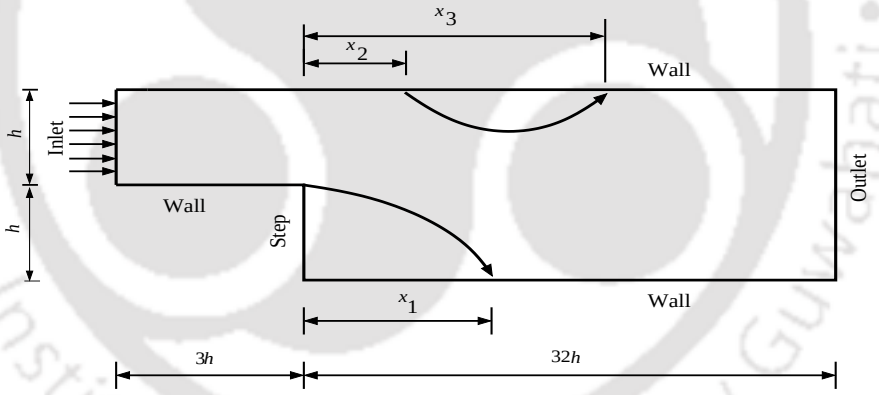

Figure 3.5: Schematic of the backward facing step problem

inlet velocity of 1 m/s. The ratio of the particle density to the fluid density is taken to be equal to 10 as given in [38]. The flow Reynolds number based on the channel height (h) is chosen as 400. A grid with 7600 quadrilateral cells is used to discretize the domain with clustering near the solid boundaries. Simulations are carried out to study the variations of recirculation lengths with Stokes number (St) at a constant particle phase volume fraction (α_s) of 0.0005 and the variations of recirculation lengths with particle phase volume fraction (α_s) at a particular Stokes number (St)

of 10^{-3}. The results obtained from the present solver have been compared with those

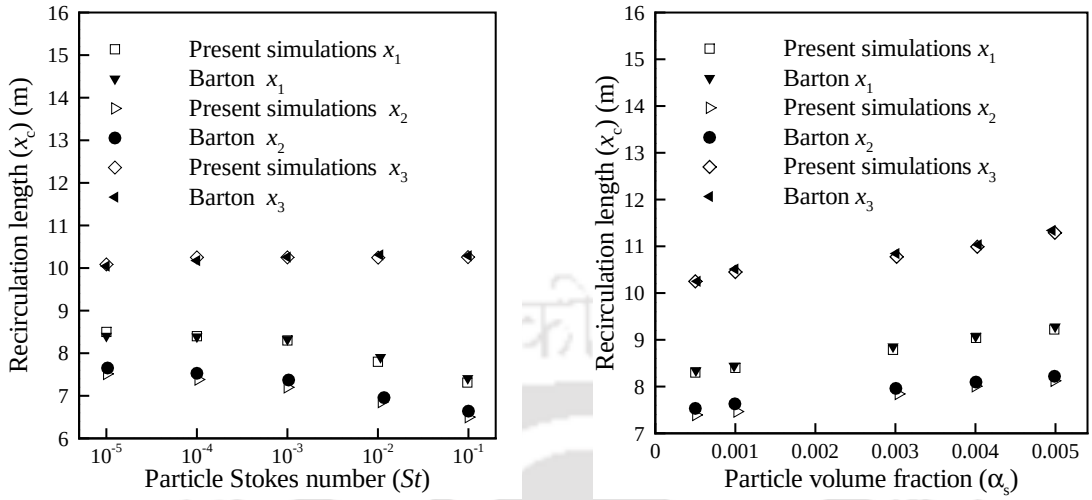

Figure 3.6: Variations in the recirculation lengths (a) with Stokes number at volume fraction 0.0005, (b) with particle phase volume fraction at Stokes number 10^{-3}; compared with [38].

obtained by Barton [38] in Fig. 3.6 (a) and (b). The variation of recirculation length (x_c) with St for α_s=0.0005 has been shown in Figs. 3.6 (a) and the variation of x_c with $\alpha_s$for St=10^{-3} has been shown in Fig. 3.6 (b). It can be seen from the plots that the agreement is excellent which validates the developed solver for gas-particle flows with two-way coupling.

3.3 Validation for three-way coupling

The importance of three-way coupling for practical flow problems including gas-solid fluidized beds makes it necessary to perform validation studies of the flow solver to check its ability to handle particle-particle and particle-wall interactions. Kinetic theory for granular flows (KTGF) model is incorporated into the flow solver to take account of particle-particle and particle wall interactions. It has been observed that in case of dense flow situations, the frictional stresses generated due to the contact of the particles become very high. In these cases, KTGF alone is not sufficient to adequately describe the flow. So, in addition to KTGF, frictional stress model is

also incorporated into the solver to take care of the stresses generated due to close packing of particles in case of dense flow situations. The following test cases have been considered for performing validation studies of the proposed flow solver for three-way coupling.

3.3.1 Dispersed laminar gas-particle flow through a vertical channel

Simulations of dispersed gas-particle flow in a vertical channel of height H and width W are performed as carried out by Passalacqua and Fox [43]. The schematic of the channel is shown in Fig. 3.7. In this problem, the inlet velocity of both the phases

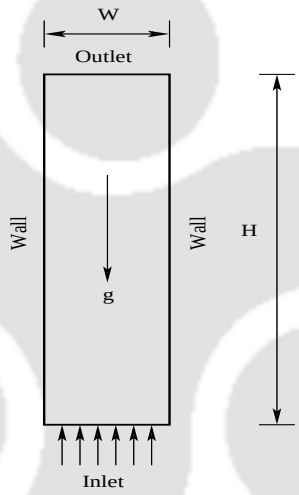

Figure 3.7: Schematic of vertical channel used for validation of three-way coupling.

is fixed at 2.0 m/s and the flow Reynolds number is set equal to 1378 which is lower than its transition value to turbulence for a single-phase flow between two parallel plates. The flow Reynolds number is adjusted by changing the viscosity of the carrier phase. The gas phase is considered to be air with density equal to 1.2 kg/m^3 and particle phase has a density of 1500 kg/m^3. The height of the channel (H) is 1 m and width (W) is 0.1 m. The domain is meshed with 2000 quadrilateral cells as given in [43]. Numerical simulations for a set of particles having a value of particle Stokes number 0.61 has been carried out. The corresponding particle diameter based on this value of Stokes number is 252 μm. The simulations are performed for two different values of inlet particle phase volume fractions 0.0001 and 0.01. The value of

particle-particle restitution coefficient (e) is set to unity (perfectly elastic collisions) and the walls are considered to be specularly reflective (with the value of ϕ set to zero). Both drag and gravity have been considered in the simulations. The steady state gas and particle velocity profiles are compared at midplane (H=0.5 m) of the channel (as shown in Figs. 3.8(a) and (b)) with those given in [43] and a reasonably good agreement is observed with the results in published literature.

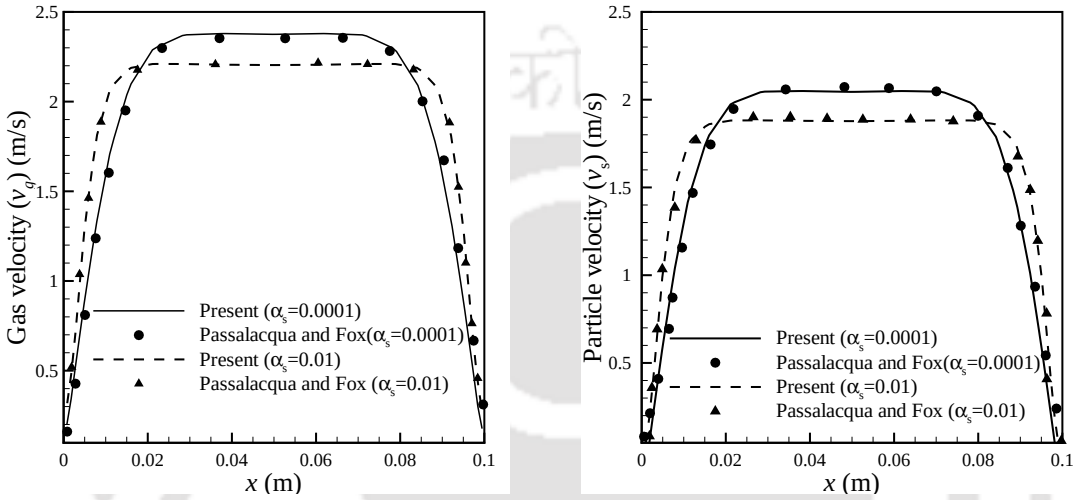

(a) (b)

Figure 3.8: Comparison of plots of steady state (a) gas velocity, (b) particle velocity in the midplane of the vertical channel with [43].

3.3.2 Dispersed laminar gas-particle flow through a horizontal channel

In the previous test case, the value of particle-particle restitution coefficient (e) is set to unity (perfectly elastic collisions) and walls are considered to be specularly reflective (the value of ϕ is set to zero). So, in order to check the capability of the flow solver to handle inelastic particle-particle collisions as well as finite wall roughness, a test case of dispersed gas-particle flow through a horizontal channel is considered. The schematic of the channel is shown in Fig. 3.9. The length of the channel (L) is considered to be 0.4 m and width (W) is considered as 0.155 m. The gas phase density is considered to be equal to 1.2 kg/m^3 and the particle phase has a density

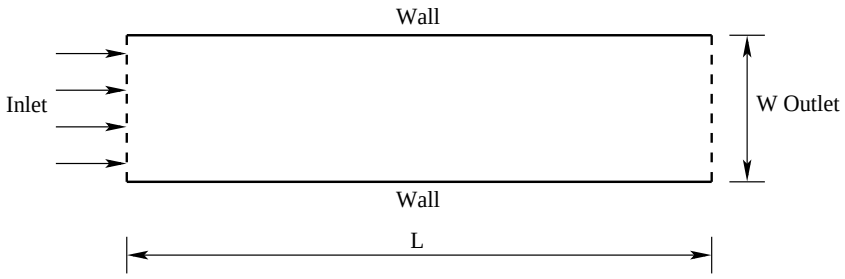

Figure 3.9: Schematic of horizontal channel used for validation of the solver with three-way coupling.

of 2500 kg/m^3. Numerical simulations are carried out in this horizontal channel for an inlet particle phase volume fraction of 0.1. The value of specularity coefficient (ϕ) is considered to be equal to 0.3 and the value of particle-particle restitution coefficent (e) is taken to be 0.9. Both phases are considered to enter the channel with a velocity equal to 1 m/s. The flow Reynolds number based on the channel width is considered to be equal to 200.

Simulations are carried out using a non-orthogonal grid, shown in Fig. 3.9, having 5606 triangular cells in order to check the capability of the developed solver to handle non-orthogonal unstructured grids. The steady state gas and particle

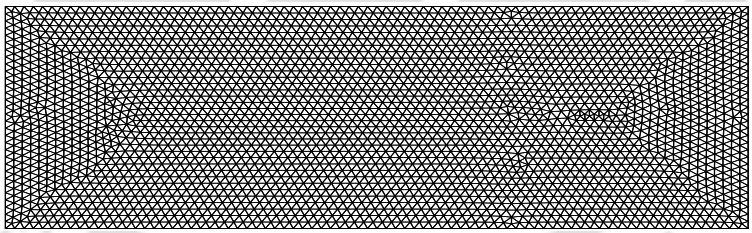

Figure 3.10: Grid with 5606 triangular cells used for the validation of three-way coupling.

velocity profiles as well as particle volume fraction profiles at the midplane of the channel (H=0.2 m) obtained from the present solver are compared in Figs. 3.11 (a), (b), (c) with those obtained from Ansys Fluent [78] using the same set of simulation parameters and computational grid. The results show a very good agreement. Also, the contours of steady state gas and particle velocities obtained from both the solvers are shown in Figs. 3.12 (a) and (b) and an overall excellent agreement can be seen

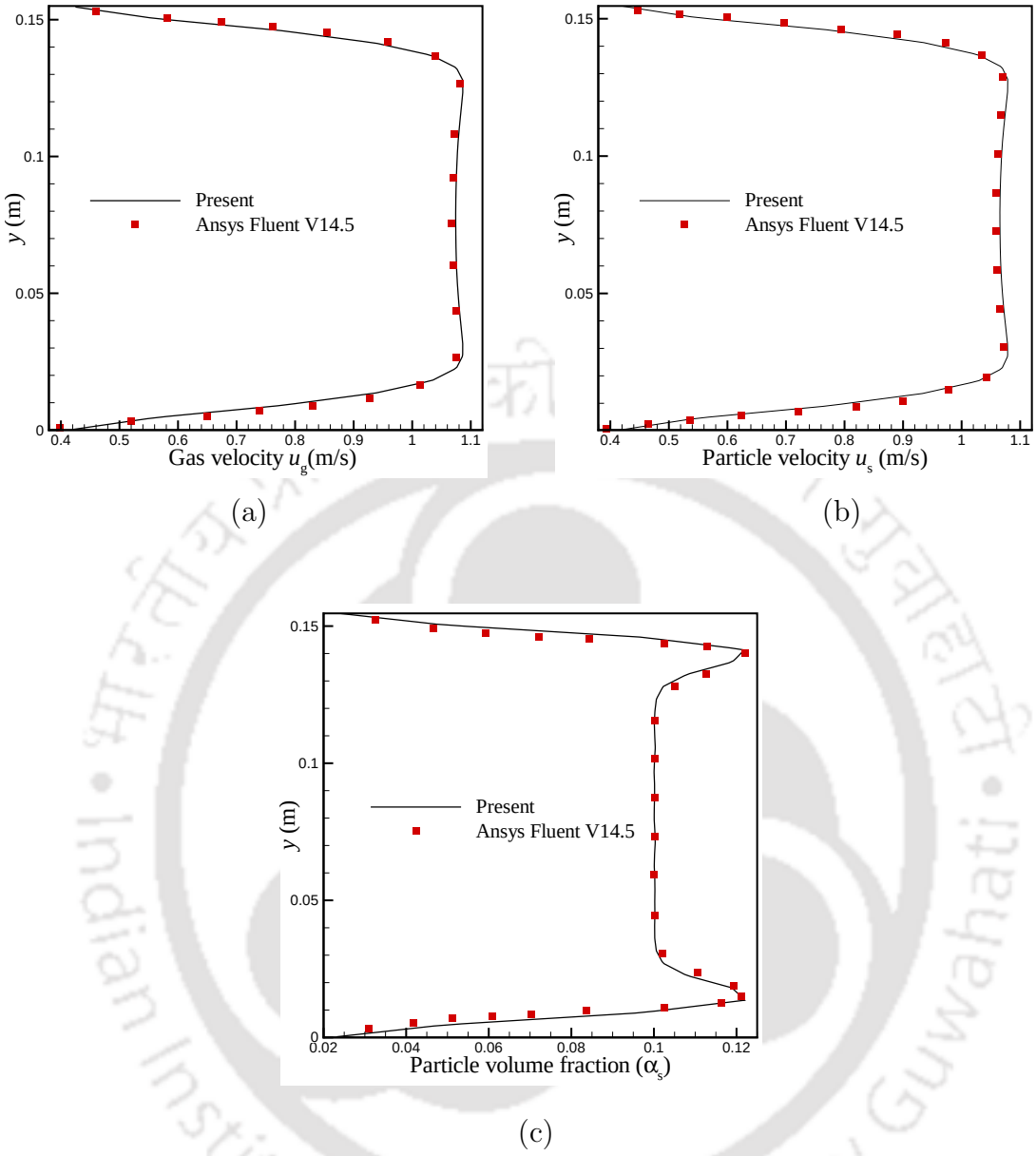

Figure 3.11: Comparison of plots of steady state (a) gas velocity, (b) particle velocity, (c) particle phase volume fraction at the midplane of the channel obtained from present simulations and Ansys Fluent

from the results obtained from both the solvers. Both in Figs. 3.11 and 3.12, a good agreement can be seen in the solutions obtained from both the solvers. These two test cases show that the developed solver can give accurate solutions for gas-particle flows with three-way coupling with KTGF model.

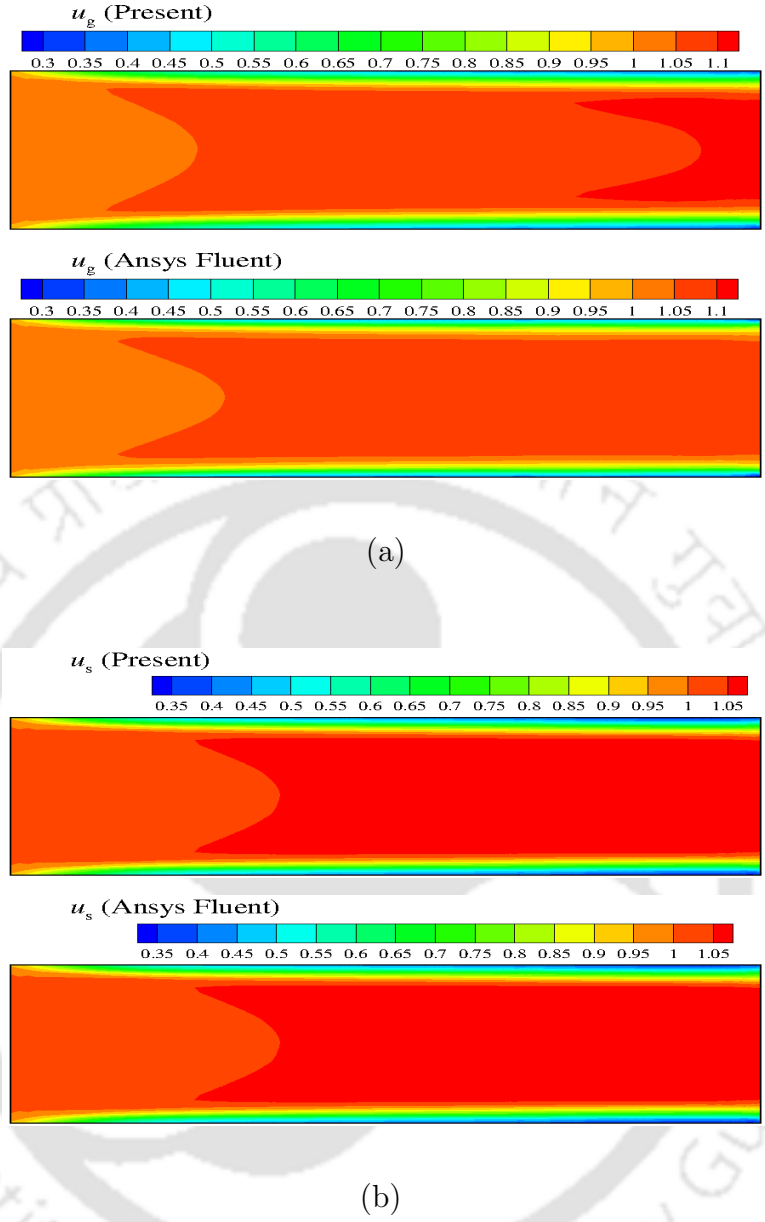

Figure 3.12: Comparison of contours of steady state (a) gas velocity, (b) particle velocity (in m/s) obtained from present simulations and Ansys Fluent

3.3.3 Settling suspension under the effect of gravity

This problem discusses the homogeneous settling of a gas-particle suspension inside a vertical column under the effect of gravity. In order to examine the ability of the solver to handle flows where there is a rapid variation of particle volume fraction, this problem has been taken up. The physical parameters of this problem are taken

from Passalacqua and Fox [103]. The schematic of the problem is shown in Fig. 3.13 which shows a vertical channel of length L=0.3 m and width W=0.05 m, with an initial particle volume fraction equal to 0.3 in the whole domain. The simulation

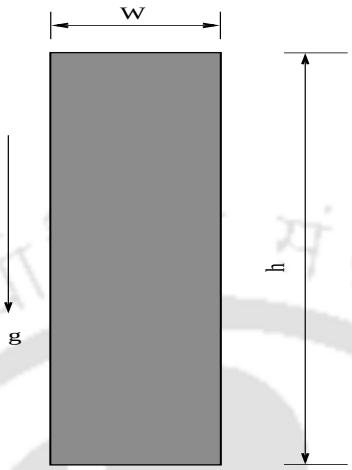

Figure 3.13: The schematic diagram of the domain of settling suspension.

parameters have been listed in Table 3.1.

Table 3.1: Parameters used for simulation of the settling suspension case

Simulation parameters	Values
Channel height (H)	0.3 m
Channel width (W)	0.05 m
Initial Particle volume fraction (α_s)	0.3
Gas density (ρ_g)	1.2 kg/m^3
Particle density (ρ_s)	2000 kg/m^3
Particle diameter (d_s)	400 μm
Particle restitution coefficent (e)	0.9
Maximum packing limit ($\alpha_{s,max}$)	0.63
Minimum volume fraction ($\alpha_{s,min}$)	0.5

When this case was simulated using the flow solver for three-way coupling but employing only the KTGF model, it has been found that the simulation ran only upto 0.0514 s of physical time and after which the linear system of equations pertaining to phase velocities and volume fraction did not converge leading to a numerically unstable solution procedure. The volume fraction contours for this case upto 0.05 s have been shown below.

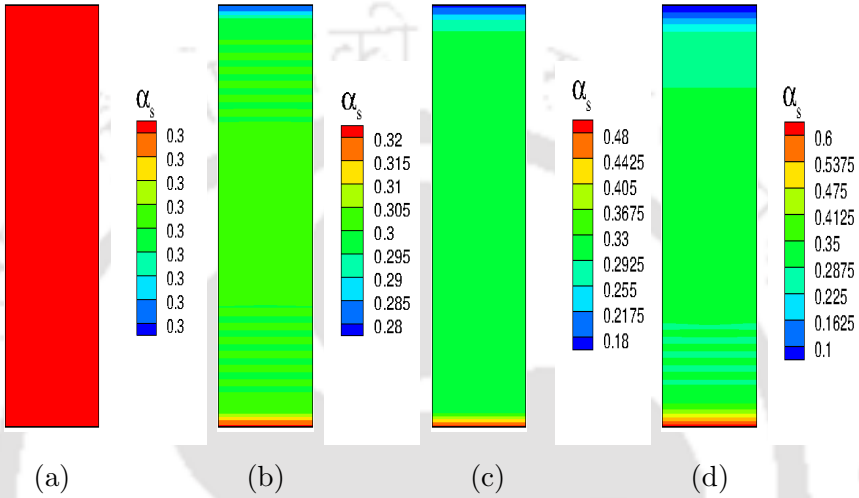

Figure 3.14: Contours of instantaneous particle volume fractions obtained at (a) t=0 s, (b) t=0.01 s, (c) t=0.03 s, (d) t=0.05 s using only KTGF

It can be observed from Fig. 3.14 that the particles tend to fall due to gravity and as a result, the particle volume fraction at the bottom increases very quickly with time. The reason behind the inability of the solver to go beyond 0.0514 s of simulation time is that after 0.05 s (as seen in Fig. 3.14 (d)), the volume fraction tends to reach a value equal to the maximum packing limit ($\alpha_{s,max}$) which leads to unphysically high value of radial distribution function (g_0, Eq. 2.18) which in turn makes the simulations unstable. This clearly shows that the KTGF model alone can not handle dense gas-particulate flows where particle volume fraction is close to the packing limit.

To overcome this difficulty, it is necessary to incorporate the frictional stress model into the solver in addition to KTGF. In this model, as described in Section 2.3, frictional solid pressure ($p_{s,f}$) and frictional solid phase viscosity ($\mu_{s,f}$) are de-

fined and added to the solid pressure (p_s) and and particle phase shear viscosity(μ_s) which are calculated from KTGF, when the particle volume fraction exceeds minimum volume fraction ($\alpha_{s,min}$). The problem is simulated again using KTGF in conjunction with the frictional stress model and it has been found that the frictional stress model helps in keeping the particle phase volume fraction within the packing limit and the simulations can be run for the desired period of time. After overcoming this difficulty, this problem is simulated again with the flow solver using orthogonal, non-orthogonal and hybrid grids and in all the three grids, the number of cells have been kept closer to that used by Passalacqua and Fox [103] such that the results can be compared with those given in [103].

The instantaneous contours of particle phase volume fraction for each of the three grids are shown in Figs. 3.15, 3.16 and 3.17 upto a physical time of 0.6 s.

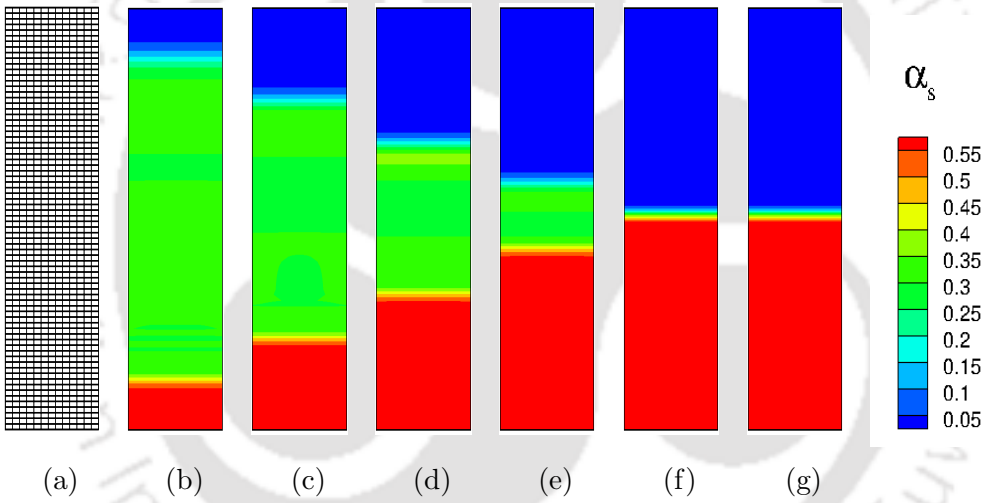

Figure 3.15: (a) Computational grid with orthogonal quadrilateral cells, contours of particle phase volume fractions obtained at (b) t=0.1 s, (c) t=0.15 s, (d) t=0.2 s, (e) t=0.25 s, (f) t=0.3 s, (g) t=0.6 s; from the grid having orthogonal quadrilateral cells.

For each of the three grids, similar variations in the contours of the particle phase volume fraction can be observed with time. The particle phase starts to settle at the bottom of the column where the volume fraction quickly increases and reaches a value very close to the packing limit ($\alpha_{s,max}$). At physical time t=0.3 s, the particle phase gets completely settled and hence, there is no significant variation of volume

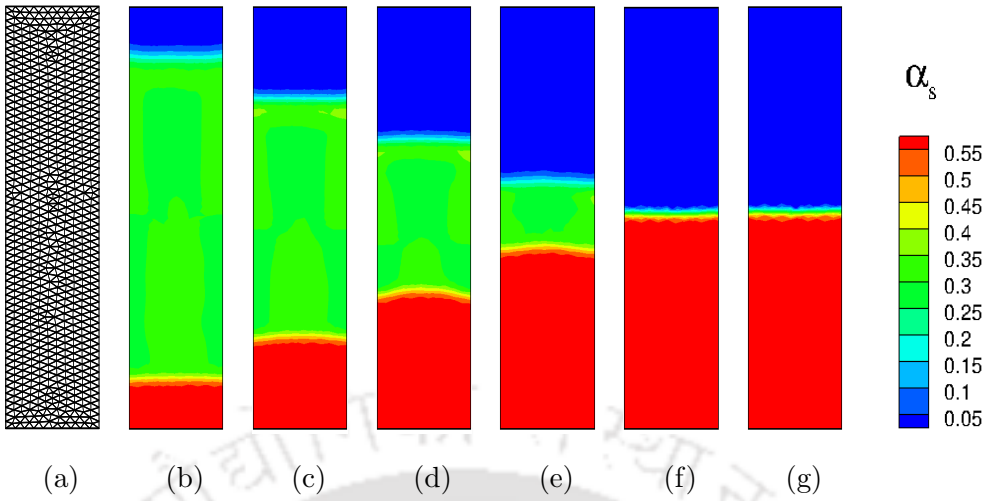

Figure 3.16: (a) Computational grid with triangular cells, contours of particle phase volume fractions obtained at (b) t=0.1 s, (c) t=0.15 s, (d) t=0.2 s, (e) t=0.25 s, (f) t=0.3 s, (g) t=0.6 s; from the grid having triangular cells.

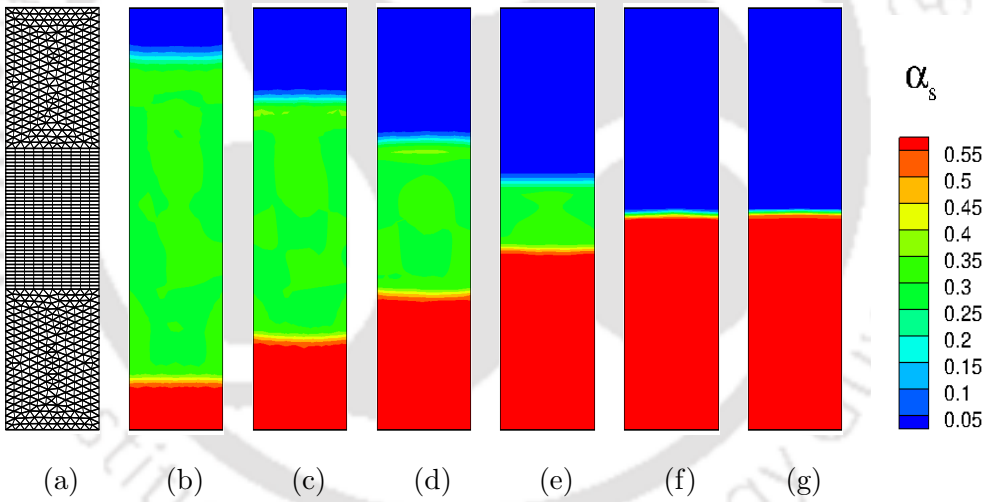

Figure 3.17: (a) Computational grid with hybrid cells, contours of particle phase volume fractions obtained at (b) t=0.1 s, (c) t=0.15 s, (d) t=0.2 s, (e) t=0.25 s, (f) t=0.3 s, (g) t=0.6 s; from the grid having hybrid cells.

fraction contours taking place afterwards in each of the three grids shown in Figs. 3.15, 3.16 and 3.17. Also, the variation of particle phase volume fraction along the vertical centerline of the channel at different time instances obtained from the

present computations are compared with those obtained from Passalacqua and Fox [103] in Figs. 3.18 (a), (b) and (c) who solved it using open source code OpenFOAM [79]. It can be observed from that the variation of centerline particle volume fraction

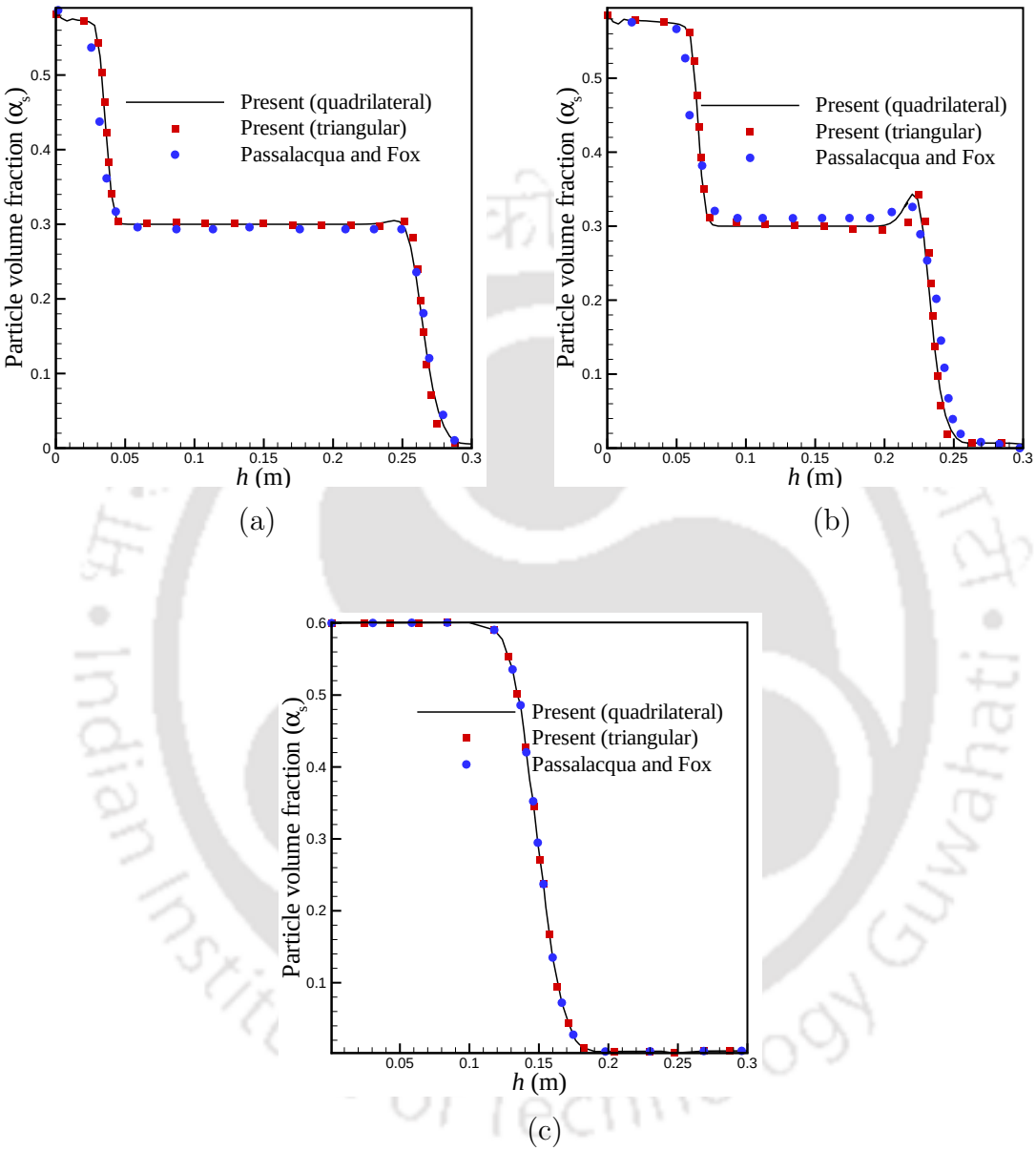

Figure 3.18: Comparison of axial particle phase volume fraction profile along the centerline at (a) t=0.1 s, (b) t=0.15 s, (c) t=0.6 s with [103].

predicted by the present solver (with both orthogonal and non-orthogonal grids) at different time instances match well with the results shown in [103]. Hence, it can be

said that the developed solver has the ability to accurately predict the rapid changes in particle phase volume fractions in the proximity of maximum packing limit.

Check for mass conservation

In order to assess the ability of the flow solver to conserve mass discretely, the variation of total mass with time is studied for the settling suspension problem discussed herein. Since the problem has no particles entering or leaving the flow domain, so the total mass of the particles in the domain should necessarily remain constant. Table 3.2 shows the comparison of total mass of particles obtained after 5 s (50,000 time steps) of physical time with the initial total mass on all the three grids used for the simulations. Also, Fig. 3.19 shows the variation of total mass with time upto 1.5 s of physical time. It can be seen from both Table 3.2 and Fig. 3.19 that the percentage error between the initial and the final mass of the particles lie in the range of 10^{-5} for all the three grids which conclusively demonstrates the discrete mass conservation of the developed flow solver.

Table 3.2: Variation of total mass of the particles with time

Type of cells	$M_{initial}$ (kg) (a)	M_{final} (kg) (after 5 s) (b)	% error (b-a)/a×100
quadrilateral	0.450000031	0.450000267	5.24×10^{-5}
triangular	0.450000031	0.450000279	5.51×10^{-5}
hybrid	0.450000031	0.450000287	5.68×10^{-5}

These three test cases discussed herein clearly show the proper implementation of three-way coupling with KTGF model to take care of particle-particle and particle-wall interactions and and the need to incorporate frictional stress model to handle dense gas-particulate flows.

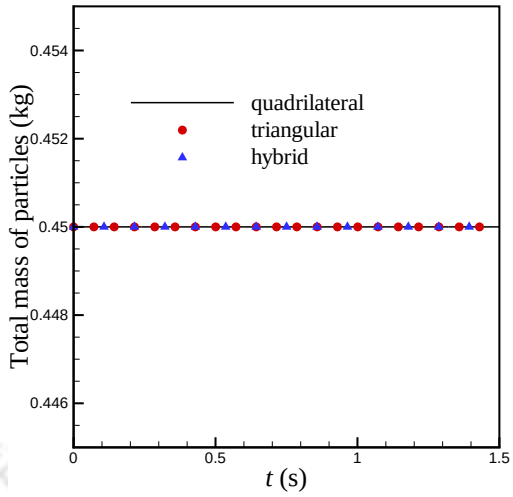

Figure 3.19: Variation of total mass of the particles with time for three different types of cells

3.4 Closure

In this chapter, a detailed validation of the developed gas-particulate flow solver has been presented. The solver has been developed indigenously and hence, significant efforts have been made to validate the flow solver at each stage in a careful manner. Studies have been performed for assessing the capability of the flow solver to handle all flow conditions (ranging from dilute to dense) with large density particles. The need for using the frictional stress model for dense gas-particulate flows is demonstrated and it has been found from the validation studies that the flow solver can accurately compute dilute, dispersed and dense gas-particulate flows for a wide range of flow scenarios.

Chapter 4

Dispersed laminar gas-particle flows through vertical and horizontal channels

Particle diameter (Stokes number), particle density and inlet particle phase volume fraction are some parameters which greatly influence the flow physics of dispersed gas-particle flows. In this chapter, using the developed solver, an extensive study of dispersed gas-particle flows through vertical and horizontal channels considering two-way coupling between the phases is carried out in order to both qualitatively and quantitatively investigate the effects of these parameters on the overall hydrodynamics of this type of flows. Also a detailed study is carried out in order to find out the effects of 'inlet slip' (or difference of phase velocities at inlet) on the flow physics inside a horizontal channel. The effects of both gas inlet velocity being greater than particle inlet velocity and vice-versa have been studied keeping all other parameters constant. A detailed analysis of the influence of all these parameters on the flow physics of dispersed gas-particle flows are presented based on the obtained results.

The contents in this chapter have been published as Kotoky, S., Dalal, A., and Natarajan, G., 2018, "A parametric study of dispersed laminar gas-particle flows through vertical and horizontal channels", Advanced Powder Technology, vol. 29 (5), pp. 1072-1084.

4.1 Problem definition

In order to investigate the effects of particle diameter and inlet particle phase volume fraction on the hydrodynamics of dispersed laminar gas-particle flows, a vertical channel of height (H) 0.4 m and width (D) of 0.155 m is considered as shown in Fig. 4.1. Each of the phases is allowed to enter the channel with a velocity of 1

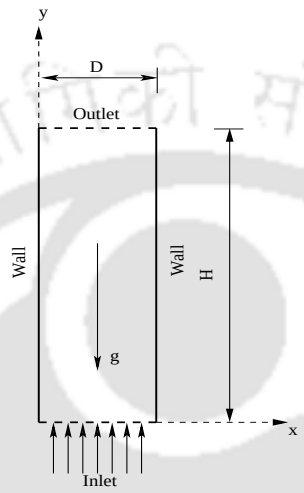

Figure 4.1: Schematic of the vertical channel used to study effects of particle diameter and inlet particle volume fraction.

m/s. Gravity is acting vertically downward opposite to the flow direction. The flow Reynolds number based on the channel width (D) is taken to be 200. The gas phase is considered to be air with density 1.2 kg/m^3. The simulations are carried out for two sets of particles having densities of 500 kg/m^3 and 1000 kg/m^3 respectively. In order to study the effects of particle diameter on the flow physics inside the channel, the simulations have been carried out for three values of particle diameters (d_s= 100 μm, 300 μm and 500 μm) for an inlet particle phase volume fraction equal to 0.01, for both the values of particle densities. On the other hand, simulations are carried out for three values of inlet particle phase volume fraction (α_s=0.0001, 0.001 and 0.01) for a particle diameter of 300 μm in order to study the effects of change of inlet particle phase volume fraction on the hydrodynamics. A two-way coupling is considered between the phases. A grid of 2480 uniform quadrilateral cells is used for the simulations. The drag model of Gidaspow [86] is used for the simulations. The simulation parameters are listed in Table 4.1.

Table 4.1: Parameters used for simulations of dispersed gas-particle flow through vertical channel

Simulation parameters	Values
Channel length (H)	0.4 m
Channel height (D)	0.155 m
Inlet gas velocity (v_g)	1.0 m/s
Inlet particle velocity (v_s)	1.0 m/s
Inlet Particle volume fraction (α_s)	0.0001, 0.001, 0.01
Gas density (ρ_g)	1.2 kg/m^3
Particle density (ρ_s)	500, 1000 kg/m^3
Particle diameter (d_s)	100, 300, 500 μm
Flow Reynolds number (Re)	200

4.2 Study of effects of particle diameter

In order to investigate the effects of particle diameter on the hydrodynamics of gas-particulate flows, three values of particle diameter 100 μm, 300 μm and 500 μm are considered for the simulations. The resulting effects of change of particle diameter on the steady phase velocity profiles are studied keeping all other simulation parameters constant.

4.2.1 Effects on steady state particle velocity profiles

Table 4.2 shows the values of maximum steady state velocities attained by the particle phase inside the channel for the two different values of particle densities of 500 kg/m^3 and 1000 kg/m^3 respectively and for the above mentioned values of particle diameters. A gradual decrease in the value of the maximum steady state particle velocity can be observed inside the channel with increase in particle size for both the values of densities. Furthermore, Fig. 4.2 shows the variation of steady state particle velocity profiles at the midplane (H=0.2 m) of the channel for a

Table 4.2: Maximum particle velocity inside the channel for particles of different sizes at constant inlet volume fraction of 0.01

Case	Particle density (kg/m^3)	Particle diameter (μm)	Max particle velocity (m/s)
1	500	100	1.14
		300	1.11
		500	1.06
2	1000	100	1.10
		300	1.05
		500	0.96

particle density of 1000 kg/m^3 for three sets of particle diameters. It is evident from

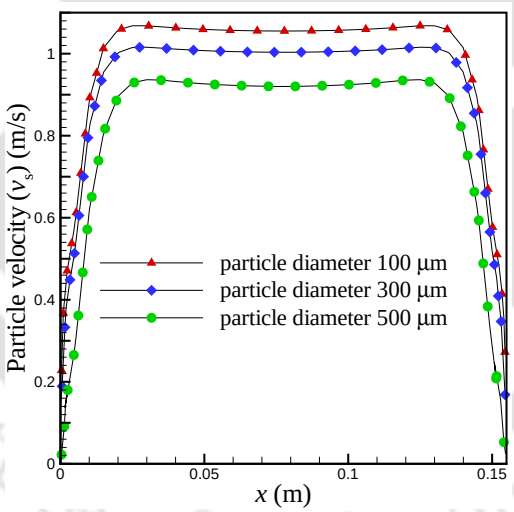

Figure 4.2: Variation of steady state particle velocity profiles at midplane of the vertical channel with particle diameter for inlet particle volume fraction 0.01.

both Table 4.2 and Fig. 4.2 that as the particle diameter is increased from 100 μm to 500 μm, the maximum steady state particle velocity at a particular section of the channel decreases. This can be attributed to the fact that the motion of the particles with larger diameters (or larger Stokes numbers) is more influenced by their inertia

and gravitational forces than the inter-phase drag force acting between the phases. Due to this high inertia and gravitational force as compared to the interphase drag forces for higher diameter particles, the steady state particle velocity at a certain section of the channel decreases with increase in particle diameter for a particular inlet particle volume fraction.

4.2.2 Effects on steady state gas velocity profiles

The effects of change of particle diameter on the corresponding steady state gas velocity profiles are also studied. The maximum steady state gas velocities obtained for the above case are shown in Table 4.3. It can be seen in Table 4.3 that unlike particle velocity, the maximum steady state gas velocity obtained inside the domain tend to increase marginally with increase in particle diameter. Also, the variations

Table 4.3: Maximum gas velocity inside the channel for particles of different sizes at constant inlet volume fraction

Case	Particle density (kg/m^3)	Particle diameter (μm)	Max gas velocity (m/s)
1	500	100	1.144
		300	1.149
		500	1.155
2	1000	100	1.11
		300	1.117
		500	1.129

of steady state gas velocity profiles at the midplane (H=0.2 m) of the channel for a particle density of 1000 kg/m^3 are shown for two sets of particle diameters of 100 μm and 500 μm in Fig. 4.3. It can be seen both in both Table 4.3 and Fig. 4.3 that as the particle diameter is increased keeping all other parameters constant, the gas velocity at a certain particle phase density shows a gradual marginal increase with particle diameter. It is due to the fact that particle velocity inside the domain decreases with increase in particle diameter, so for higher diameter particles,

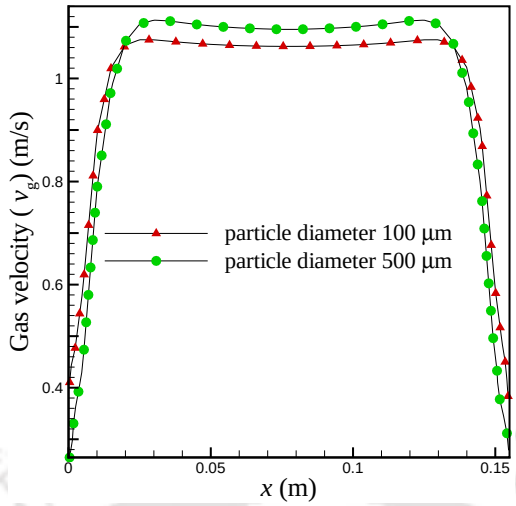

Figure 4.3: Variation of steady state gas velocity profiles at midplane of the vertical channel with particle diameter at constant inlet particle volume fraction

the opposing drag force exerted by the particles on the gas phase decreases which in turn increases the corresponding gas velocity with increase in particle diameter inside the channel.

Figs. 4.4 (a) and (b) show the contours of steady state gas and particle velocity respectively in the channel for particle density of 1000 kg/m^3 and particle diameter of 500 μm.

4.3 Study of effects of inlet particle phase volume fraction

In order to study the effects of inlet particle phase volume fraction on the steady state phase velocity profiles inside a vertical channel, the same channel (shown in Fig. 4.1) is considered with the flow parameters discussed in Section 4.1. The volume fraction of the particles at the inlet of the channel is varied from a lower value of 0.0001 to a moderate value of 0.01 for particle densities of 500 kg/m^3 and 1000 kg/m^3 and particle diameter of 300 μm. The resulting effects of change of inlet particle phase volume fraction on the steady phase velocity profiles are studied keeping all other simulation parameters constant.

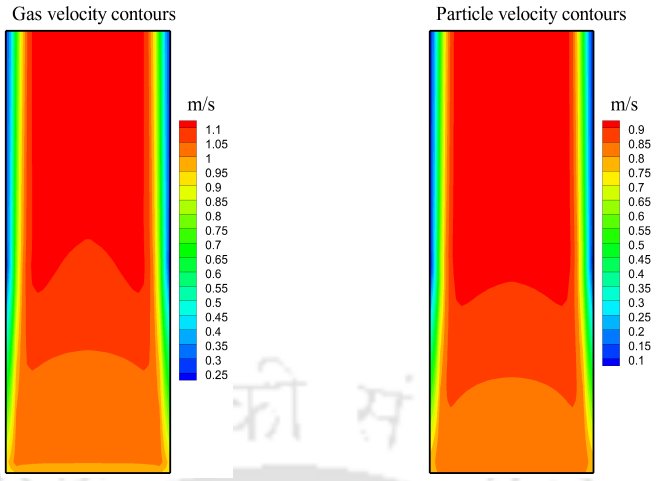

(a) (b)

Figure 4.4: Contours of steady state (a) gas phase velocity and (b) particle phase velocity for particle density of 1000 kg/m^3 and diameter of 500 μm for inlet particle phase volume fraction 0.01

4.3.1 Effects on steady state gas velocity profiles

The steady state gas phase velocity profiles at the midplane of the channel (H=0.2 m) for density value of 500 kg/m^3 are plotted in Fig. 4.5. It can be seen that as particle phase volume fraction is increased from 0.0001 to 0.01, the steady state velocity attained by the gas phase at midplane of the channel decreases. This can be attributed to the fact that with increase in particle phase volume fraction, the amount of drag acting on the gas phase increases as the interphase exchange term (K_{gs}) has particle volume fraction (α_s) in the numerator. This in turn reduces the steady state maximum velocity of the gas phase at any section of the channel. It is also noticeable that with increase is particle volume fraction, the gas phase velocity profile changes its shape from a nearly parabolic one (for inlet particle volume fraction 0.0001) to a bit flattened one (for inlet particle volume fraction 0.01). Table 4.4 shows the values of maximum gas velocity obtained in the domain at steady state for the above mentioned density and particle diameter values and for particle phase volume fraction varying from 0.0001 to 0.01. The gradual decrease in the value of maximum gas phase velocity inside the domain seen in Table 4.4 is due to the increase of the magnitude of interphase drag force exerted by the particle phase on the gas phase with increase in particle phase volume fraction.

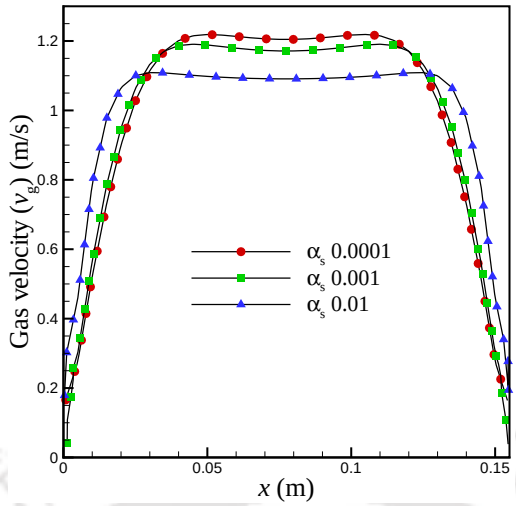

Figure 4.5: Variation of steady state gas velocity profiles at midplane of the vertical channel with inlet particle volume fraction for particle diameter 300 μm

Table 4.4: Maximum gas velocity inside the channel for different inlet volume fractions of particle phase at constant particle diameter of 300 μm

Case	Particle density (kg/m^3)	Particle volume fraction (inlet)	Max gas velocity (m/s)
1	500	0.0001	1.31
		0.001	1.26
		0.01	1.15
2	1000	0.0001	1.29
		0.001	1.23
		0.01	1.12

4.3.2 Effects on steady state particle velocity profiles

Like gas phase velocity, noticeable variations can also be observed in case of steady state particle velocity with change in inlet particle phase volume fraction. Figure 4.6 shows the profiles of steady state particle velocity at the midplane (H=0.2 m) of the channel. In Fig. 4.6, a gradual decrease of steady state particle velocity can

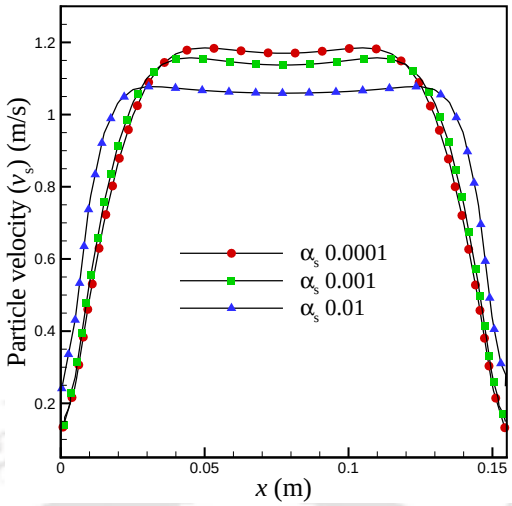

Figure 4.6: Variation of steady state particle velocity profiles at midplane of the vertical channel with inlet particle volume fraction for particle diameter 300 μm

be observed with increase in particle phase volume fraction. Also, the maximum values of particle phase velocity obtained inside the channel for different inlet volume fractions have been shown in Table 4.5. It can be seen from both Fig. 4.6 and

Table 4.5: Maximum particle velocity inside the channel for different inlet volume fractions of particle phase at constant particle diameter of 300 μm

Case	Particle density (kg/m^3)	Particle volume fraction (inlet)	Max particle velocity (m/s)
1	500	0.0001	1.28
		0.001	1.23
		0.01	1.11
2	1000	0.0001	1.24
		0.001	1.12
		0.01	1.05

Table 4.5 that like gas velocity, steady state particle velocity inside the channel also decreases with increase in the particle phase volume fraction at inlet. It is again

due to the increase in the value of interphase momentum exchange coefficient (K_{gs}) with increase in the value of particle phase volume fraction which in turn increases the interphase drag exerted by the gas phase on the particles.

4.4 Study of effect of inlet slip between the phases

The term 'inlet slip' refers to the difference of the phase velocities at the inlet of the domain. Depending on the way in which particles are introduced into the domain, There may be a difference of velocity of the phases at the inlet in different real situations like pneumatic conveying, solid transportation system etc. Hence, this study has been taken up in the present work and the variations of phase velocities and volume fractions in the domain have been studied with inlet slip for a particular value of inlet particle phase volume fractions.

Problem definition

In this study, a two-dimensional horizontal channel of length L=0.4 m and height H=0.155 m as shown in Fig. 4.7 is considered. The fluid phase is considered to

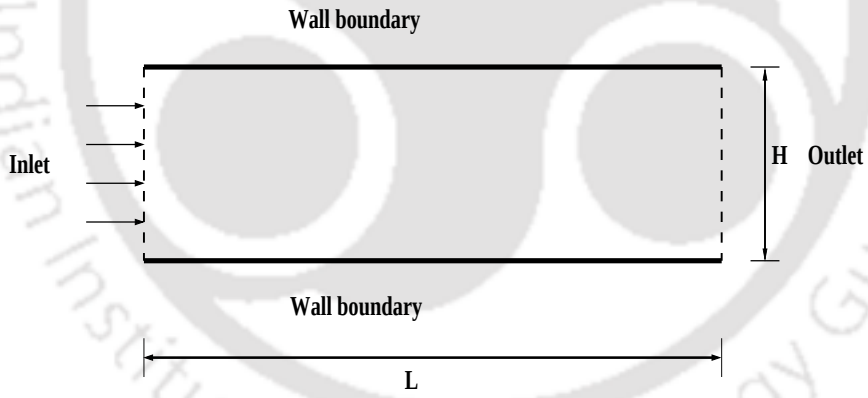

Figure 4.7: Schematic of horizontal channel used to study the effects of inlet slip between the phases.

be air with density 1.2 kg/m^3 and the particulate phase density is taken to be 500 kg/m^3. The inlet volume fractions of gas and particle phase are specified as 0.8 and 0.2 respectively. A no slip condition is specified for the carrier phase velocity at the walls, while a free-slip condition is specified for the disperse phase velocity. Two-way coupling is achieved between the phases by assuming that there is no momentum

loss due to the collisions of the particles with the wall and particle-particle collisions are perfectly elastic. The particle diameter is considered to be equal to 300 μm. The slip is provided between the phases in two ways.

- Gas velocity (u_g)=1.0 m/s and particle velocity (u_s)=0.5 m/s.
- Gas velocity (u_g)=0.5 m/s and particle velocity (u_s)=1.0 m/s.

In both the cases, the flow Reynolds number based on the channel height and inlet gas velocity is kept to be equal to 200. A uniform grid of 2480 quadrilateral cells is used for the simulations. The changes in the steady state phase velocity and volume fraction profiles as well as the mass flow rates of both phases are studied and compared with the case when both the phases enter with the same magnitude of velocity.

4.4.1 When gas velocity is greater than particle velocity at inlet ($u_g > u_s$)

Figure 4.8 (a) shows the comparison of steady state gas velocity profiles when (i) both the phases enter the channel with same velocity (u_g=u_s=1 m/s, no inlet slip condition) and when (ii) particle velocity at inlet is less than the gas velocity ($u_g > u_s$, u_g=1 m/s and u_s=0.5 m/s) at the midplane (H=0.2 m) of the channel. It can be seen that although the inlet gas velocity for cases (i) and (ii) mentioned here are the same, yet the steady state gas velocity obtained at the midplane of the channel is less in case (ii) than that of case (i). It is due to the reason that in case (ii), as the inlet particle velocity is less than the inlet gas velocity, there exists a tendency of the gas phase to increase the particle phase velocity and hence there is more momentum transfer from the gas phase to particle phase in this case than in the case of same inlet velocities. As a result, the steady state gas velocity at any section for this case is less than the case where there is same inlet velocity for both the phases. Table 4.6 shows the steady state mass flow rates at different sections of the channel and it can be seen that the steady state mass flow rate for the gas phase remains the same in both the cases (i) and (ii). But as the steady state gas phase velocity at any section in case (ii) is lower than that of case (i), so the gas phase volume fraction has to increase in order to keep the mass flow rate same in both the cases. Hence, it can be seen in Fig. 4.8 (b) that the steady state gas phase volume fraction at the

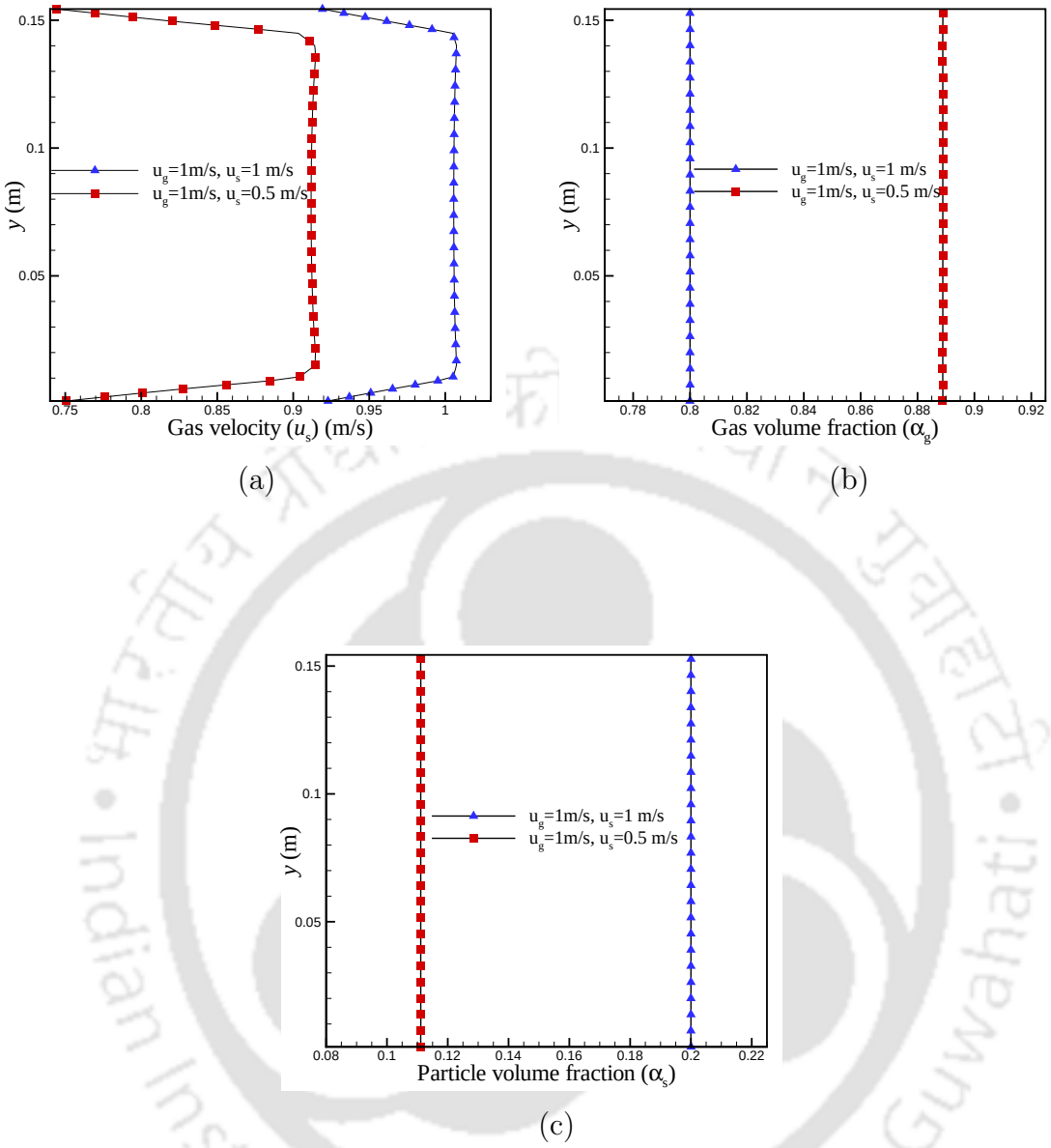

Figure 4.8: Comparison of plots of steady state (a) gas velocity,(b) gas volume fraction and (c) particle volume fraction profiles in the midplane of the channel for (i) u_g=u_s=1 m/s; (ii) u_g=1 m/s, u_s=0.5 m/s

midplane of the channel is greater in case (ii) than in case (i). Since at any section of the channel, $\alpha_g + \alpha_s$=1, so, the corresponding steady state particle phase volume fraction decreases for case (ii) than in case (i); as seen in Fig. 4.8 (c).

Table 4.6: Steady state mass flow rates at different channel sections for $u_g > u_s$ at inlet

Case	inlet		x=0.1 m		x=0.2 m	
	$\dot{m}_g$ (kg/s)	$\dot{m}_s$ (kg/s)	$\dot{m}_g$ (kg/s)	$\dot{m}_s$ (kg/s)	$\dot{m}_g$ (kg/s)	$\dot{m}_s$ (kg/s)
(i) $u_g = u_s$=1 m/s	0.00124	0.155	0.001238	0.15491	0.001239	0.15484
(ii) u_g=1 m/s, u_s=0.5 m/s	0.00124	0.0775	0.001236	0.07701	0.001234	0.07699

4.4.2 When particle velocity is greater than gas velocity at inlet $u_s > u_g$)

In this case, the carrier phase, i.e., the gas phase inlet velocity is less than the dispersed phase inlet velocity. In this case also, a distinct difference between the steady state particle velocity profiles can be observed for the cases when (i) both the phases enter the channel with same velocity (u_g=u_s=1 m/s, no inlet slip condition) and when (ii) particle velocity at inlet is greater than the gas velocity (u_g=0.5 m/s and u_s=1 m/s), as seen in Fig. 4.9 (a). It can be seen that although the inlet particle velocity for cases (i) and (ii) mentioned above are same, yet the steady state particle velocity obtained at the midplane of the channel is less in case (ii) than that of case (i). It is due to the fact that in case (ii), as the inlet particle velocity is more than the inlet gas velocity, there exists a tendency of the gas phase to decrease the particle phase velocity through the interphase drag force term which contains ($\mathbf{u}_g$-$\mathbf{u}_s$) term. As a result, the steady state particle velocity at any section for this case is less than the case where there is same inlet velocity for both the phases. Table 4.7 shows the steady state mass flow rates at different sections of the channel and it can be seen that the steady state mass flow rate for the particle phase remains the same in both the cases (i) and (ii). But as the steady state particle phase velocity at any section in case (ii) is lower than in case (i), so the particle phase volume fraction has to increase in order to keep the mass flow rate constant in both the cases. Hence, it can be seen in Fig. 4.9 (b) that the steady state particle phase volume fraction at the midplane of the channel is greater in case (ii) than in case (i). Since at any section

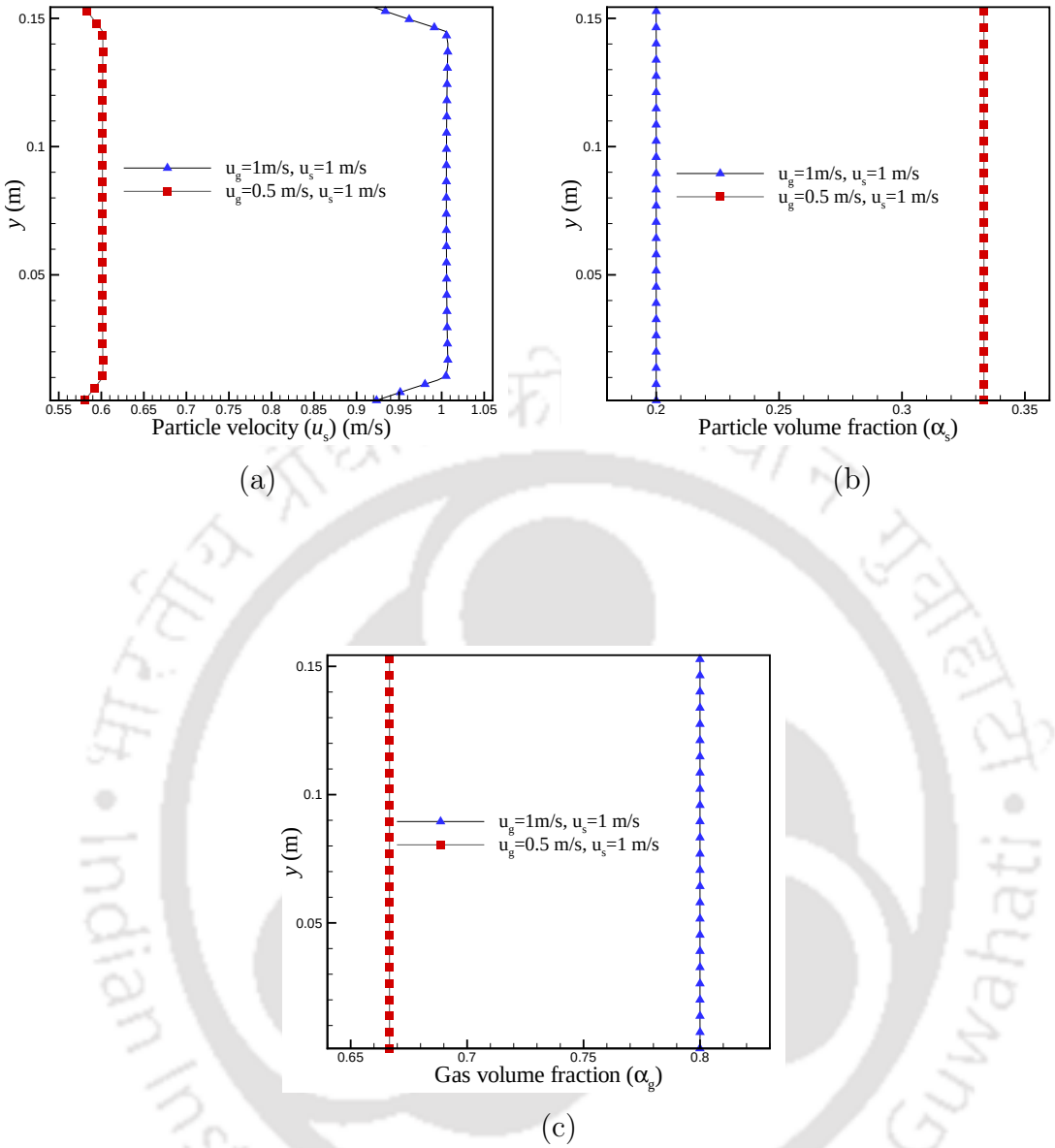

Figure 4.9: Comparison of plots of steady state (a) particle velocity, (b) particle volume fraction and (c) gas volume fraction profiles in the midplane of the channel for (i) u_g=u_s=1 m/s; (ii) u_g=0.5 m/s, u_s=1 m/s

of the channel, $\alpha_g + \alpha_s$=1, so, the corresponding steady state gas phase volume fraction decreases for case (ii) than in case (i); as seen in Fig. 4.9 (c).

Table 4.7: Steady state mass flow rates at different channel sections for $u_s > u_g$ at inlet

Case	inlet		x=0.1 m		x=0.2 m	
	$\dot{m}_g$ (kg/s)	$\dot{m}_s$ (kg/s)	$\dot{m}_g$ (kg/s)	$\dot{m}_s$ (kg/s)	$\dot{m}_g$ (kg/s)	$\dot{m}_s$ (kg/s)
(i) $u_g = u_s$=1 m/s	0.00124	0.155	0.001238	0.15491	0.001239	0.15484
(ii) u_g=0.5 m/s, u_s=1 m/s	0.00062	0.155	0.000619	0.15483	0.000616	0.15480

4.5 Closure

In this chapter, a detailed parametric study of dispersed laminar gas-particle flows assuming a two-way coupling between the phases has been carried out using the flow solver. The variations in the steady state phase velocities and phase volume fraction profiles have been studied quantitatively for variations in particle diameter as well as inlet particle phase volume fractions in case of dispersed gas-particle flows through a vertical channel. Studies have also been carried out in order to find out the effects of 'inlet-slip' on the steady state phase velocity and volume fraction profiles in case of horizontal channels. Distinguishable variations in steady state phase velocities and volume fraction profiles have been observed in both the cases.

Chapter 5

Effects of specularity and restitution coefficients on the hydrodynamic behavior of flows through horizontal channels

Particle-wall interactions (quantified by specularity coefficient, ϕ) and particle-particle interactions (quantified by restitution coefficient, e) have significant influence on the overall flow characteristics of dispersed gas-particle flows. In this chapter, using the developed solver, a study has been carried out to investigate the effects of ϕ and e on the overall hydrodynamics of dispersed gas-particle flows through horizontal channels. Also, investigations have been carried out to find out the ϕ-e pair for which the phase velocities become an extremum. In addition to these, The variation in the wall shear stress of both the phases with change in the value of ϕ has also been studied. It has been observed in literature that very few studies are available till date where the quantitative effects of variations of these two parameters have been studied individually (as done by Loha et al. [73, 74] for bubbling gas-solid fluidized

The contents in this chapter have been published as Kotoky, S., Dalal, A., and Natarajan, G., 2018, "Effects of specularity and particle-particle restitution coefficients on the hydrodynamic behavior of dispersed gas-particle flows through horizontal channels", Advanced Powder Technology, vol. 29(4), pp. 874-889.

beds) as well as in combination for dispersed gas-particle flows through horizontal channels. Moreover, discussions on the consequent effects of variation of these two parameters on the steady state phase velocities, volume fractions as well as on the wall shear stress profiles are also very limited. With these motivations in mind, in this chapter, a detailed parametric study has been carried out to investigate the effects of variation of ϕ and e on the phase velocitites and volume fraction profiles inside a horizontal channel. In addition to these, the variation in the wall shear stress of both the phases with the variation of ϕ has also been studied.

5.1 Problem definition

The present investigations focus on a thorough parametric study of dispersed gas-particle flows through horizontal channels considering a three-way coupling between the phases in order to determine the effects of specularity coefficient (ϕ) and particle-particle restitution coefficient (e) on the flow physics inside the channel. To this end, simulations are carried out in a horizontal channel of length L=0.4 m and width W= 0.155 m as shown in Fig. 5.1. The gas phase is considered to be air with a density

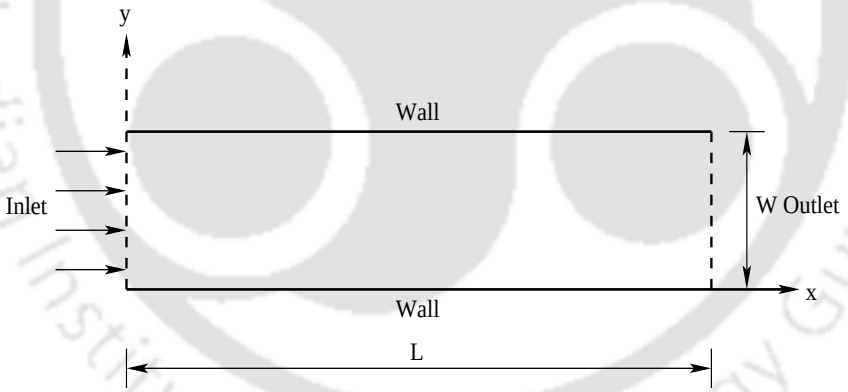

Figure 5.1: Schematic of horizontal channel used to study the effects of specularity coefficient and particle-particle restitution coefficient.

of 1.2 kg/m^3 whereas the particle phase is considered to have a density of 2500 kg/m^3 and the particle diameter is considered to be 530 μm. This value of particle density and particle diameter corresponds to Geldart B [16] group of particles. The flow Reynolds number based on the channel width is considered to be equal to 200. In order to investigate the effects of ϕ on the flow behavior, simulations have been

carried out for three values of ϕ (ϕ=0.0, 0.5 and 0.8) for an inlet particle volume fraction value of 0.1 and at a fixed value of e=0.9. Similarly, the effects of e have been studied by varying its value from 0.99 to a value of 0.8 for an inlet particle volume fraction of 0.1 and at a value of ϕ=0.5. These values for ϕ and e have been selected for simulations because the previously reported works involving simulation of Geldart B particles like [73, 74] have used the values of ϕ and e in this range and obtained comparable results with available experimental data for bubbling gas-solid fluidized beds. Also, a study is performed for different combinations of values of ϕ and e in order to find the combined effect of the two parameters on the overall hydrodynamics of gas-particle flows through a horizontal channel. Finally, a study on the variation of wall shear stress of both the phases with wall-roughness has been taken up. In this regard, simulations have been carried out for the above mentioned three values of ϕ at a value of e=0.99 and a detailed analysis of the obtained results have been carried out thereafter. The simulation parameters are listed in Table 5.1.

Table 5.1: Parameters used for simulation for dispersed gas-particle flow through horizontal channel

Simulation parameters	Values
Inlet gas velocity (u_g)	1.0 m/s
Inlet particle velocity (u_s)	1.0 m/s
Inlet Particle volume fraction (α_s)	0.1
Gas density (ρ_g)	1.2 kg/m^3
Particle density (ρ_s)	2500 kg/m^3
Particle diameter (d_s)	530 μm
Flow Reynolds number (Re)	200
Specularity coefficient (ϕ)	0, 0.5, 0.8
Particle restitution coefficent (e)	0.99, 0.9, 0.8

5.2 Grid independence study

Several researchers like Gelderbloom et al. [104], Jung et al. [105] have done studies to find out the appropriate grid size for bubbling fluidized beds involving gas-particle flows. Gelderbloom et al. [104] concluded that when the grid size is of the order of ten times the particle diameter, the bubble size computed with that grid showed closer agreement with experimental results. So, in the present study, grid independence study has been carried out to investigate if this observation holds good for the test case studied herein. In this regard, three grids with different number of volumes have been used; the first one is of size 60 × 21 (where the cell size is more than ten times of particle diameter), the second one is of size 80 × 31 (where the cell size is of the order of ten times of particle diameter) and third one is of size 120 × 51 (where the cell size is much smaller than ten times of particle diameter). Considering e=0.9 and ϕ=0.5, simulations are carried out using the three meshes and the steady state particle velocity and particle volume fraction profile at the midplane of the channel are compared for the three grids in Fig. 5.2. It can be

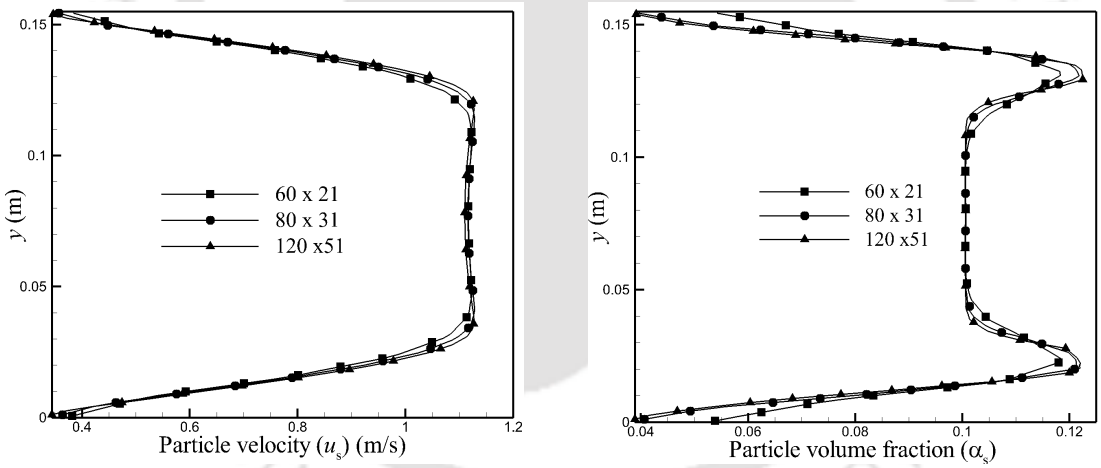

Figure 5.2: Plots of steady state (a) particle velocity, (b) particle phase volume fraction profiles at midplane of the channel for different grid sizes.

seen that there is no significant difference among the particle velocity profiles obtained using the three different grids and that the profile obtained from the 80 × 31 grid lies in between the profiles obtained from 60 × 21 and 120 × 51 grids for particle velocity. In case of particle phase volume fraction, the 60 × 21 grid seems

to overpredict near the walls, while there is no significant difference in the steady state particle phase volume fraction profiles for the other two grids. Figures 5.2(a) and (b) clearly show that the difference in the particle phase velocity and volume fraction profiles obtained from the 80 × 31 grid with that obtained from 120 × 51 grid is very less and hence, without sacrificing significant amount of accuracy, The simulations performed in this study are performed using a grid of size 80 × 31.

5.3 Effects of variation of specularity coefficient

In order to study the effect of specularity coefficient (ϕ) on the flow characteristics of dispersed laminar gas-particle flows, simulations are carried out in the channel shown in Fig. 5.1 based on the parameters mentioned in Table 5.1. For an inlet particle phase volume fraction of 0.1, the value of ϕ is varied from zero (for free-slip wall boundary condition) to a value equal to 0.8 (which means that 80% of particle momentum is lost due to collision with the wall) for a particular value of e=0.9 (corresponding to 10% loss of particle momentum due to particle-particle collisions). The variations of gas and particle velocities as well as particle volume fraction profiles with variation of ϕ have been studied for that particular value of e.

5.3.1 Effect on particle velocity profiles

The particle velocity profiles at the midplane of the channel (x=0.2 m) for an inlet particle phase volume fraction of 0.1 are plotted for ϕ=0, 0.5 and 0.8 at a particular value of e=0.9; as shown in Fig. 5.3. It is observed that particle velocity near the wall is maximum for ϕ=0 as in this case, there is no loss of particle momentum due to particle-wall collisions. With increase in the value of ϕ, the particle velocity near the wall gets decreased. As the steady state particle velocity near the wall at any section of the channel decreases with increase in the value of ϕ, so to compensate this loss in velocity and to make the net steady state mass flow rate remain constant at a particular section, the value of particle velocity increases near the centerline of the channel where there is little wall effect. In Fig. 5.3, it can be well understood that the maximum value of the steady state particle velocity is obtained for ϕ=0.8 at a particular value of e. It can also be observed from Table 5.2 that the maximum particle velocity in the domain is obtained when the value of ϕ is maximum and

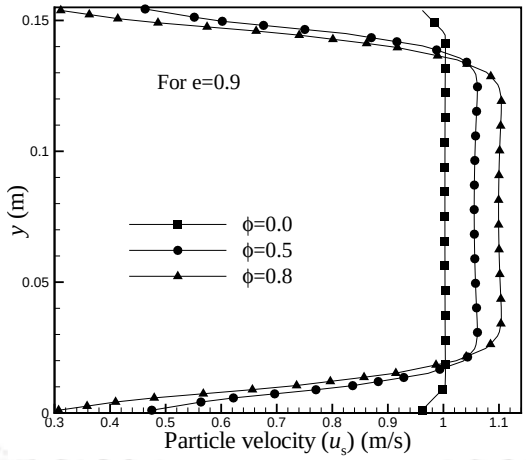

Figure 5.3: Variation of steady state particle velocity profiles with ϕ at the midplane of the channel for e=0.9.

the minimum particle velocity in the domain is obtained when the value of ϕ is minimum, at a particular value of e.

5.3.2 Effect on gas velocity profiles

The corresponding gas phase velocity profiles at the midplane of the channel (x=0.2 m) for the same value of inlet particle volume fraction of 0.1 are plotted for ϕ=0, 0.5 and 0.8 at a particular value of e=0.9; as shown in Fig. 5.4. For a particular value of e, the gas velocity near the wall is maximum when ϕ=0 and it decreases as the value of ϕ is increased. It is due to the reason that particle velocity is maximum near the wall for ϕ=0 and since the interphase drag force term contains $(\mathbf{u}_s - \mathbf{u}_g)$ term, so the tendency of the particle phase to increase the velocity of the gas phase near the wall is also maximum when ϕ=0. Due to this, gas velocity near the wall at any section of the channel is maximum for ϕ=0 and it decreases with increase in ϕ. As the steady state gas velocity near the wall at any section of the channel decreases with increase in the value of ϕ, hence to keep the steady state net mass flow rate at a particular section of the channel constant, the gas velocity near the centerline of the channel also increases like particle velocity, with increase in the value of ϕ. In Fig. 5.4 and Table 5.2, it can be seen that at a particular value of e, the maximum gas velocity in the domain can be obtained when the value of ϕ is maximum.

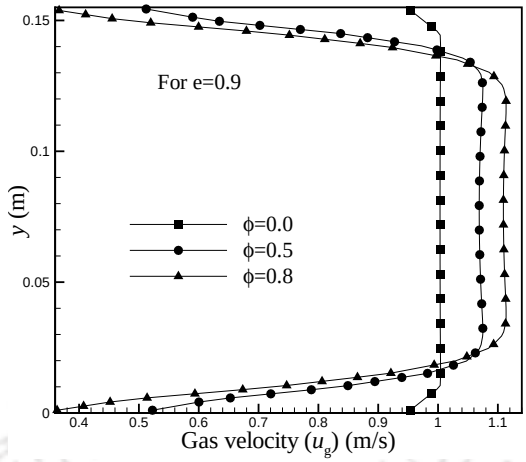

Figure 5.4: Variation of steady state gas velocity profiles with ϕ at the midplane of the channel for e=0.9.

Table 5.2: Maximum gas and particle velocity inside the channel for different values of ϕ at a particular value of e

Case	e	ϕ	Max gas velocity (m/s)	Max particle velocity (m/s)
1	0.9	0.0	1.00754	1.00691
		0.5	1.12	1.112
		0.8	1.16	1.136

5.3.3 Effect on particle phase volume fraction profiles

The steady state particle phase volume fraction profiles at the midplane of the channel (x=0.2 m) have been plotted in Fig. 5.5 for three values of ϕ=0, 0.5 and 0.8 and at a particular value of e=0.9. For ϕ=0 (free-slip condition), there is no loss of particle velocity due to collisions with the wall or in other words, the particles can move freely along the wall. As a result, the particles have a higher value of volume fraction near the wall for ϕ=0. But as the value of ϕ is increased, the resistance to the free motion of the particles along the wall also increases. So, it can be seen in Fig. 5.5 that at a particular value of e, the value of particle phase volume fraction

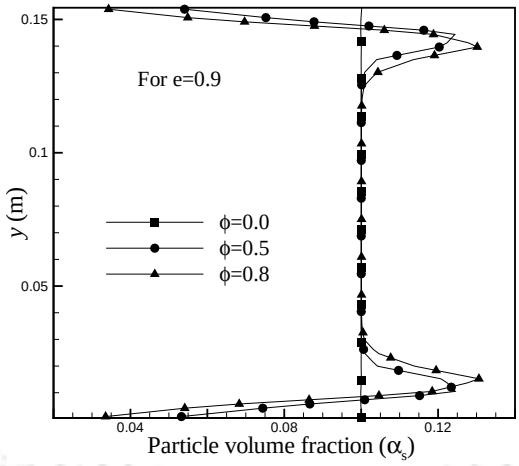

Figure 5.5: Variation of steady state particle volume fraction profiles with ϕ at the midplane of the channel for e=0.9.

near the wall decreases when the value of ϕ increases. The particles which move away from the wall tend to accumulate at some distance away from the wall where wall effect is not influential and hence, it can be seen that for non-zero values of ϕ, the particle volume fractions tend to increase as we move away from the wall and becomes maximum at a certain distance from the wall. The maximum value of particle volume fraction at the midplane of the channel is found to be obtained for ϕ=0.8; at a particular value of e. At the central or core region of the channel which is far away from the wall, steady state volume fractions for all the three values of ϕ are almost same and equal to the inlet value of particle volume fraction.

5.4 Effects of variation of particle-particle restitution coefficient

The value of particle-particle restitution coefficient (e) is a measure of the amount of momentum lost due to collisions among the particles. A value of unity means that no momentum is lost whereas, for eg., a value of e=0.8 denotes that 20% of particle momentum is lost due to collisions. Now, in order to study the effects of variations of e on the flow physics inside the channel, the same horizontal channel described in Section 5.1 has been considered. Both the phases are considered to be entering the channel with same velocity of 1 m/s with inlet particle phase volume fraction of

0.1. The particle phase density is considered to be equal to 2500 kg/m^3 whereas the gas phase is considered to be air with a density of 1.2 kg/m^3. The effects of e on the flow physics have been studied for three different values (e=0.99, 0.9 and 0.8) at a particular value of ϕ=0.5. The particle diameter is taken to be 530 μm.

5.4.1 Effect on particle velocity profiles

The variation in the steady state particle phase velocity profiles at the midplane of the channel (x=0.2 m) with e are shown in Fig. 5.6 for a value of ϕ=0.5. As the

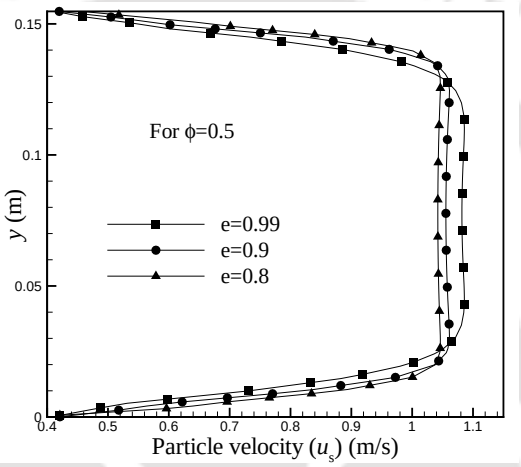

Figure 5.6: Variation of steady state particle velocity profiles with e at the midplane of the channel for ϕ=0.5.

value of ϕ is fixed, so there is negligible variation in the value of particle velocity at the wall for all the values of e. But, there exists a difference in particle velocities in the core region of the channel for different values of e. For e=0.99, the loss of momentum due to particle-particle collisions is minimum. As a result, maximum value of steady state particle velocity can be obtained at any section of the channel for e=0.99. For e=0.8, the loss of momentum due to particle-particle collisions is maximum out of the three values of e and so, steady state particle velocity at any section of the channel is minimum for e=0.8. Hence, with increase of values of e, particle velocity inside the domain increases. Table 5.3 shows that the particle velocity obtained inside the channel is maximum when the value of e is maximum, at a particular value of ϕ.

5.4.2 Effect on gas velocity profiles

The corresponding steady state gas phase velocity profiles at the midplane of the channel (x=0.2 m) obtained for the three values of e at a particular value of ϕ=0.5 are shown in Fig. 5.7. Also, the values of maximum gas velocities obtained inside the domain are shown in Table 5.3. It can be observed that at a particular value

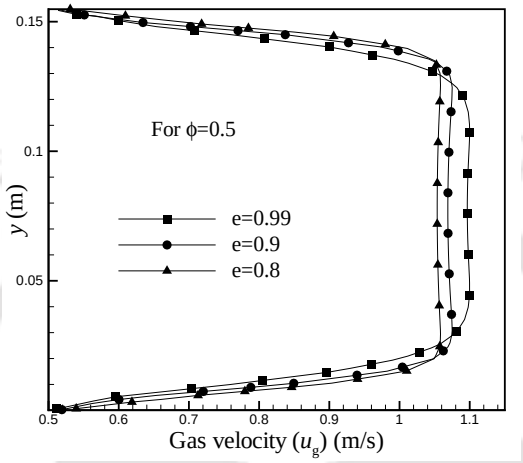

Figure 5.7: Variation of steady state gas velocity profiles with e at the midplane of the channel for ϕ=0.5.

of ϕ, as there is no variation in the particle velocity at the wall, so the drag force acting on the gas phase near the wall for all the values of e is same and hence, the steady state gas velocity near the wall is almost same for all the values of e. As

Table 5.3: Maximum gas and particle velocity inside the channel for different values of e at a particular value of ϕ

Case	ϕ	e	Max gas velocity (m/s)	Max particle velocity (m/s)
1	0.5	0.99	1.16	1.148
		0.9	1.12	1.112
		0.8	1.105	1.09761

discussed in Section 5.4.1, particle velocity u_s is maximum for e=0.99 and so the tendency to increase the gas phase velocity also becomes maximum when e=0.99. As a result, maximum gas velocity inside the channel is obtained for e=0.99 and it decreases with decrease in the value of e. It can be seen from Table 5.3 that at a particular value of ϕ, the gas velocity obtained inside the domain is maximum when the value of e is maximum and it is minimum when the value of e is minimum.

5.4.3 Effect on particle phase volume fraction profiles

The steady state particle phase volume fraction profiles for different values of e at the midplane of the channel (x=0.2 m) have been plotted in Fig. 5.8 for ϕ=0.5. As discussed in Section 5.3.3, at a particular non-zero value of ϕ, the particle volume fraction tends to increase as we move away from the wall to a local maximum value for all the values of e and forms a peak as seen in Fig. 5.8. But this local maximum

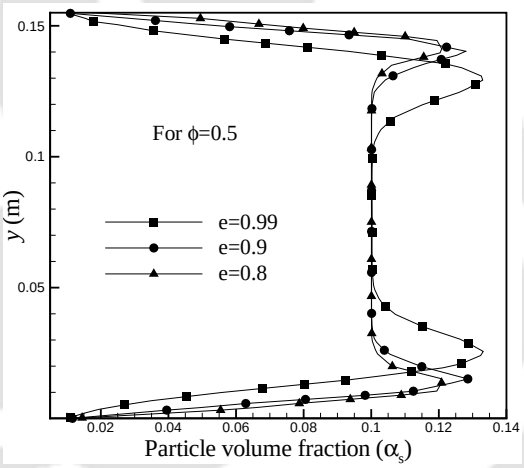

Figure 5.8: Variation of steady state particle volume fraction profiles with e at the midplane of the channel for ϕ=0.5.

value of particle volume fraction is found to increase with increase in the value of e. The reason behind this increase is that as the value of e is increased, the particle velocity increases due to less loss of particle momentum due to particle-particle collisions. In other words, the particles can move more freely and so, more and more particles which get deflected by the wall tend to accumulate in that section as the value of e is increased. Hence, the maximum peak value of steady state particle volume fraction has been obtained for e=0.99. In the central or core region of the

channel where wall effect is minimum, steady state volume fraction for all the three values of e are almost same and equal to the inlet value of particle volume fraction. A point worth noting is that the length of the region where steady state particle phase volume fraction is constant and equal to the inlet value is minimum when e=0.99 and it increases as the value of e decreases.

5.5 Comparison of results for different combinations of ϕ-e pairs

In Sections 5.3 and 5.4, studies have been carried out in order to investigate the effects of variations ϕ at a fixed e and e for fixed ϕ on the overall flow hydrodynamics of dispersed gas-particle flows through horizontal channels. So, in this section, a study is taken up in order to find combined effects of ϕ and e considering four different combinations listed below.

- ϕ=0 (minimum), e =0.99 (maximum).
- ϕ= 0.8 (maximum), e =0.99 (maximum).
- ϕ=0 (minimum), e =0.8 (minimum).
- ϕ=0.8 (maximum), e =0.8 (minimum).

5.5.1 Comparison of particle phase velocity profiles

The steady state particle phase velocity profiles are plotted at the midplane of the channel (x=0.2 m) for the above mentioned four cases and are shown in Figs. 5.9 (a), (b), (c) and (d). Distinct variations in the particle phase velocity profiles can be observed in all the plots. It can be seen from Figs. 5.9 (a) and (c) that when value of ϕ=0; there is no significant variation in the steady state particle velocity when the value of e is varied from 0.99 to 0.8. Hence, it can be said that for ϕ=0, variations in the values of e do not bring any significant variations in the steady state particle velocity. But, when the value of ϕ=0.8, it can be seen from Figs. 5.9 (b) and (d) that when value of e is maximum, the particle velocity in that case is also maximum. Again, for both e=0.99, 0.8; the particle velocity near the wall is

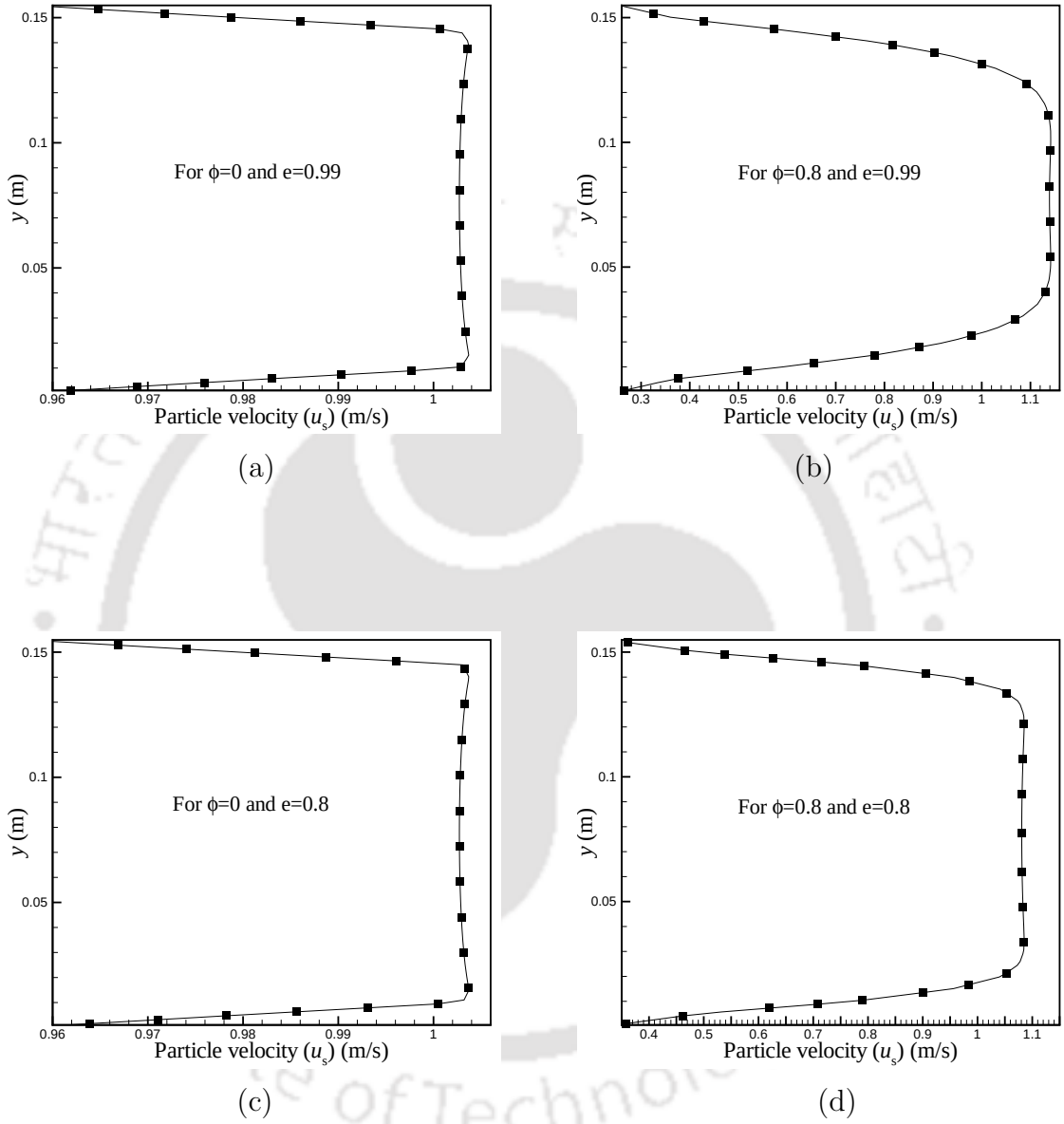

Figure 5.9: Comparison of plots of steady state particle velocity profiles for (a) ϕ=0, e=0.99; (b) ϕ=0.8, e=0.99; (c) ϕ=0, e=0.8 and (d) ϕ=0.8, e=0.8.

maximum for ϕ=0 and it is minimum for ϕ=0.8. But the velocity near the centerline of the channel is maximum for ϕ=0.8 for both the values of e. Table 5.4 shows the maximum values of particle velocity obtained inside the domain and it can be seen that out of the four combinations, the maximum value of particle velocity can be obtained for the combination ϕ=0.8, e=0.99, i.e., when both the values of ϕ and e are maximum.

5.5.2 Comparison of gas phase velocity profiles

The corresponding steady state gas phase velocity profiles are plotted at the mid-plane of the channel (x=0.2 m) for the four sets of ϕ-e pairs in Figs. 5.10 (a), (b), (c) and (d). It can be seen from Figs. 5.10 (a) and (c) that like particle velocity, when the value of ϕ=0; there is no significant variation in the steady state gas velocity when the value of e is varied from 0.99 to 0.8. But, when the value of ϕ=0.8, it can be seen from Figs. 5.10 (b) and (d) that when value of e is maximum, the gas velocity in that case is also maximum. This is due to increase of the drag force exerted by the particles on the gas which is due to the increase in the value of particle velocity with increase in the value of e. Again, for both e=0.99, 0.8; the gas velocity near the wall is maximum for ϕ=0 and it is minimum for ϕ=0.8. But the velocity near the central region of the channel is maximum for ϕ=0.8 for both the values of e. Table 5.4 shows the maximum values of gas velocity obtained inside the domain and it can be seen that out of the four combinations, like particle velocity, the maximum value of gas velocity can be obtained for the combination ϕ=0.8, e=0.99.

Table 5.4: Maximum gas and particle velocity inside the channel for different extreme combinations of values of ϕ and e

Case	ϕ-e pairs	Max gas velocity (m/s)	Max particle velocity (m/s)
1	ϕ=0, e=0.99	1.00802	1.00688
2	ϕ=0.8, e=0.99	1.21	1.19
3	ϕ=0, e=0.8	1.00749	1.00683
4	ϕ=0.8, e=0.8	1.138	1.129

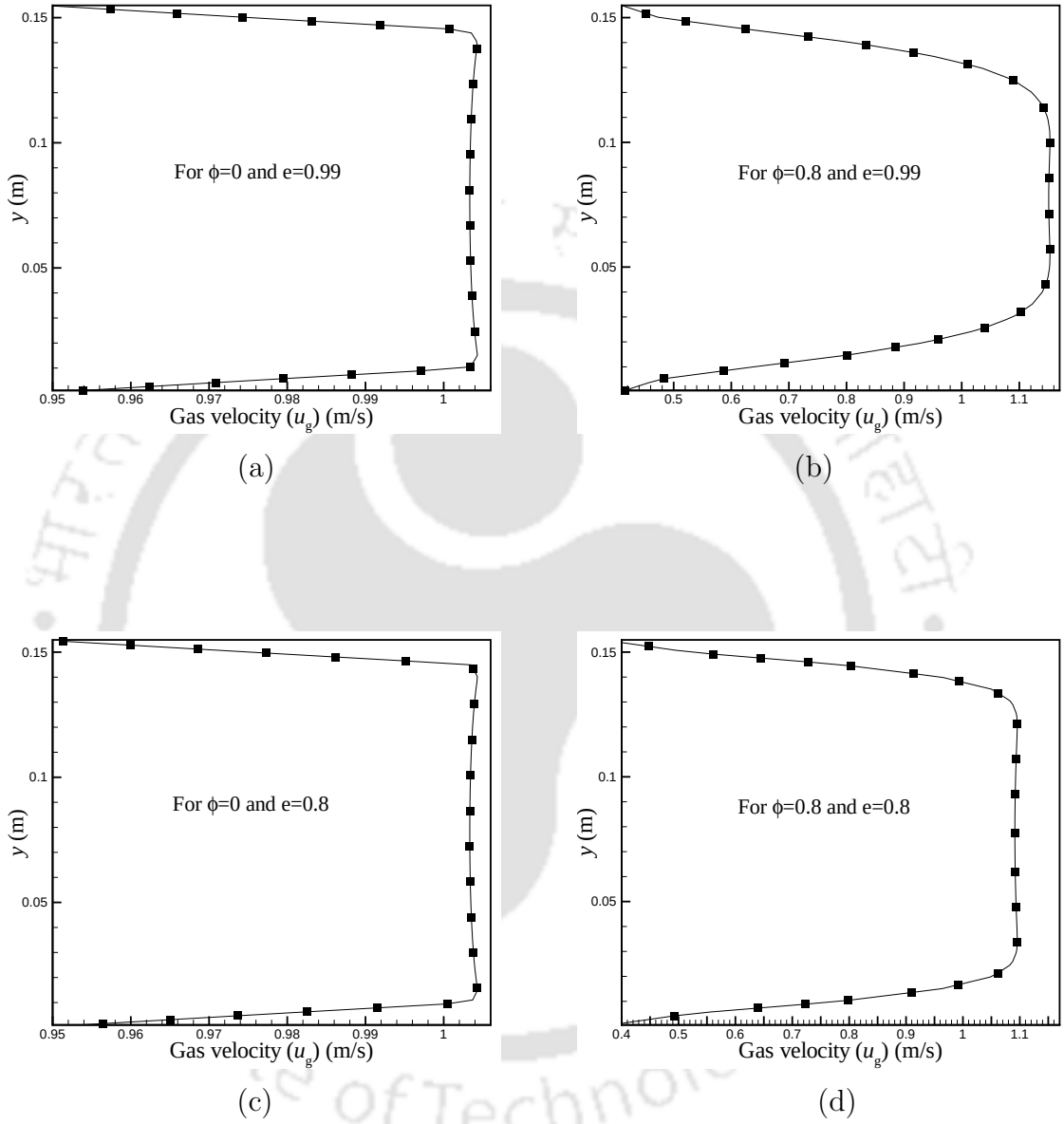

Figure 5.10: Comparison of plots of steady state gas velocity profiles for (a) ϕ=0, e=0.99; (b) ϕ=0.8, e=0.99; (c) ϕ=0, e=0.8 and (d) ϕ=0.8, e=0.8.

5.5.3 Comparison of particle phase volume fraction profiles

The steady state particle phase volume fraction profiles for the four sets of ϕ-e pairs plotted at the midplane of the channel (x=0.2 m) are shown in Figs. 5.11 (a), (b), (c) and (d). It can be observed from Figs. 5.11 (a) and (c) that when ϕ=0; there is no significant variation of particle phase volume fraction along the midplane of the channel and its value remains almost equal to the inlet value of particle phase

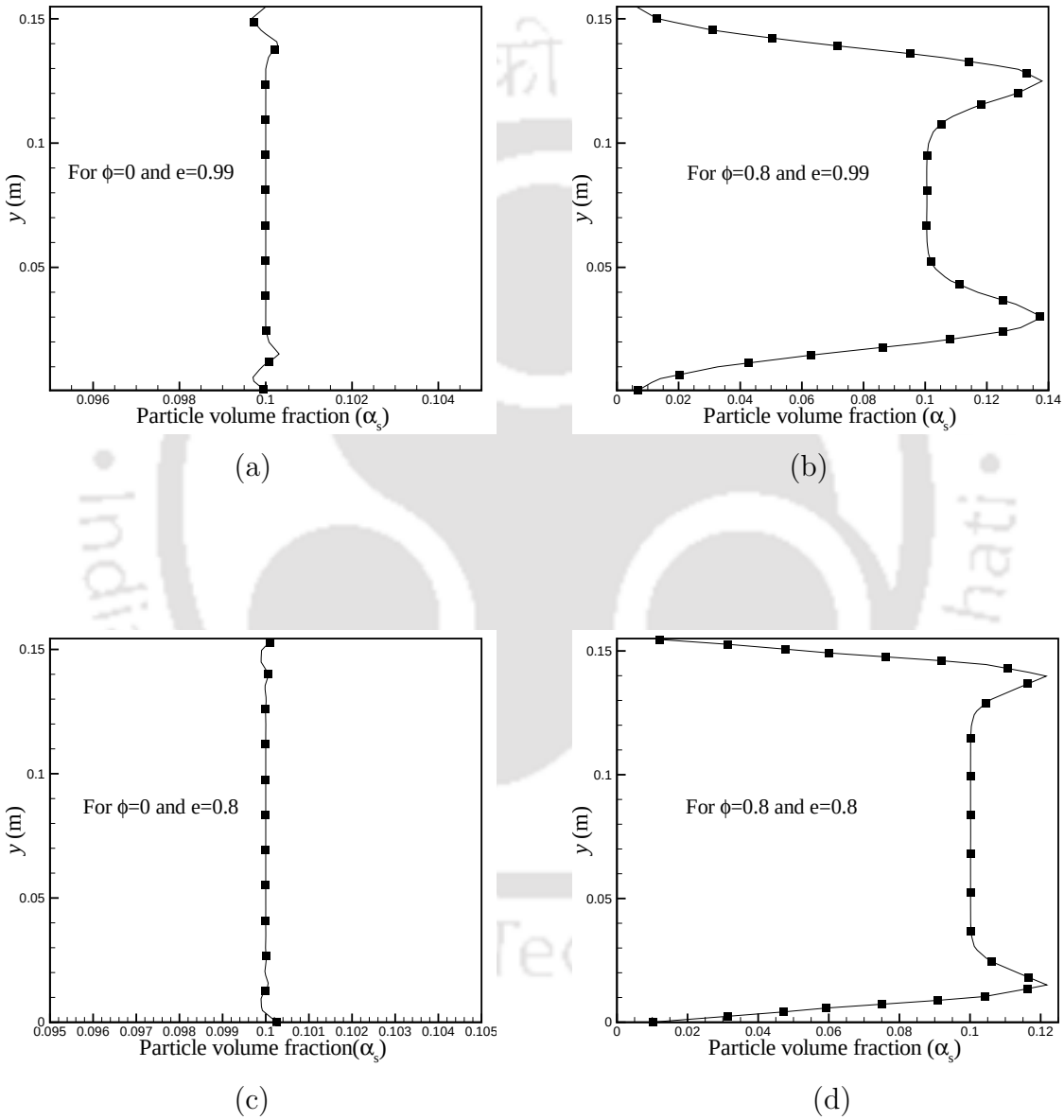

Figure 5.11: Comparison of plots of steady state particle volume fraction profiles for (a) ϕ=0, e=0.99; (b) ϕ=0.8, e=0.99; (c) ϕ=0, e=0.8 and (d) ϕ=0.8, e=0.8.

volume fraction; for both maximum and minimum values of e. But when the value of ϕ=0.8; there is significant variation of particle volume fractions for both the values of e, as can be seen in Figs. 5.11 (b) and (d). For ϕ=0.8; the volume fraction of the particle phase is minimum near the wall for both the values of e and tends to increase upto a certain distance away from the wall. The maximum value of particle volume fraction at the midplane of the channel is obtained for the combination of ϕ=0.8 and e=0.99. It can also be observed that the length of the region where steady state particle phase volume fraction is constant and equal to the inlet value is smaller for e=0.99 as compared to e=0.8; at a value of ϕ=0.8.

5.6 Effect of drag models

In many previously published works like Visuri et al. [94], Loha et al. [17], Zinani et al [76] etc., the effects of changing the drag model on the hydrodynamics of fluidized beds have been discussed. So, investigations have been carried out in order to examine whether changing the drag model has any effect on the problem discussed herein. In this regard, simulations have been carried out for ϕ=0, 0.8 for a value of e=0.9 and for e=0.8, 0.99 for a value of ϕ=0.8 using two well-known drag models namely Gidaspow drag model [86] and Syamlal-OBrien drag model [90]. For all these sets of values of ϕ and e, negligible changes in the phase velocity and volume fraction profiles have been observed for the two drag models. The steady state phase velocity and volume fraction profiles at the midplane of the channel (x=0.2 m) obtained by using both the drag models have been shown in Fig. 5.12 for one set of values of ϕ=0.8 and e=0.9. It can be clearly observed from Fig. 5.12 that for this particular flow situation, very little change occur in both steady state phase velocities and volume fraction profiles due to the change in the drag model. Hence, it can be concluded that changing the drag model for a particular set of values of ϕ and e does not bring any significant changes in the flow physics of dispersed laminar gas-particle flows through a horizontal channel.

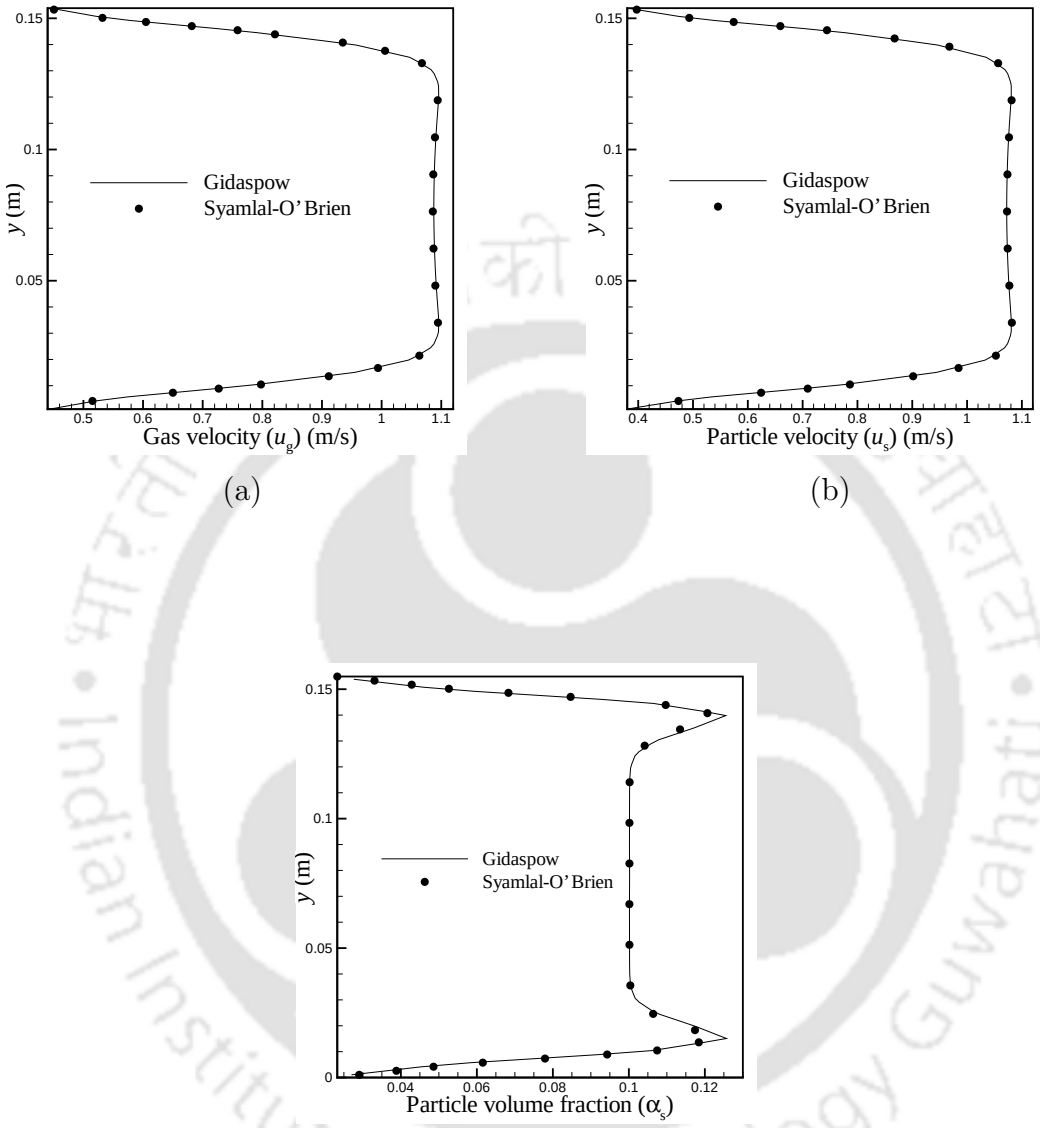

Figure 5.12: Comparison of plots of steady state (a) gas velocity, (b) particle velocity and (c) particle phase volume fraction profiles for ϕ=0.8, e=0.9 for two different drag models.

5.7 Study of wall shear stress distribution of individual phases

5.7.1 Particle phase

The value of wall shear stress of the particle phase is calculated using the following expression given by Johnson and Jackson [14].

$$\tau_{s,w} = -\frac{\pi}{6}\frac{\alpha_s}{\alpha_{s,\max}}\phi\rho_s g_o\sqrt{3\theta}\mathbf{u}_{s,w} \tag{5.1}$$

The steady state values of average wall shear stress for the particle phase have been shown in Table 5.5 for different values of ϕ at a particular value of e=0.99. It can be observed that with increase in the value of ϕ, the wall shear stress on the particle phase increases which causes lower particle velocity near the wall for higher values of ϕ.

Table 5.5: Value of average shear stress of the particle phase at the wall

Case	e	ϕ	τ_{avg}(-ve) (kg/m-s^2)
1	0.99	0.0	0
		0.5	1.452
		0.8	1.62

5.7.2 Gas phase

On the other hand, the gas phase wall shear stress is calculated using the formula

$$\tau_{w,gas} = \mu_g \frac{\partial u_g}{\partial y}\Bigg]_{wall} = \mu_g \frac{u_{g,wall} - u_{g,co}}{\Delta y} \tag{5.2}$$

Where $u_{g,wall}$ is the velocity at a particular face on the wall boundary and $u_{g,co}$ is the velocity of the gas phase at the cell center of the cell containing that face.

Δy is the perpendicular distance between the cell center and the face center. At the wall, the gas velocity is always zero due to no-slip boundary condition and the value of $u_{g,co}$ is influenced by the corresponding particle velocity at the cell center. As already discussed in Sections 5.3.1 and 5.3.2, the particle velocity near the wall is maximum for ϕ=0 and it decreases with increase in the value of ϕ. Hence, gas velocity near the wall also becomes maximum for ϕ=0 as the drag exerted by the particles is maximum in this case. So, the value of $u_{g,co}$ becomes maximum for ϕ=0 and as a result, the value of the gradient $\frac{\partial u_g}{\partial y}$ at the wall also becomes maximum. This is the reason why the magnitude of average wall shear stress of the gas phase is maximum for ϕ=0; at a particular value of e; as seen in Table 5.6. With increase in value of ϕ, due to decrease in particle velocity near the wall, the drag acting on gas phase decreases and hence, gas velocity also decreases near the wall which tend to lower the value of $\frac{\partial u_g}{\partial y}$ at the wall and as a consequence, it can be seen in Table 5.6 that average wall shear stress for gas phase decreases with increase in the value of ϕ.

Table 5.6: Value of average shear stress of the gas phase at the wall

Case	e	ϕ	τ_{avg}(-ve) (kg/m-s^2)
1	0.99	0.0	0.2956
		0.5	0.1726
		0.8	0.1618

5.8 Closure

In this chapter, a detailed study on the effects of ϕ and e on the hydrodynamics of dispersed gas-particle flows through horizontal channels have been presented. The analysis indicates that at a particular value of e, both gas and particle velocities at the centerline of the channel increase with increase in the value of ϕ, whereas near the wall, they tend to decrease. At a fixed non-zero value of ϕ, both gas and particle

velocities tend to increase with increase in the value of e. For ϕ=0, which corresponds to free-slip boundary condition for particle velocity, there is no significant variation in gas and particle velocities with changes in e. Out of all combinations of values of ϕ and e investigated herein, it is found that both gas and particle velocity attain a maximum value when both the values of ϕ and e are maximum. The value of average wall shear stress for the particle phase increases with increase in the value of ϕ whereas, for the gas phase, it decreases with increase in the value of ϕ.

Chapter 6

Effects of particle-particle and particle-wall interactions on recirculating flows through a sudden expansion

Separation and recirculation flow phenomena are greatly abundant in many natural as well as engineering applications. From the point of view of fluid mechanics, whenever there is an expansion in the area of cross-section of the flow, generally there is a flow separation and a recirculation zone is obtained. The best examples are flow over a backward facing step or flow through a sudden expansion. Dispersed gas-particle flows have applications in coal combustors, cyclone separators, air filters where there exist possibilities of flow separation. In this chapter, a detailed study is carried out in order to investigate the effects of particle-particle and particle-wall interactions on recirculating gas-particulate flows through a sudden expansion. The stretching or shrinking of recirculation zone which depends on the values of particle-particle restitution coefficient (e) and specularity coefficient (ϕ) could be vital in the design of gas-solid separators and air filters where there exists a distinct possibility of flow separation. So, as a first step towards better understanding the complex flow dynamics of such flow situations, this study has been taken up in this chapter.

6.1 Problem definition

The present investigations are targeted at an extensive study of dispersed gas-particle flows through a sudden expansion in order to determine the effects of particle-wall and particle-particle interactions on the recirculation lengths. To fulfill this objective, a two-dimensional planer sudden expansion has been considered as a representative geometry as shown in Fig. 6.1. The height of the inlet channel is

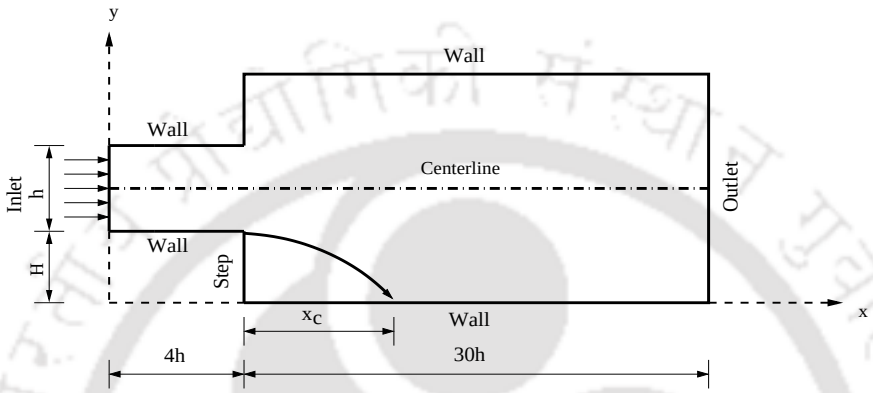

Figure 6.1: Schematic of the sudden expansion geometry considered for the simulations.

taken to be h=0.05 m, while the step height is considered as 0.035 m. The height of the channel at the outlet is taken as $2.4h$. The gas phase is air with a density of 1.2 kg/m^3 whereas the particle phase has a density of 500 kg/m^3 and the diameter of the solid particles is taken as 530 μm. Both the phases enter the domain with equal velocity of 1 m/s with the particle volume fraction equal to 2% at the inlet. The flow Reynolds number is taken to be 200 based on the height of the channel outlet. The entrance length is taken to be equal to $4h$ while the length of the main channel is taken as $30h$. It has been observed that for this geometry and flow and fluid parameters, the resulting flow remains symmetric and in the laminar regime. Therefore, in order to save computational time, only half of the domain has been solved in all studies. Simulations have been carried out for five different values of e (e=0.99, 0.95, 0.9, 0.85 and 0.8), ranging from very close to perfectly elastic collisions (e=0.99) to highly inelastic collisions (e=0.8) and at a fixed value of ϕ=0.2 in order to investigate the influence of the change in the value of e on the recirculation characteristics. Likewise, at a fixed value of e=0.85, simulations are carried out for five different values of ϕ (ϕ=0, 0.2, 0.5, 0.8 and 1), ranging from a free-slip boundary

condition (ϕ=0) to a no-slip boundary condition (ϕ=1) for particle velocity in order to examine if and by how much changes in the values of ϕ while keeping all other parameters invariant can influence the recirculation characteristics. Finally, a study is performed for different combinations of values of ϕ and e in order to find the combined effect of these pair of parameters in the overall recirculation characteristics. The simulation parameters have been listed in the Table 6.1.

Table 6.1: Parameters used for simulation for dispersed gas-particle flow through the sudden expansion

Simulation parameters	Values
Inlet gas velocity (u_g)	1.0 m/s
Inlet particle velocity (u_s)	1.0 m/s
Inlet Particle volume fraction (α_s)	2%
Gas density (ρ_g)	1.2 kg/m^3
Particle density (ρ_s)	500 kg/m^3
Particle diameter (d_s)	530 μm
Flow Reynolds number (Re) (Based on outlet height)	200
Specularity coefficient (ϕ)	0, 0.2, 0.5, 0.8, 1
Particle restitution coefficent (e)	0.99, 0.95, 0.9, 0.85, 0.8

6.2 Grid independence study

In flows involving separation and recirculation, the main challenge lies in predicting the length of the recirculation zone accurately using a computational grid of optimum resolution. In the present study, a grid independence study has been conducted using four grids of different resolutions with the coarsest grid having 7,600 cells and the finest having 19,000 cells. The details of the four meshes are given in Table 6.2. Considering the flow and physical parameters mentioned in Section 6.1, simulations are carried out in each of the four meshes assuming ϕ=1 and e=0.8. The

recirculation lengths obtained on these four grids have been summarized in Table 6.2. It can be seen in Table 6.2 that the deviation in recirculation lengths obtained from the meshes $G3$ and $G4$ is acceptably small. Therefore, it can be argued that the mesh $G3$ can provide a grid independent solution and all subsequent investigations are carried out on this mesh with 15,200 cells.

Table 6.2: Recirculation lengths obtained for computational grids of different sizes

Grid	Number of cells	δx and δy (m)	Recirculation length (m)
G1	$7,600$	δx=0.005, δy= 0.5 $\times$ δx	1.28
G2	$11,400$	δx=0.005, δy= 0.33 $\times$ δx	1.325
G3	$15,200$	δx=0.005, δy= 0.25 $\times$ δx	1.34
G4	$19,000$	δx=0.005, δy= 0.2 $\times$ δx	1.3406

6.3 Effect of variation of particle-particle restitution coefficient on recirculation characteristics

In order to investigate the effects of the variations in the values of particle-particle restitution coefficient (e), five different values of e viz. 0.99, 0.95, 0.9, 0.85 and 0.8 have been used. The changes in the recirculation lengths for flow in the sudden expansion for different values of e have been studied at a fixed value of ϕ=0.2 (shown in Fig. 6.2). It must be emphasized here that a lower value of e signifies more loss of particle momentum due to particle-particle collisions and this loss decreases as the value of e approaches unity. The analyses carried out in this work clearly show that the simulation results are sensitive to the changes in the values of e since in the two-fluid model adopted in this study, solid phase properties (which appear in particle momentum equation) like solid pressure and solid phase shear viscosity are empirically calculated as functions of e. It can be seen from Fig. 6.2 that there

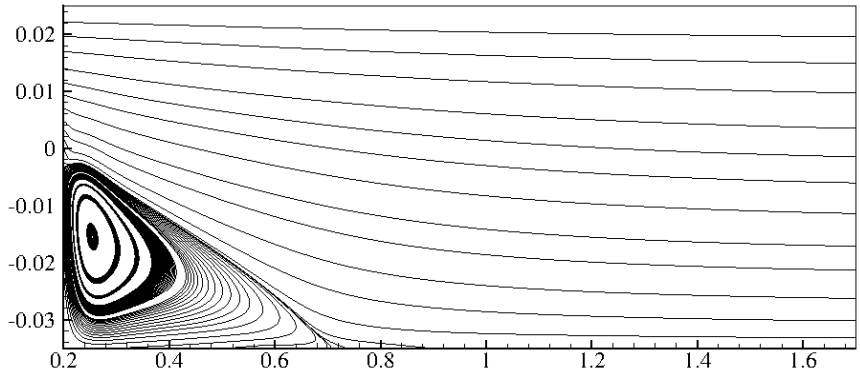

(a)

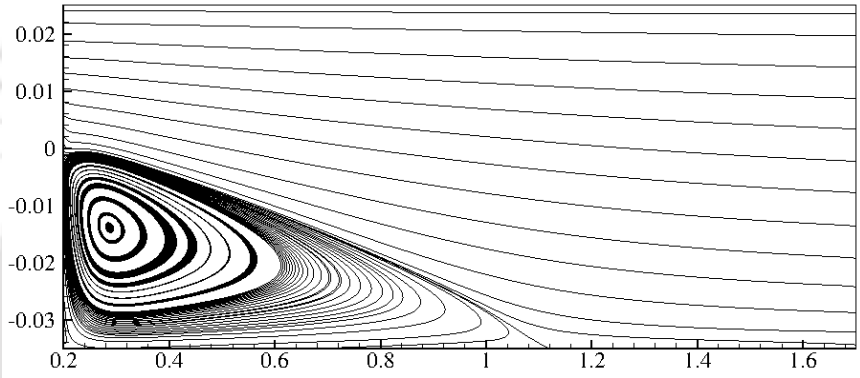

(b)

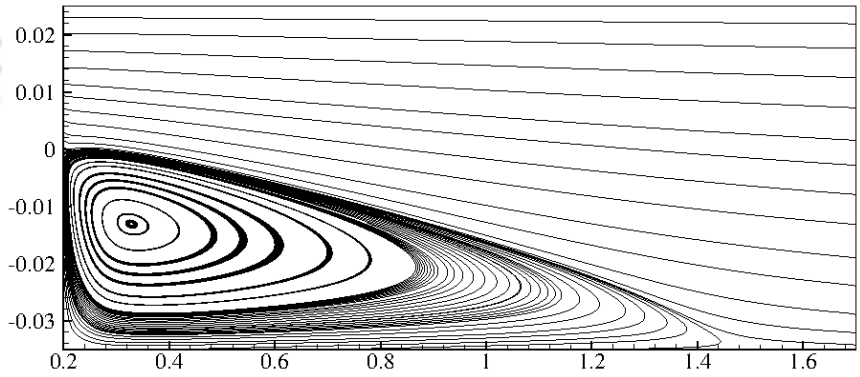

(c)

Figure 6.2: Recirculation zones obtained at the vicinity of the step for (a) e=0.99, (b) e=0.95 and (c) e=0.8; for ϕ=0.2

is a significant change in the recirculation lengths as the value of e is varied at a particular value of ϕ. The length of the recirculation zone downstream of the step is found to increase with decrease in the value of e i.e., the minimum length of the recirculation zone has been obtained for e=0.99 where almost perfectly elastic collisions occur among the particles (seen in Fig. 6.2(a)) and it increases as the value of e decreases (seen in Figs. 6.2(b) and 6.2(c)). The reason for such an observation can be attributed to the fact that a lower value of e signifies more kinetic energy dissipation due to particle-particle collisions and as the particles are dispersed in the gas, a part of this dissipated kinetic energy is transmitted to the gas. Since the dissipation of kinetic energy is more for lower values of e, so the kinetic energy transmitted from the particles to the continuous gas phase also becomes more for lower values of e which in turn has a stretching effect on the recirculation zone. Figure 6.3 (a) shows the variations of recirculation length (x_c) with the variations in the values of e at ϕ=0.2.

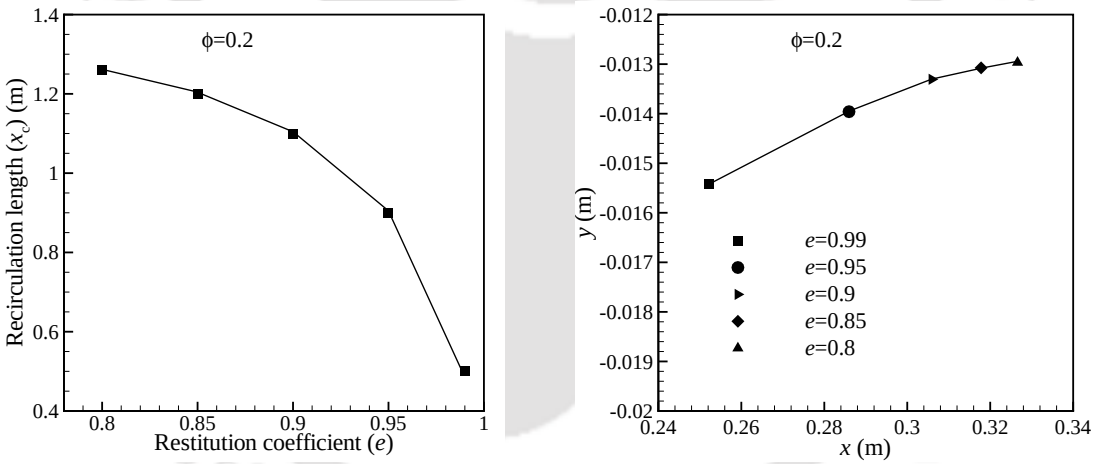

Figure 6.3: (a) Variation of recirculation lengths with e at ϕ=0.2, (b) variation of co-ordinates of the vortex eye with e at ϕ=0.2

It can be clearly observed from Fig. 6.3 (a) that there is a continuous decrease in the values of recirculation length past the step as the value of e is increased from 0.8 to 0.99. Between these two extreme values of e, the value of the recirculation length is found to decrease from 1.26 m to 0.5 m with the sharpest decrease has been found as the value of e is changed from 0.95 to 0.99. Figure 6.3(b) shows the co-ordinates

of the vortex eye for all the five values of e and it can be observed that when the value of e is decreased from 0.99 to 0.8, the vortex eye tend to shift upwards and to the right. Overall, it can be concluded from the above analysis that for the chosen value of ϕ and all other parameters being invariant, the length of the recirculation zone is the lowest when the value of e is maximum and highest when the value of e is minimum.

6.4 Effect of variation of specularity coefficient on recirculation characteristics

The value of specularity coefficient (ϕ) physically determines the amount of particle momentum lost due to collisions with the wall. In the two fluid model, the value of ϕ is used to derive the boundary conditions of particle velocity at the solid walls and different values of ϕ indicate different amounts of momentum lost due to particle-wall collisions. In order to study the effects of variations in the values of ϕ on the recirculation characteristics, five different values of ϕ (ϕ=0, 0.2, 0.5, 0.8 and 1) have been considered. ϕ=0 represents no loss of particle momentum due to particle-wall collisions (free-slip boundary condition) and ϕ=1 signifies 100% momentum loss due particle-wall collisions (no-slip boundary condition). The changes in the recirculation lengths for these values of ϕ have been studied at e=0.85, keeping all other physical and flow parameters invariant.

The recirculation zones for three values of ϕ (ϕ=0, 0.2 and 1) have been shown in Fig. 6.4. It can be observed that keeping all other parameters invariant, when the value of ϕ is varied from 0 to 1, there is a small but gradual increase in the recirculation length. The reason behind this marginal increase in the recirculation length may be understood from the variation of particle velocity near the wall with change in the value of ϕ. For ϕ=0, the particle velocity near the wall is highest as no particle momentum is lost due to collisions with the wall while the particle velocity decreases near the wall as the value of ϕ is increased becoming minimum for ϕ=1. Hence, the drag exerted by the particles near the wall inside the recirculation zone on the gas phase is minimum for ϕ=1 while the drag increases as the value of ϕ tends to zero. As a result, when all other flow and physical parameters are kept

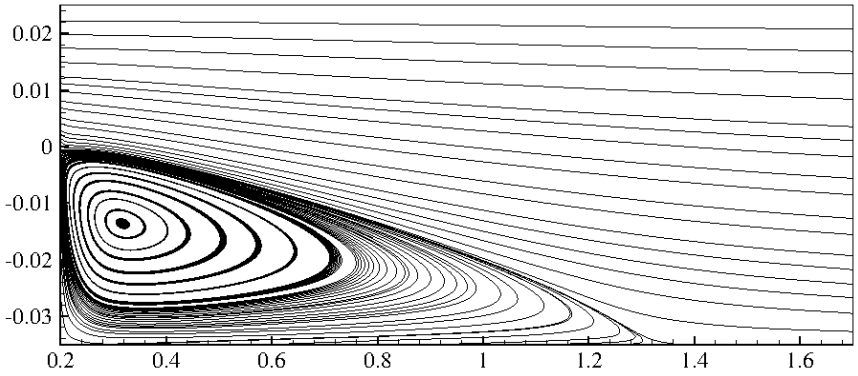

(a)

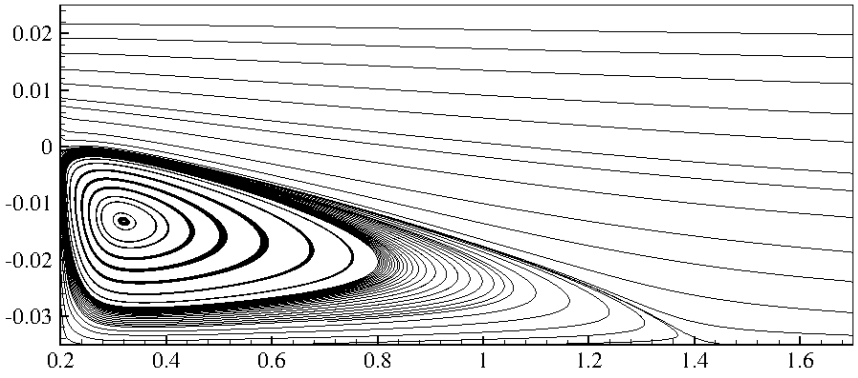

(b)

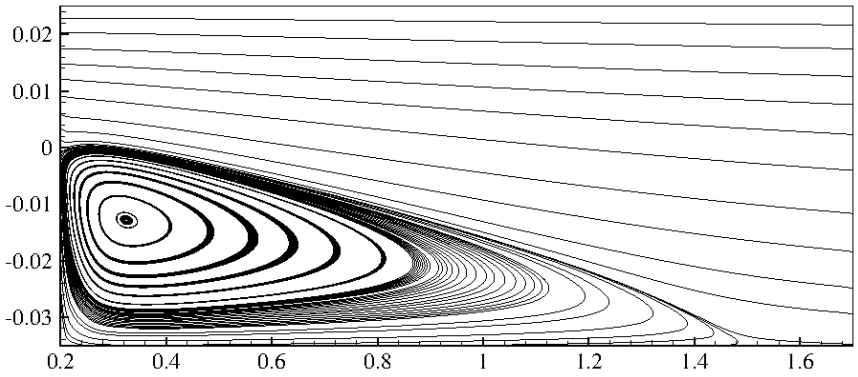

(c)

Figure 6.4: Recirculation zones obtained at the vicinity of the step for (a) ϕ=0, (b) ϕ=0.2 and (c) ϕ=1; for e=0.85

invariant, the length of the recirculation zone past the step shows a small gradual increase with increase in the value of ϕ, at a particular value of e. However, this increase in the length of the recirculation zone is not as significant as it has been seen in case of variation of e (in Section 6.3) due to the reason that unlike e, the value of ϕ have effects on the flow only at the wall and not anywhere else inside the domain.

Figure 6.5 (a) shows the variations in the recirculation lengths for all the five values of ϕ for e=0.85. It can be observed that the recirculation length shows a gradual increase with a value of 1.1 m for ϕ=0 upto a value of 1.3 m for ϕ=1. The co-ordinates of the vortex eye for all values of ϕ have been shown in Fig. 6.5 (b) where a marginal shift upwards and to the right has been observed. Overall, it may be concluded from the above analysis that at a particular value of e and for all other parameters being invariant, the length of the recirculation zone past the step increases gradually with increase in the value of ϕ, but at a much lesser rate than that observed in case of variation of e, discussed in Section 6.3.

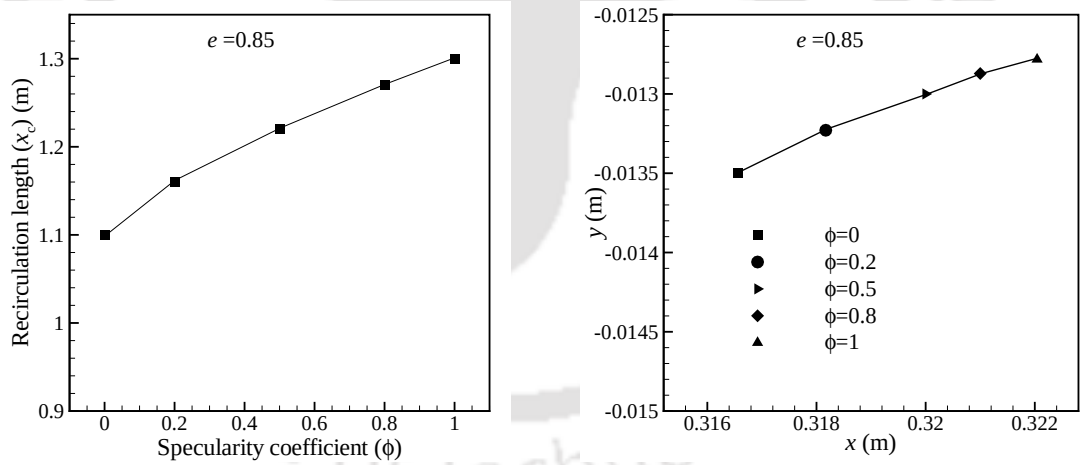

Figure 6.5: Variation of recirculation lengths with ϕ at e=0.85, (b) variation of co-ordinates of the vortex eye with ϕ at e=0.85

6.5 Comparison of recirculation lengths for different combinations of ϕ-e pairs

In Sections 6.3 and 6.4, studies have been carried out to investigate the effects of e for fixed ϕ and ϕ for fixed e respectively on the recirculation characteristics of dispersed gas-particle flows through a sudden expansion. It is therefore more illustrative to study the combined effects of ϕ-e and in this section, the variations in the recirculation lengths have been studied for four different combinations listed below.

- ϕ=0, e =0.8 (minimum,minimum).
- ϕ=0, e =0.99 (minimum,maximum).
- ϕ=1, e =0.8 (maximum,minimum).
- ϕ=1, e =0.99 (maximum,maximum).

Figure 6.6 shows the recirculation zones obtained at the vicinity of the step for these four combinations of values of ϕ and e. Out of the above four combinations, it can be seen that maximum recirculation length has been obtained in the case shown in Fig. 6.6(c) (for ϕ=1, e=0.8) and the minimum recirculation length has been obtained in the case shown in Fig. 6.6(b) (for ϕ=0, e=0.99).

Figure 6.7 shows variations in recirculation lengths with ϕ and e. It is clear from Fig. 6.7 that at a particular value of ϕ, there is a continuous decrease of recirculation length with increase in the value of e where the sharpest decrease has been found when the the value of e is changed from 0.95 to 0.99. Likewise, at a particular value of e, the recirculation length is found to increase with increase in the value of ϕ and the maximum variation in recirculation length with ϕ has been found for e=0.8. A closer look at the Figs. 6.6 and 6.7 shows that the recirculation length is maximum when the value of ϕ is maximum and e is minimum whereas; recirculation length is minimum when the value of ϕ is minimum and the value of e is maximum. This indicates that the length of the recirculation zone considering particle-particle and particle-wall interactions discussed herein shows a direct dependence on ϕ and an inverse dependence on e, with the former dependence weaker than the later.

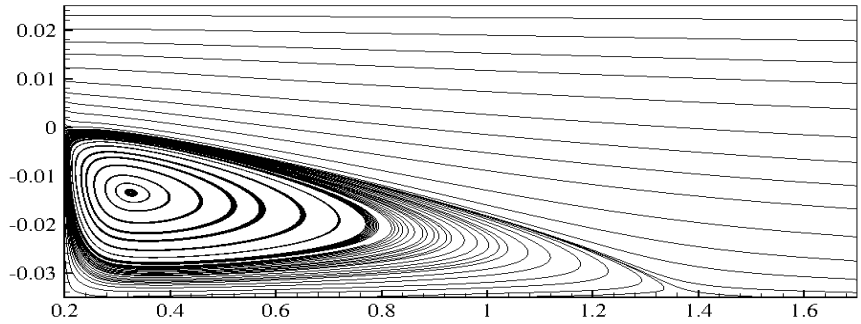

(a)

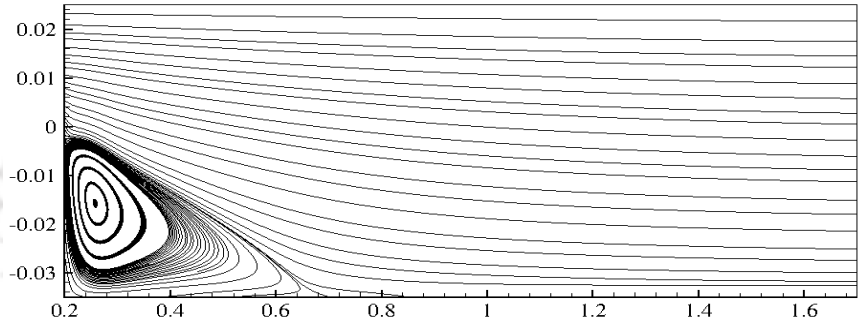

(b)

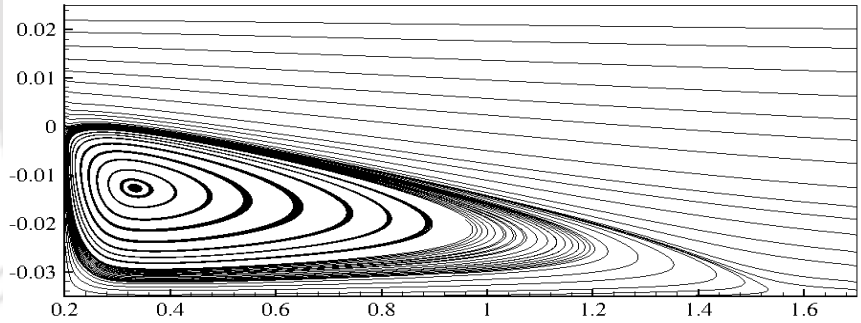

(c)

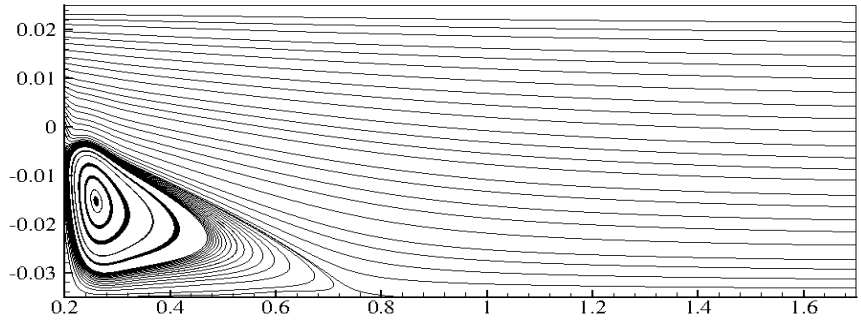

(d)

Figure 6.6: Recirculation zones obtained at the vicinity of the step for (a) ϕ=0, e=0.8, (b) ϕ=0, e=0.99 and (c) ϕ=1, e=0.8 for and (d) ϕ=1, e=0.99

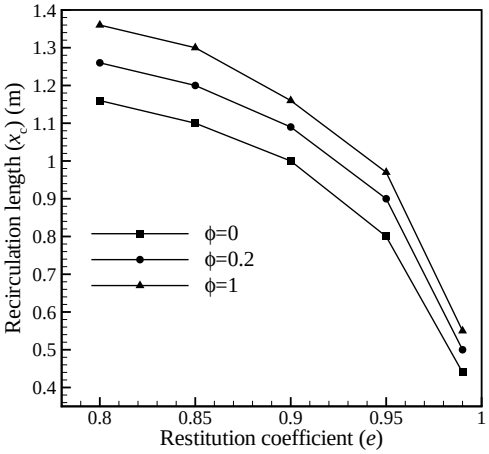

Figure 6.7: Variations of recirculation length for different values of e and ϕ

6.6 Closure

In this chapter, a detailed study has been presented on the effects of ϕ and e on the recirculation characteristics of dispersed gas-particle flows through a sudden expansion. Investigations have also been carried out to find the ϕ-e pair for which the recirculation lengths are an extremum. It has been found that for a particular value of ϕ, the recirculation lengths tend to decrease with increase in the value of e, when other parameters kept invariant. On the contrary for a fixed value of e, the recirculation lengths tend to increase gradually with increase in the value of ϕ although the changes are not as significant as those obtained in the case of variation of e. Among all possible combinations of values of ϕ and e investigated herein, the maximum value of the recirculation length past the expansion is obtained when the value of ϕ is maximum and that of e minimum.

Chapter 7

Simulation of bubbling gas-solid fluidized beds

Fluidization is a physical process of transforming solid particles into a fluid-like state by suspending them in a gas medium (discussed in details in Section 1.5). Gas-solid fluidized bed is an industrial application which utilizes this concept of fluidization of solid particles. The solid particles which are placed on the bed are subjected to a gas flow from below at a certain velocity so that the the gas drag on the particles is large enough to overcome gravity. In the fluidized state, the moving particles work effectively as a mixture, which in turn results in a uniform temperature and a high mass transfer rate [15]. The smallest value of inlet gas velocity at which fluidization occurs is referred to as minimum fluidization velocity.

Among the different categories of fluidized beds, one common type is the bubbling gas-solid fluidized beds wherein the inlet velocity of the fluidizing gas is relatively low (generally of the order or few times higher than the minimum fluidization velocity) and so, the fluidization zone is relatively stationary with very few particles being entrained from the bed. Due to the low values of gas inlet velocities, interphase forces other than the drag force (like lift force and virtual mass force) become insignificant in case of these beds and the resulting flow inside the bed can be considered as laminar [17]. In this chapter, extensive validations of the developed flow solver for bubbling gas-solid fluidized beds are carried out along with a parametric study in order to understand the influence of the changes in the values of particle diameter on

the fluidization characteristics. It must however be mentioned here that the present study is limited to two-dimensional flow problems in laminar conditions and should be considered as a first attempt to apply the gas-particulate flow solver developed in this work to a practical problem of interest.

7.1 Validation study of bubbling gas-solid fluidized beds

In this section, a detailed validation of the flow solver with full three-way coupling is carried out in order to assess its ability to handle high density particles in bubbling gas-solid fluidized beds where volume fraction of the particles is close to the packing limit ($\alpha_{s,max}$). Two validation studies are carried out and in both the studies, the particles are initially placed on the bed of the chamber (at t=0 s) and the fluidizing agent gas (generally air) enters from the bottom with a certain value of velocity higher than the minimum fluidization velocity which is capable of fluidizing the solid particles resting on the bed. Comparison of the results obtained for these two cases with both numerical and experimental data is presented for both orthogonal and non-orthogonal grids.

7.1.1 Validation problem 1

The first problem simulated using the developed solver has been taken from Passalacqua and Fox [103]. In this problem, the fluidized bed configuration is of 0.138 m width and 1 m height as shown in Fig. 7.1. The particle phase is of material density ρ_s=2000 kg/m^3 with particle diameter of 350 μm. Initially, the bed is filled with particles upto a height of 0.2 m with a volume fraction α_s=0.58. The details of the simulation parameters are shown in Table 7.1. The grid used in the simulation of the above problem in Passalacqua and Fox [103] is of 1400 quadrilateral cells which corresponds to a grid size of 0.01 m. It has been reported that this grid has provided a grid independent solution for the problem stated above. This problem is simulated with the inhouse flow solver using two grids, one is made of uniform quadrilateral cells, while the other is made of triangular cells, both having a grid size of 0.01 m. The simulations for this particular case is run upto a physical time equal to 30 s. Time-averaging of the variables is carried out for the last 25 s of the

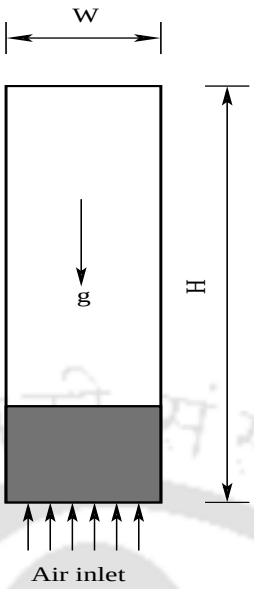

Figure 7.1: Schematic of the domain of the fluid bed configuration

Table 7.1: Parameters used for the validation of bubbling gas-solid fluidized bed

Simulation parameters	Values
Initial Particle volume fraction (α_s)	0.58
Initial bed height	0.2 m
Inlet gas velocity (v_g)	0.54 m/s
Gas density (ρ_g)	1.4 kg/m^3
Particle density (ρ_s)	2000 kg/m^3
Particle diameter (d_s)	350 μm
Specularity coefficient (ϕ)	0.5
Particle restitution coefficent (e)	0.8
Maximum packing limit ($\alpha_{s,max}$)	0.63
Minimum volume fraction ($\alpha_{s,min}$)	0.5

simulations (i.e., between 5 to 30 s). The instantaneous contours of volume fraction obtained with the triangular grid at different instances of time have been shown in Fig. 7.2. Figures 7.3 (a) and (b) show the comparisons of the results obtained from

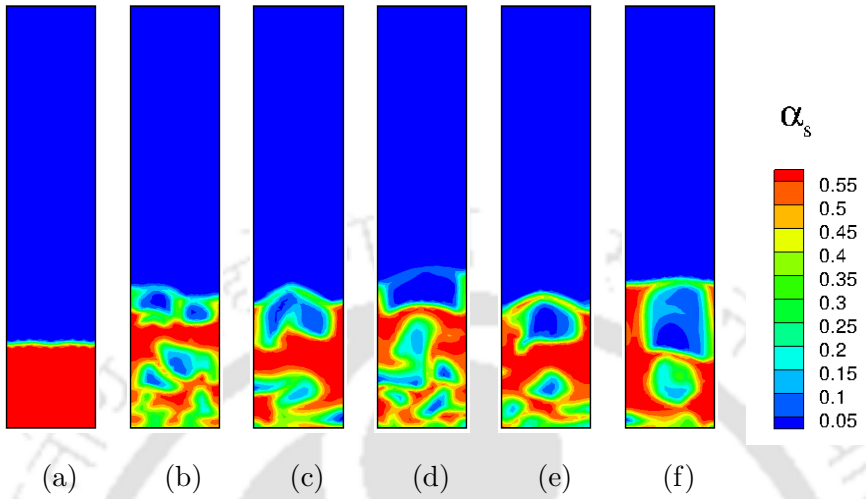

Figure 7.2: Contours of particle phase volume fractions obtained at (a) t=0 s, (b) t=1 s, (c) t=5 s, (d) t=10 s, (e) t=20 s and (f) t=30 s; from the grid having triangular cells.

the developed solver with those given in [103] for two different time-averaged quan-

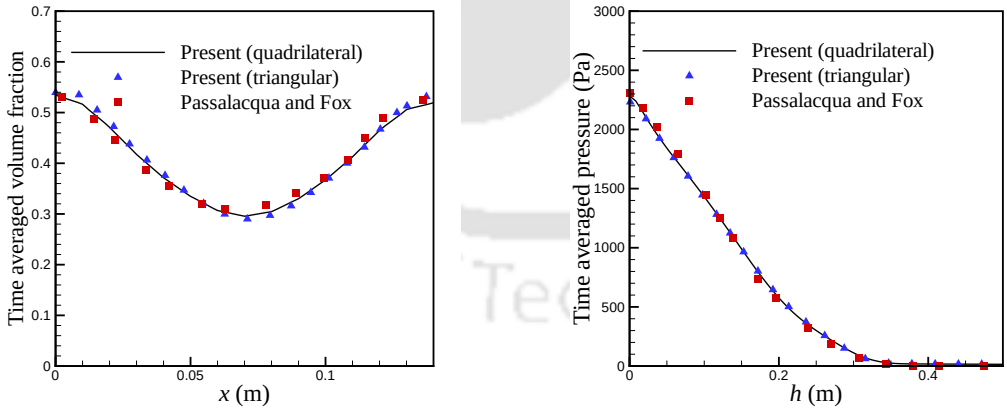

Figure 7.3: (a) Comparison of radial variation of time-averaged particle volume fraction profile, (b) comparison of axial variation of pressure

tities. The comparison of the variation of time-averaged particle volume fraction in the radial direction at H=0.2 m (measured from the bottom) has been shown in Fig. 7.3 (a) while the variation of time-averaged pressure in the axial direction is compared in Fig. 7.3 (b). A good agreement has been observed in the comparisons of both the time-averaged quantities for both the grids with the results given in [103].

7.1.2 Validation problem 2

The second test case simulated using the flow solver for validation purpose is taken from the work of Taghipour et al. [70] which is also solved numerically by Liu et al. [88]. In this problem, the fluidized bed configuration is of 0.28 m width and 1 m height. The particle phase is of material density ρ_s=2500 kg/m^3 with particle diameter of 280 μm. Initially, the bed is filled with particles upto a height of 0.4 m with a volume fraction α_s=0.6. The details of the simulation parameters are shown in Table 7.2.

Table 7.2: Parameters used for the validation of the bubbling gas-solid fluidized bed

Simulation parameters	Values
Initial Particle volume fraction (α_s)	0.6
Initial bed height	0.4 m
Inlet gas velocity (v_g)	0.46 m/s
Gas density (ρ_g)	1.2 kg/m^3
Particle density (ρ_s)	2500 kg/m^3
Particle diameter (d_s)	280 μm
Specularity coefficient (ϕ)	0.5
Particle restitution coefficent (e)	0.8
Maximum packing limit ($\alpha_{s,max}$)	0.63
Minimum volume fraction ($\alpha_{s,min}$)	0.5

The instantaneous volume fraction contours at different time instances during the course of the simulation are shown in Fig. 7.4. The simulations are carried out with a time step (Δt) equal to 10^{-4} and upto a physical time of 60 s. Fig. 7.5 shows the variation of the time-averaged particle volume fraction (done between 5 to 30 s of simulation time) along the radial direction at a height h=0.2 m from the bottom

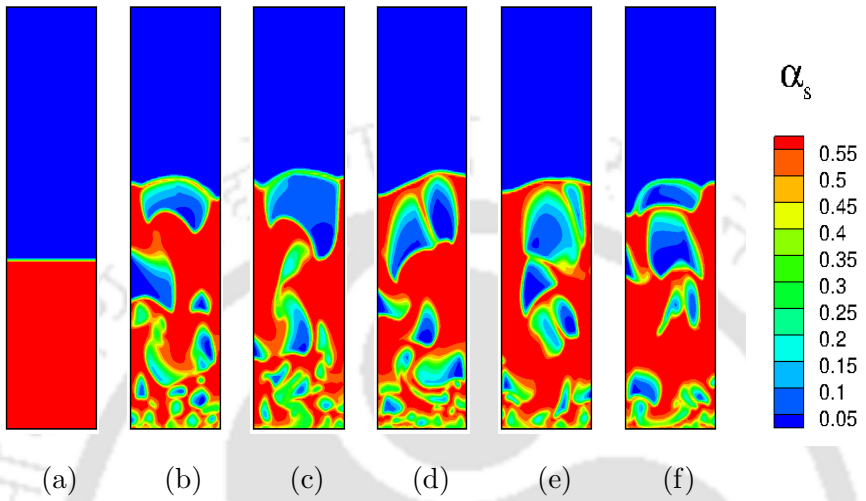

Figure 7.4: Contours of particle phase volume fractions obtained at (a) t=0 s, (b) t=5 s, (c) t=10 s, (d) t=15 s, (e) t=25 s and (f) t=30 s.

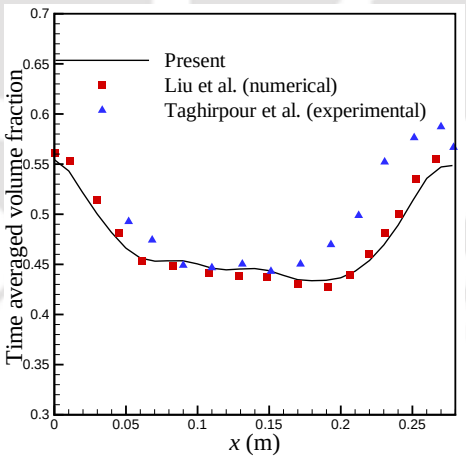

Figure 7.5: Comparison of time-averaged volume fraction along the radial direction

of the domain obtained from the developed solver. It has been compared with both the numerical results of Liu et al. [88] and experimental results of Taghipour et

al. [70] in Fig. 7.5. It can be observed that the present results are in very good agreement with the numerical results of Liu et al. [88], while a reasonable agreement can be observed with the experimental results of Taghipour et al. [70].

These studies collectively demonstrate the applicability of the flow solver in simulating gas-particulate flows in bubbling gas-solid fluidized beds.

7.2 Study of effects of particle diameter on fluidization characteristics

In this section, the flow solver is applied in order to study the effects of particle diameter on fluidization characteristics of bubbling gas-solid fluidized beds. It has been observed in literature that very few studies have reported the effects of variation of particle diameter (Stokes number) on the overall fluidization characteristics of bubbling gas-solid fluidized beds for all other parameters remaining constant. In particular, the changes in the time-averaged phase velocity and volume fraction profiles due to the change in particle diameter have not been discussed in details. Hence, in this section, a numerical study is carried out using the flow solver to find out the effects of change of particle diameter on the fluidization characteristics of bubbling gas-solid fluidized beds.

Problem definition

The effects of change of particle diameter are studied inside fluidized bed reactor of height, H=0.9 m and width, W=0.12 m shown schematically in Fig. 7.6. The fluidizing agent is considered to be air with density 1.2 kg/m^3 whereas the particle phase is considered to have a density of 2000 kg/m^3. Initially, the bottom half of the bed (upto a height H=0.4 m) is filled up with particles with a volume fraction α_s=0.58. The air is introduced from the bottom of the bed with a uniform velocity of 0.54 m/s which is higher than the minimum fluidization velocity and large enough to fluidize the particles on the bed. In order to study the effects of particle diameter on the hydrodynamics, simulations are carried out for five values of particle diameter (d_s= 300 μm, 350 μm, 400 μm, 450 μm and 500 μm) keeping all other parameters invariant. Table 7.3 provides the details of the simulation parameters used in this

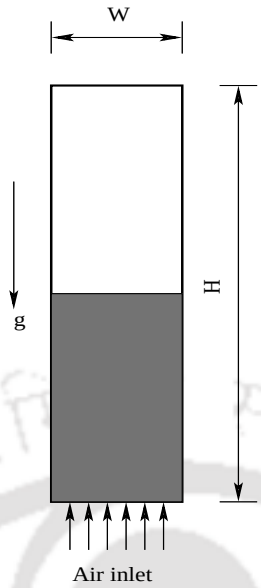

Figure 7.6: Schematic of the channel used for study of effects of particle diameter on fluidization

Table 7.3: Parameters used for study of effects of particle diameter

Simulation parameters	Values
Initial Particle volume fraction (α_s)	0.58
Initial bed height	0.4 m
Inlet gas velocity (v_g)	0.54 m/s
Gas density (ρ_g)	1.2 kg/m^3
Particle density (ρ_s)	2000 kg/m^3
Particle diameter (d_s)	300,350,400,450,500 μm
Specularity coefficient (ϕ)	0.5
Particle restitution coefficent (e)	0.8
Maximum packing limit ($\alpha_{s,max}$)	0.63
Minimum volume fraction ($\alpha_{s,min}$)	0.5

study.

Regarding the optimum value of grid size in bubbling gas-solid fluidized beds, Gelderbloom et al. [104] concluded that the when the grid size is of the order of ten times the particle diameter, the bubble size computed with that grid showed closer agreement with experimental results which has been followed in the subsequent studies of Jung et al. [106] and Loha et al. [17, 73, 74]. In the present study, simulations are carried out for five different values of particle diameter and so a grid of 6750 uniform quadrilateral cells with a grid size of 0.004 m, which is of the order of ten times of the average of the simulated particle diameters, is used for the simulations.

7.3 Effects on the fluidization behavior

The effects of particle diameter on the fluidization behavior of bubbling gas-solid fluidized beds are studied for the parameters mentioned in Table 7.3. The problem being inherently unsteady, simulations are carried out for a time period of 30s and time-averaging has been done between 5 to 30 s of physical time to get time-averaged values of different flow and physical quantities. Figure 7.7 (a), (b), (c), (d) and (e) show the time-averaged particle phase volume fraction contours for particle diameters 300 μm, 350 μm, 400 μm, 450 μm and 500 μm respectively. It can be observed from Fig. 7.7 that there is a significant change in the time-averaged volume fraction contours with change in the particle diameter for all other parameters remaining invariant. With increase in the particle diameter, the particles tend to settle more towards the bottom part of the reactor and so, the volume fraction near the bottom increases with particle diameter. Hence, it is seen that the value of time-averaged particle phase volume fraction at the bottom of the reactor increases gradually from Fig. 7.7 (a) to Fig.7.7 (e) as the particle diameter increases from 300 μm to 500 μm. It is due to the reason that the higher diameter (higher Stokes number) particles are influenced more by their inertia and gravitational fields than the lower diameter particles and so with time, the higher diameter particles have more tendency to settle at the bottom parts of the domain. Due to this tendency of the higher diameter particles, a gradual but prominent decrease in the length of the fluidization zone can be observed with increase in particle diameter in Fig. 7.7.

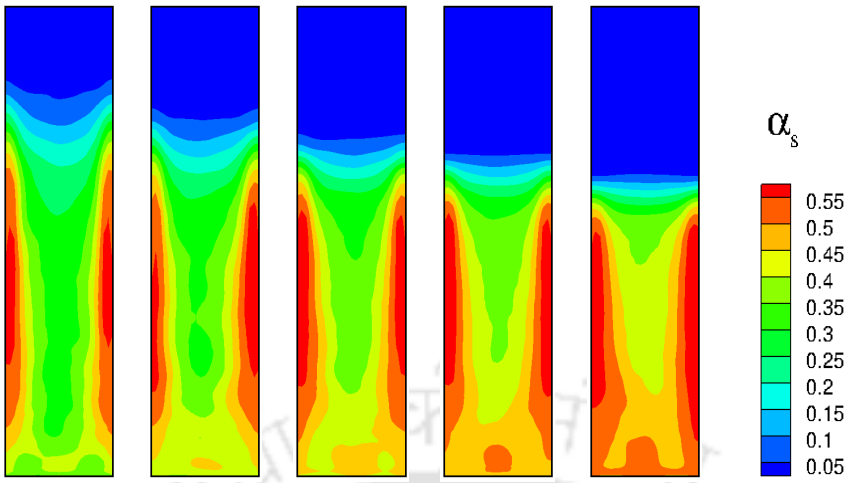

Figure 7.7: Time-averaged particle volume fraction contours for particle diameter of (a) 300 μm, (b) 350 μm, (c) 400 μm, (d) 450 μm and (e) 500 μm.

7.4 Effects on time-averaged particle velocity profiles

In order to investigate the effects of particle diameter on the time-averaged particle velocity profiles, the profiles of time-averaged particle velocity obtained for four values of particle diameter have been plotted at three different sections h=0.2 m, h=0.3 m and h=0.4 m (measured from the bottom) of the reactor in Fig. 7.8 (a), (b) and (c) respectively. It can be observed that at all the three sections inside the channel, there is distinguishable variations in the time-averaged particle velocity profiles obtained for particles with different diameters. At any particular section, it is seen that maximum value of time-averaged particle velocity has been obtained for particles with lowest diameter and vice-versa. The reason for this can be attributed to the fact that the lower diameter particles are more readily influenced by the interphase momentum exchanges and changes in the gas phase velocity fields than the higher diameter particles. Hence, it is observed from Figs. 7.8 (a), (b) and (c) that at all the three sections, maximum velocity is obtained for particles with the lowest diameter and minimum velocity is obtained for the particles with the highest diameter. Table 7.4 shows the maximum values of time-averaged particle velocity obtained inside the channel where a continuous decrease in the maximum

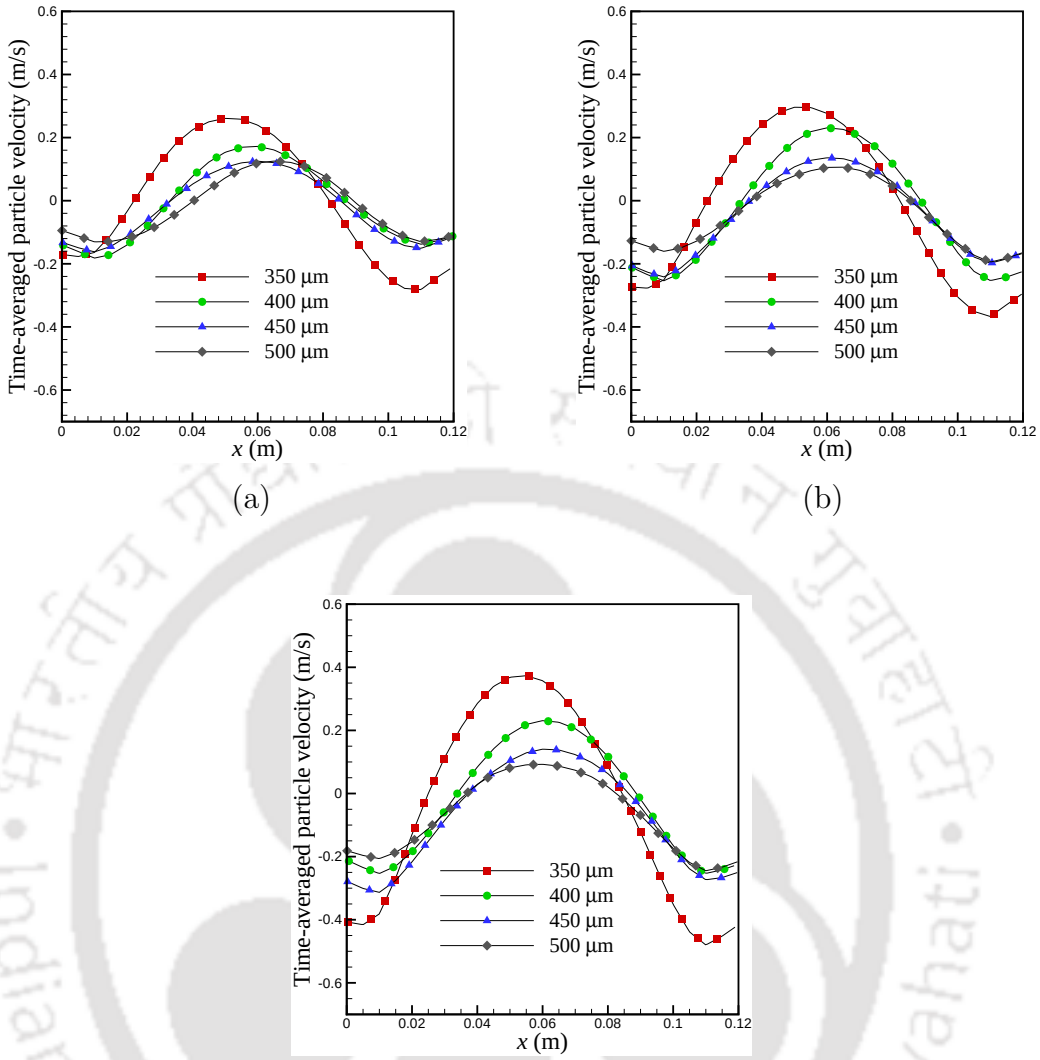

Figure 7.8: Plots of time-averaged particle velocity profiles for four values of particle diameter at (a) h=0.2 m, (b) h=0.3 m and (c) h=0.4 m.

values of the time-averaged particle velocity can be observed with increase in particle diameter.

It can also be observed from Figs. 7.8 (a), (b) and (c) that for any particular value of particle diameter, the magnitude of maximum time-averaged particle velocity increases gradually from the section h=0.2 m to the section h=0.4 m, i.e., the magnitude of maximum value of time-averaged particle velocity obtained at a

Table 7.4: Maximum value of time-averaged particle velocity inside the domain for different values of particle diameter

Particle diameter (μm)	Max. time avg. particle velocity (m/s)
300	0.56
350	0.387
400	0.232
450	0.1533
500	0.1269

particular section increases with increase in height. However, this variation in the time-averaged particle velocity with height inside the channel becomes less prominent with increase in particle diameter, as observed in Fig. 7.8. Moreover, it is worth noting that the time-averaged particle velocity profiles at any section inside the channel become more symmetric as the value of particle diameter increases.

7.5 Effects on time-averaged particle phase volume fraction profiles

The corresponding particle phase volume fraction profiles for different particle diameters at the same three sections of the channel have been plotted in Figs. 7.9 (a), (b) and (c). It can be observed that like time-averaged particle velocity profiles, there is noticeable variations in the time-averaged volume fraction profiles at any section inside the channel with change in particle diameter. At a particular section inside the fluidization zone, the maximum value of time-averaged volume fraction has been observed for the highest diameter particles and vice-versa. It is due to the reason that as observed in Section 7.4, the time-averaged particle velocity is minimum for the particles with maximum value of diameter at any section inside the fluidization zone. Due to this lower velocity, the accumulation of the higher diameter particles at any section is more than the lower diameter particles which results in higher values

of time-averaged volume fractions for higher diameter particles at any section inside the channel.

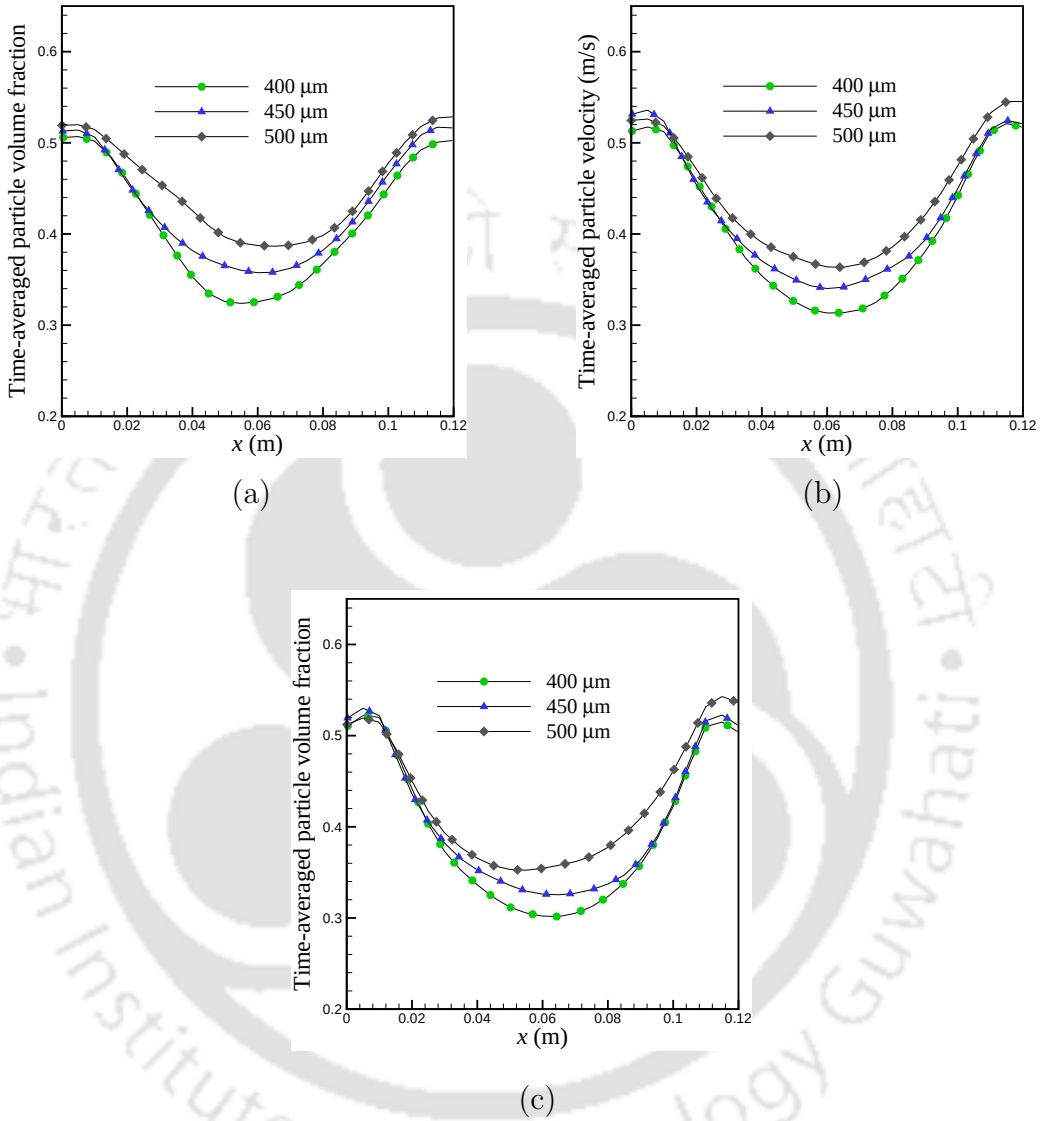

Figure 7.9: Plots of time-averaged particle volume fraction profiles for three values of particle diameter at (a) h=0.2 m, (b) h=0.3 m and (c) h=0.4 m.

Also, it can be observed from Fig. 7.9 that for a particular diameter, the volume fraction near the vertical centerline (x=0.06 m) is maximum at lower sections (close to inlet) of the channel and it decreases continuously at the sections which are at a greater height inside the fluidization zone. In other words, as seen in Fig. 7.9,

the magnitude of time-averaged particle phase volume fraction is maximum at the section h=0.2 m and minimum at the section h=0.4 m. However, this variation of time-averaged volume fractions with height is more pronounced for higher diameter particles (specially for 500 μm). The reason for this variation is due to the fact that higher diameter particles tend to settle more at the lower sections as seen in Fig. 7.7 and so, volume fraction for higher diameter particles increases at the lower sections inside the fluidization zone.

7.6 Closure

In this chapter, the applicability of the flow solver in the simulations of gas-particulate flows in bubbling gas-solid fluidized beds is tested. Two validation studies, including comparisons from available numerical and experimental results, are presented. Investigations have been carried out on the effects of particle diameter on the time-averaged particle velocity and volume fraction profiles at different sections inside the fluidized bed reactor. The time-averaged particle velocity at any section inside the fluidization zone has been found to decrease while the time-averaged particle phase volume fraction at any section has been found to increase with increase in particle diameter.

Chapter 8

Conclusions and scope of future work

8.1 Conclusions

This thesis presents the details of the development of a finite volume method based numerical flow solver to simulate gas-particulate flows using Eulerian-Eulerian two-fluid model on collocated grid arrangement. The solver which is capable of handling both orthogonal and non-orthogonal meshes is developed in such a manner that it can handle all conditions ranging from dilute to dense gas-particulate flows. A detailed discussion on the discretization procedure and solution methodology has been carried out with an emphasis on the implementation aspects specific to gas-particulate flows along with the description of drag models and coupling approaches. Validations have been performed for one-way and two-way coupling for dilute flow conditions in the initial phase of the work. Subsequently, the solver is modified to handle non-dilute flows as well as to account for particle-particle and particle wall interactions using the KTGF model. Two major concerns in numerical implementation of such flows pertain to the derivation of pressure equation and keeping the particle phase volume fraction within the packing limit. The pressure equation has been derived from the global continuity equation obtained by adding the continuity equations of both the phases, following the the idea of Moukalled et al. [32]. Frictional stress model has been added to the solver in combination with KTGF in order to keep the particle phase volume fractions within the packing limit even in

closely packed flow situations. A detailed validation at all stages of development (including comparisons from Ansys Fluent) for different problems available in the literature are performed and the results show a reasonably good agreement with the published data.

The flow solver is subsequently applied for parametric studies in three different flow scenarios and finally applied to the preliminary studies on the flow hydrodynamics inside bubbling gas-solid fluidized beds.

A parametric study of dispersed laminar gas-particle flows through vertical and horizontal channels has been carried out considering a two-way coupling between the phases. The effects of particle diameter (Stokes number), inlet particle phase volume fraction and 'inlet slip' between the phases on the hydrodynamics have been elaborately discussed. The salient conclusions which can be drawn from this study are summarized below.

- With increase in particle diameter, the maximum velocity attained by the particles inside the channel decreases. This is due to the fact that larger diameter particles experience a higher inertia and gravitational force in comparison to the interphase drag than the smaller diameter particles with same material density.
- The corresponding maximum steady state gas velocities are found to increase marginally with increase in particle diameter when all other parameters are kept invariant. The reason behind this increase is the decrease of particle velocity with particle diameter which in turn reduces the retarding drag force exerted by the particles on the gas phase.
- The steady state gas velocity at a particular section decreases with increase in the inlet particle phase volume fraction. It is due to the increase of retarding interphase drag force acting on the gas phase exerted by the particles with increase in particle volume fractions, which tend to lower the gas velocity at any section of the channel.
- 'Inlet slip' (or difference of inlet phase velocities) also have a significant effect on steady state phase velocity and volume fraction profiles. When $u_g > u_s$ (u_g=1 m/s and u_s=0.5 m/s) at inlet, steady state gas velocity at any section

inside the channel is less than its corresponding value when both the phases enter with the same inlet velocity (u_g=1 m/s and u_s=1 m/s). So, in this case, the gas volume fraction at a particular section increases such that at steady state, the net mass flow rate remains constant at all the sections and equal to the value at inlet. On the other hand, when $u_s > u_g$ at inlet, steady state particle velocity at any section inside the channel is less than its corresponding value when both the phases enter with the same inlet velocity. As a result, the particle volume fraction at a particular section increases in this case such that at steady state, the net particle mass flow rate remains constant at all the sections and equal to the value at inlet.

Investigations have also been carried out to find out the effects of three-way coupling which involves the effects of particle-particle and particle-wall interactions on dispersed gas-particle flows through horizontal channels. The effects on steady state phase velocities and volume fraction profiles due to the variation in the value of ϕ at a particular value of e have been studied and vice-versa. The main conclusions of this study are summarized as follows.

- At a particular value of e, both the particle phase and gas phase velocity near the wall is maximum for ϕ=0. The magnitude of both the velocities near the wall decreases with increase in the value of ϕ. On the other hand, near the centerline of the channel, the maximum value of velocity attained by both the phases increases with increase in the value of ϕ at a particular value of e. For ϕ=0, the volume fraction is maximum near the wall and it decreases with increase in the value of ϕ. For non-zero values of ϕ, significant variations in the particle phase volume fraction profiles can be observed, at a particular value of e.

- At a particular non-zero value of ϕ, the maximum steady state velocity attained by both the phases increases with increase in the value of e. But for ϕ=0; there is no significant variation in phase velocities as well as particle phase volume fraction profiles with change in the value of e. Like gas and particle velocity, for a non-zero value of ϕ, significant variations in particle phase volume fraction profiles can be observed with change in e.

- The value of average wall shear stress for the particle phase increases with increase in the value of ϕ whereas, for the gas phase, it decreases with increase

in the value of ϕ.

- The study carried out for various combinations of values of ϕ and e indicate that the magnitude of the maximum phase velocity of each individual phase obtained inside the channel shows a direct dependence on both ϕ and e and tend to be maximum when both the values of ϕ and e are maximum.

Similarly, the effects of particle-particle and particle-wall interactions on the recirculation characteristics of dispersed gas-particle flows through a sudden expansion have been studied. The changes in the recirculation lengths occurring due to the changes in the values of ϕ and e have been investigated. The main findings of this study are listed below.

- At a particular value of ϕ, for all other parameters being invariant, the length of the recirculation zone tends to increase with decrease in the value of e. In other words, for the values of e investigated herein, the length of the recirculation zone is found to be the lowest when the value of e is 0.99 (close to unity, corresponding to perfectly elastic collisions) and highest when the value of e is equal to 0.8. The co-ordinates of the vortex eye also show a significant shift upwards and towards the right with variation of e, at a particular value of ϕ.

- For a particular value of e, as the value of ϕ is varied from zero (free-slip boundary condition for particle velocity) to unity (no-slip condition for particle velocity), one can observe that there is a gradual increase in the recirculation length with increase in the value of ϕ although this change is not as significant as the one observed with change in e, for a given value of ϕ.

- Of the various combinations of values of ϕ and e studied, the length of the recirculation zone is found to be maximum when the value of ϕ is maximum and the value of e is minimum while the length of the recirculation zone is minimum when the value of ϕ is minimum and that of e is maximum.

Preliminary studies have been conducted in order to investigate the effects of variation of particle diameter (Stokes number) on the overall fluidization characteristics of a bubbling gas-solid fluidized bed reactor. The effects of change of particle diameter on the time-averaged particle velocity and volume fraction profiles have been studied at different sections of the bed keeping all other parameters invariant. The following conclusions can be drawn from this study.

- Particle diameter (Stokes number) has a significant effect on the fluidization characteristics of gas-solid bubbling fluidized beds even when all other parameters remain invariant.

- The time-averaged particle velocity at any section inside the fluidization zone tend to increase with decrease in the particle diameter. The reason for this can be attributed to the fact that the lower diameter particles are more readily influenced by the interphase momentum exchanges and changes in the gas phase velocity fields than the higher diameter particles.

- For a certain value of particle diameter, the magnitude of maximum time-averaged particle velocity has been found to increase gradually from the sections at lower heights (close to inlet) to the sections at higher heights inside the channel. However, this variation in the time-averaged particle velocity with height inside the channel becomes less prominent with increase in particle diameter.

- The time-averaged particle phase volume fraction at any section inside the fluidization zone tend to increase with increase in the particle diameter. This is due to the lower value of time-averaged particle velocity of higher diameter particles which results in the higher rate of accumulation of particles at any section inside the channel.

8.2 Scope of future work

Although the present work provides details of the development of a numerical flow solver for gas-particulate flows and its application to different flow scenarios, there exist many directions which can be explored in near future. A few of the research possibilities have been summarized below.

- The present solver can handle only isothermal flow situations. So, in order to simulate non-isothermal two phase flows, additional equations for conservation of energy for both the phases need to be implemented in addition to the present governing equations considered in this work.
- The present solver can be used to simulate gas-droplet flows if in addition to the energy equations of both the phases, mass transfer effects are also taken into account. The evaporation of the droplets under different flow conditions can then be studied using the flow solver.
- The studies on fluidized beds have been carried out primarily in case of two-dimensional bubbling gas-solid fludized beds. More realistic simulations in three-dimensions including turbulent flow conditions will necessitate the inclusion of turbulence models and their validation. Such an implementation will make the solver more useful in simulating problems of practical importance and may later also be extended to handle other types of fluidized beds such as circulating fluidized beds where the flows inside the reactor are predominantly turbulent.
- The development of the present gas-particulate flow solver has been done in a serial manner. Handling complex three-dimensional industrial flow problems will necessitate the use of much larger meshes and an inherently parallel framework. Parallelizing the gas-particulate flow solver is therefore may be the research effort of immediate importance and may be undertaken in the near future.

References

[1] Ishii M. and Hibiki T., *Thermo-Fluid dynamics of two-phase flow* (Springer, 1975).

[2] Starkey T.V. (1956) 'The laminar flow of stream of suspended particles', *British Journal of Applied Physics*, vol. 7, pp. 52–55.

[3] Booras G.S. and Krantz W.B. (1976) 'Dispersion in the laminar flow of power-law fluids through straight tubes', *Industrial and Engineering Chemistry Fundamentals*, vol. 15(4), pp. 249–253.

[4] Sinclair J.L. and Jackson R. (1989) 'Gas-particle flow in vertical pipe with particle-particle interactions', *AIChE Journal*, vol. 35, pp. 1473–1481.

[5] Kashinsky O.N., Timkin L.S., and Cartellier A. (1993) 'Experimental study of "laminar" bubbly flows in a vertical pipe', *Experiments in Fluids*, vol. 14, pp. 308–314.

[6] Nakoryakov V.E., Kashinsky O.N., Randin V.V., and Timkin L.S. (1996) 'Gas-liquid bubbly flow in vertical pipes', *Journal of Fluid Engineering*, vol. 118, pp. 377–382.

[7] Luo R., Pan X.H., and Yang X.Y. (2003) 'Laminar light particle and liquid two phase flows in a vertical pipe', *International Journal of Multiphase Flows*, vol. 29, pp. 603–620.

[8] Schindler M., Talkner P., Kostur M., and Hanggi P. (2007) 'Accumulating particles at the boundaries of a laminar flow', *Physica*, vol. 385, pp. 46–58.

[9] Tsuji Y. (2007) 'Multi-scale modelling of dense phase gas-particle flow', *Chemical Engineering Science*, vol. 62, pp. 3410–3418.

[10] Crowe C., Schwarzkopf J., Sommerfeld M., and Tsuji Y., *Multiphase Flows with Droplets and Particles* (CRC Press, 2012).

[11] Elghobashi S. (1994) 'On predicting particle-laden turbulent flows', *Applied Scientific Research*, vol. 52, pp. 309–329.

[12] Loth E. (2000) 'Numerical approaches for motion of dispersed particle, droplets and bubbles', *Progress in Energy and Combustion Science*, vol. 26, pp. 161–223.

[13] Tu J.Y. and Fletcher C. (1995) 'Numerical computation of turbulent gas-solid particle flow in a 90^0 bend', *AIChE Journal*, vol. 41(10), pp. 2187–2197.

[14] Johnson P. and Jackson R. (1987) 'Frictional-collisional constitutive relations for granular materials, with application to plane shearing', *Journal of Fluid Mechanics*, vol. 176, pp. 67–93.

[15] der Hoef M.A.V., Ye M., van Sint Annaland M., Andrews A.T., Sundaresan S., and Kuipers J.A.M. (2006) 'Multiscale modeling of gas-fluidized beds', *Advances in Chemical Engineering*, vol. 31, pp. 65–149.

[16] Geldart D. (1973) 'Types of gas fluidization', *Powder Technology*, vol. 7(5), pp. 285–292.

[17] Loha C., Chattopadhyay H., and Chatterjee P. (2012) 'Assessment of drag models in simulating bubbling fluidized bed hydrodynamics', *Chemical Engineering Science*, vol. 75, pp. 400–407.

[18] Mohanarangam K., Tian Z.F., and Tu J.Y. (2007) 'Numerical gas-particle flow in a 90^0 bend: comparison of two particle modeling approach', *ANZIAM*, vol. 48, pp. C741–C758.

[19] Shirolkar J.S., Coimbra C., and McQuay Q. (1996) 'Fundamental aspects of modeling turbulent particle dispersion in dilute flows', *Progress in Energy and Combust Science*, vol. 22(10), pp. 363–399.

[20] Danon H., Wolpshtein M., and Hetsroni G. (1977) 'Numerical calculations of two-phase turbulent round jet', *International Journal of Multiphase flow*, vol. 3(1), pp. 223–234.

[21] Chen P. and Wood P. (1990) 'Turbulent closure modeling for dilute gas-particle flows', *The Canadian Journal of Chemical Engineering*, vol. 63, pp. 349–359.

[22] Mostafa A.A. and Mongia H.C. (1988) 'On the interaction of particles and turbulent fluid flow', *International Journal of Heat and Mass Transfer*, vol. 31(10), pp. 2063–2075.

[23] Shuen J., Solomon A., Zhang Q., and Faeth G. (1985) 'Structure of particle-laden jets: Measurements and predictions', *AIAA Journal*, vol. 23(3), pp. 396–404.

[24] Mostafa A. and Eglobashi S. (1985) 'A two-equation turbulence model for jet flows laden with vaporizing droplets', *International Journal of Multiphase Flow*, vol. 11(4), pp. 515–533.

[25] Chen C. and Wood P. (1986) 'Turbulence closure modelling of the dilute gas-particle axisymmetric jet', *AIChE Journal*, vol. 32, pp. 163–166.

[26] Tu J.Y. and Fletcher C.A. (1994) 'An improved model for particlulate turbulence modulation in confined two-phase flows', *International Communications in Heat and Mass Transfer*, vol. 21(6), pp. 775–783.

[27] Tsuji Y., Morikawa Y., and Shinomi T. (1984) 'LDV measurements of air-solid two-phase in a vertical pipe', *Journal of Fluid Mechanics*, vol. 139, pp. 417–434.

[28] Kliafas Y. and Holt M. (1987) 'LDV measurements of a turbulent air-solid two-phase flow in a 90^0 bend', *Experiments in Fluids*, vol. 5, p. 73.

[29] Tu J.Y. (1997) 'Computation of turbulent two-phase flow on overlapped grids', *Numerical Heat Transfer, Part B*, vol. 32(B), pp. 175–195.

[30] Enwald H., Peirano E., and Almstedt A. (1997) 'Eulerian two-phase flow theory applied to fluidization', *International Journal of Multiphase Flow*, vol. 22, pp. 21–66.

[31] Ferry J. and Balachandar S. (2001) 'A fast Eulerian method for disperse two-phase flow', *International Journal of Multiphase Flow*, vol. 27, pp. 1199–1226.

[32] Moukalled F., Darwish M., and Sekar B. (2003) 'A pressure-based algorithm for multi-phase flow at all speeds', *Journal of Computational Physics*, vol. 190, pp. 550–571.

[33] Tian Z.F., Tu J.Y., and Yeoh G.H. (2005) 'Numerical simulation and validation of dilute gas-particle flow over a backward-facing step', *Aerosol Science and Technology*, vol. 39, pp. 319–332.

[34] Mohanarangam K., Tian Z.F., and Tu J.Y. (2008) 'Numerical simulation of turbulent gas-particle flow in a 90^0 bend: Eulerian-Eulerian approach', *Computers and Chemical Engineering*, vol. 32, pp. 561–571.

[35] Benavides A. and Watchem B. (2009) 'Eulerian-Eulerian prediction of dilute turbulent gas-particle flow in a backward facing step', *International Journal of Heat and Fluid Flow*, vol. 30, pp. 452–461.

[36] Akbarinia A. and Laur R. (2009) 'Investigating the diameter of solid particles effects on a laminar nanofluid flow in a curved tube using a two phase approach', *International Journal of Heat and Fluid Flow*, vol. 30, pp. 706–714.

[37] Kalteh M., Abbassi A., Aval M.S., and Harting J. (2011) 'Eulerian-Eulerian two-phase numerical simulation of nanofluid laminar forced convection in a microchannel', *International Journal of Heat and Fluid Flow*, vol. 32, pp. 107–116.

[38] Barton I.E. (1996) 'Computation of dilute particulate laminar flow over a backward facing step', *International Journal for Numerical Methods in Fluids*, vol. 22, pp. 211–221.

[39] Barton I.E. (1994) 'Laminar flow past an enclosed and open backward facing step', *Physics of Fluids*, vol. 6, pp. 4054–4056.

[40] Barton I.E. (1996) 'Exponential lagrengian tracking schemes applied to stokes law', *Journal of Fluids Engineering*, vol. 118, pp. 85–89.

[41] Barton I.E. (1997) 'Laminar flow over a backward-facing step with a stream of hot particles', *International Journal of Heat and Fluid Flow*, vol. 18(4), pp. 400–410.

[42] Yu K., Lau K., and Chan C. (2004) 'Numerical simulation of gas-particle flow in a single-side backward-facing step flow', *Journal of Computational and Applied Mechanics*, vol. 163, pp. 119–129.

[43] Passalacqua A. and Fox R. (2011) 'Advanced continuum modelling of gas-particle flows beyond the hydrodynamic limit', *Applied Mathematical Modelling*, vol. 35, pp. 1616–1627.

[44] Passalacqua A., Fox R., Garg R., and Subramaniam S. (2010) 'A fully coupled quadrature-based moment method for dilute to moderately dilute fluid-particle flows', *Chemical Engineering Science*, vol. 40, pp. 2267–2283.

[45] Zhao L.H., Marchioli C., and Andersson H.I. (2012) 'Stokes number effects on particle slip velocity in wall-bounded turbulence and implications for dispersion models', *Physics of Fluids*, vol. 24, p. 021705.

[46] Deshmukh A., Vasava V., Patankar A., and Bose M. (2016) 'Particle velocity distribution in a flow of gas-solid mixture through a horizontal channel', *Powder Technology*, vol. 298, pp. 119–129.

[47] Sommerfeld M. and Kussin J. (2004) 'Wall roughness effects on pneumatic conveying of spherical particles in a narrow horizontal channel', *Powder Technology*, vol. 142, pp. 180–192.

[48] Lain S. and Sommerfeld M. (2008) 'Euler/Lagrange computations of pneumatic conveying in a horizontal channel with different wall roughness', *Powder Technology*, vol. 184, pp. 76–88.

[49] Zhu K., Wong C.K., Rao S.M., and Wang C.H. (2004) 'Pneumatic conveying of granular solids in horizontal and inclined pipes', *AIChE Journal*, vol. 50, pp. 1729–1745.

[50] Eskin D. (2005) 'Modeling dilute gas-particle flows in horizontal channels with different wall roughness', *Chemical Engineering Science*, vol. 60, pp. 655–663.

[51] Soleimania A., Schneiderbauera S., and Pirkera S. (2015) 'CFD study of the gas-particle flow in a horizontal duct: the impact of the solids wall boundary conditions', *Procedia Engineering*, vol. 102, pp. 1026–1037.

[52] Li T. and Benyahia S. (2012) 'Revisiting Johnson and Jackson boundary condition for granular flows', *AIChE Journal*, vol. 58(7), pp. 2058–2068.

[53] Li X., Lv S., and Liu Y. (2013) 'Effects of particleparticle collisions on sudden expansion gas-particle flows via a two-phase kinetic energy-particle temperature model', *Advanced Powder Technology*, vol. 24, pp. 98–105.

[54] Zhao Y., Ding T., Zhu L., and Zhong Y. (2016) 'A specularity coefficient model and its application to dense particulate flow simulations', *Industrial and Engineering Chemistry Research*, vol. 55, pp. 1439–1448.

[55] Arefmanesh A. and Michaelides E. (1988) 'Pressure changes at a sudden expansion in gas-solid flows', *Particulate Science and Technology*, vol. 6(3), pp. 333–341.

[56] Ruck B. and Makiola B. (1988) 'Particle dispersion in a single-sided backward-facing step flow', *International Journal of Multiphase Flows*, vol. 14(6), pp. 787–800.

[57] Fessler J.R. and Eaton J.K. (1999) 'Turbulence modification by particles in a backward-facing step flow', *Journal of Fluid Mechanics*, vol. 394, pp. 97–117.

[58] Terekhov V. and Pakhomov M. (2008) 'Turbulent gas-dispersed flow in a pipe with sudden expansion: numerical simulation', *Thermophysics and Aeromechanics*, vol. 15(4), pp. 589–601.

[59] Terekhov V. and Pakhomov M. (2015) 'Numerical simulation of turbulent swirling gas-dispersed flow behind a sudden tube expansion', *Thermophysics and Aeromechanics*, vol. 22(5), pp. 597–608.

[60] Gundogdu M.Y., Kutlar A.I., and Duz H. (2009) 'Analytical prediction of pressure loss through a sudden-expansion in two-phase pneumatic conveying lines', *Advanced Powder Technology*, vol. 20, pp. 48–54.

[61] Mohanarangam K., Tu J.Y., and Chen L. (2008) 'Numerical study of particle dispersion behind a sudden expansion geometry and its effect on step heights', *Computers and Chemical Engineering*, vol. 32, pp. 3187–3197.

[62] Mergheni M.A., Sautet J.C., Ticha H.B., and Nasrallah S.B. (2012) 'Numerical simulation of sudden-expansion particle-laden flows using the Eulerian-Lagrangian approach', *Thermal Science*, vol. 16(4), pp. 1005–1012.

[63] Love A.I.J., Giddings D., and Power H. (2014) 'Numerical analysis of particle flows within a double expansion', *Powder Technology*, vol. 266, pp. 22–37.

[64] Chisea M., Mahisen V., Melheim J., and Halvorsen B. (2005) 'Numerical simulation of particle flow by Eulerian-Eulerian and Eulerian-Lagrengian approach with application to fluidized bed', *Computers and Chemical Engineering*, vol. 29, pp. 291–304.

[65] Deardorff J.W. (1971) 'On the magnitude of the subgrid scale eddy coefficient', *Journal of Computational Physics*, vol. 7(1), pp. 120–133.

[66] Lindborg H., Lysberg M., and Jakobsen H. (2007) 'Practical validation of the two-fluid model applied to dense gas-solid flows in fluidized beds.', *Chemical Engineering Science*, vol. 62, pp. 5854–5869.

[67] Spalding D.B. (1980) 'Numerical computation of multi-phase fluid flow and heat transfer', *Recent Advances in Numerical Methods in Fluids*, vol. 1, pp. 139–167.

[68] Duarte C., Olazar M., Murata V., and Barrozo M. (2008) 'Numerical simulation and experimental study of fluid-particle flows in a spouted bed', *Powder Technology*, vol. 188, pp. 195–205.

[69] Wachem B., Schouten J., Krishna R., and Vandenbleek C. (1999) 'Validation of the Eulerian simulated dynamic behaviour of gas-solid fluidized beds', *Chemical Engineering Science*, vol. 54, pp. 2141–2149.

[70] Taghipour F., Ellis N., and Wong C. (2005) 'Experimental and computational study of gas-solid fluidized bed hydrodynamics', *Chemical Engineering Science*, vol. 60, pp. 6857–6867.

[71] Passalacqua A. and Marmo L. (2009) 'A critical comparison of frictional stress models applied to the simulation of bubbling fluidized beds', *Chemical Engineering Science*, vol. 160, pp. 2795–2806.

[72] Benyahia S., Syamlal M., and O'Brien T. (2007) 'Study of the ability of multiphase contiuum models to predict core-annulus flow', *AIChE Journal*, vol. 53, pp. 2549–2568.

[73] Loha C., Chattopadhyay H., and Chatterjee P. (2013) 'Euler-Euler CFD modeling of fluidized bed: Influence of specularity coefficient on hydrodynamic behavior', *Particuology*, vol. 11, pp. 673–680.

[74] Loha C., Chattopadhyay H., and Chatterjee P. (2014) 'Effect of coefficient of restitution in Euler-Euler CFD simulation of fluidized-bed hydrodynamics', *Particuology*, vol. 15, pp. 170–177.

[75] Verma V., Padding J.T., Deen N.G., and Kuipers J.A.M. (2015) 'Effect of bed size on hydrodynamics in 3-D gassolid fluidized beds', *AIChE Journal*, vol. 61(5), pp. 1492–1506.

[76] Zinani F., Philippsen C., and Indrusiak M. (2016) 'Numerical study of gas-solid drag models in a bubbling fluidized bed', *Particulate Science and Technology*, vol. 36(1), pp. 1–10.

[77] Alamolhoda F., Zarghami R., Sotudeh-Gharebagh R., and Mostoufi N. (2017) 'Effect of changes in particle size on the hydrodynamics of gas-solid fluidized beds through wall vibration', *Powder Technology*, vol. 307, pp. 129–136.

[78] 'www.ansys.com/products/fluids/ansys-fluent', .

[79] 'OpenCFD, OpenFOAM–the open source CFD Toolbox–user's guide, 1st Edition, OpenCFD Ltd.', *United Kingdom, 2010*.

[80] Syamlal M., Rogers W.R., and Brian T.J.O. (1993) 'MFIX Documentation: Theory guide, tech. rep.', *US Department of Energy*.

[81] Jackson R. (1997) 'Locally averaged equations of motion for a mixture of identical spherical particles and a newtonian fluid', *Chemical Engineering Science*, vol. 52(15), pp. 2457–2469.

[82] Lun C., Savage S., and Chepurning N. (1984) 'Kinetic theories for granular flow: Inelastic particles in Couette flow and singly inelastic particles in a general flow field', *Journal of Fluid Mechanics*, vol. 140, pp. 223–237.

[83] van Wachem B.G.M., Schouten J.C., and van der Bleek C.M. (2001) 'Comparative analysis of CFD models of dense gas-solid systems', *AIChE Journal*, vol. 47(5), pp. 1035–1050.

[84] Mineto A.T., de Souza Braun M.P., Navarro H.A., and Cabezas-Gomez L. (2014) 'Influence of the granular temperature in the numerical simulation of gas-solid flow bubbling fluidized bed', *Chemical Engineering Communications*, vol. 201, pp. 1003–1020.

[85] Syamlal M. (1998) 'MFIX documentation numerical technique', *Technical Report, U. S. Department of Energy, Morgantown Energy Technology Center*.

[86] Gidaspow D., *Multiphase Flow and Fluidization: Continuum and Kinetic Theory Descriptions* (Academy Press, 1994).

[87] Hrenya C.M. and Sinclair J.L. (1997) 'Effects of particle-phase turbulence in gas-solid flows', *AIChE Journal*, vol. 43, pp. 853–859.

[88] Liu Y. and Hinrichsen O. (2014) 'CFD modeling of bubbling fluidized beds using openFOAM : Model validation and comparison of TVD differencing schemes', *Computers and Chemical Engineering*, vol. 75-88, pp. 19–50.

[89] Schaeffer D.G. (1987) 'Instability in the evolution equations describing incompressible granular flow', *Journal of Differential Equations*, pp. 19–50.

[90] Syamlal M. and O'Brien T. (1989) 'Computer simulation of bubbles in a fluidized bed.', *AIChE symposium series*, vol. 85, pp. 22–31.

[91] Mckeen T. and Pugsley T. (2003) 'Simulation and experimental validation of a freely bubbling bed of FCC catalyst', *Powder Technology*, vol. 129, pp. 139–152.

[92] Kolev N.I., *Multiphase Flow Dynamics* (Springer, 2005).

[93] Wen C.Y. and Yu Y.H. (1966) 'Mechanics of fluidization', *Chemical Engineering Programme Symposium Series*, vol. 62, pp. 100–111.

[94] Visuri O., Wierink G.A., and Alopaeus V. (2012) 'Investigation of drag models in CFD modeling and comparison to experiments of liquid-solid fluidized systems', *International Journal of Mineral Processing*, vol. 104, pp. 58–70.

[95] GAMBIT (2004) 'Gambit 2.2 user's guide', *Fluent Inc., Lebanon, NH,*.

[96] Rhie C.M. and Chow W.L. (1983) 'Numerical study of the turbulent flow past an airfoil with trailing edge seperation', *AIAA Journal*, vol. 21, pp. 1525–1532.

[97] Dalal A., Eswaran V., and Biswas G. (2008) 'A finite-volume method for Navier-Stokes equation on unstructured meshes', *Numerical Heat Transfer,Part B*, vol. 54(2), pp. 238–259.

[98] Khosla P.K. and Rubin S.G. (1974) 'A diagonally dominated second order accurate implicit scheme', *Computers and Fluids*, vol. 2, pp. 207–209.

[99] Perot B. (2000) 'Conservation properties of unstructured staggered mesh schemes', *Journal of Computational Physics*, vol. 159, pp. 58–89.

[100] Manik J. (2017) 'Well-balanced and consistent algorithms for three-dimensional simulations of binary immiscible flows', *PhD thesis, Department of Mechanical Engineering, IIT Guwahati*.

[101] LIS (2005) 'Library of Iterative Solvers for Linear Systems, lis user guide', *www.ssisc.org/lis*.

[102] Dasgupta A.K. (2008) 'Numerical simulation of dilute gas-particle flows using an Eulerian-Eulerian approach', *M. Tech thesis, Department of Mechanical Engineering, IIT Kanpur*.

[103] Passalacqua A. and Fox R.O. (2011) 'Implementation of an iterative solution procedure for multi-fluid gas-particle flow models on unstructured grids', *Powder Technology*, vol. 213, pp. 174–187.

[104] Gelderbloom S., Gidaspow D., and Lyczkowski R. (2003) 'CFD simulations of bubbling/collapsing fluidized beds for three Geldart groups', *AIChE Journal*, vol. 49, pp. 844–858.

[105] Jung J., Gidaspow D., and Gamwo I. (2006) 'Bubble computation, granular temperatures, and Reynolds stresses', *Chemical Engineering Communications*, vol. 193, pp. 946–975.

[106] Jung J.H., Yoon H.S., Lee C.Y., and Shin S.C. (2012) 'Effect of the vertical baffle height on the liquid sloshing in a three-dimensional rectangular tank', *Ocean Engineering*, vol. 44, p. 7989.

LIST OF PUBLICATIONS

International Journal

- **Kotoky, S.**, Dalal, A., and Natarajan, G., 2018, A parametric study of dispersed laminar gas-particle flows through vertical and horizontal channels, Advanced Powder Technology, vol. 29 (5), pp. 1072-1084.

- **Kotoky, S.**, Dalal, A., and Natarajan, G., 2018, Effects of specularity and particle-particle restitution coefficients on the hydrodynamic behavior of dispersed gas-particle flows through horizontal channels, Advanced Powder Technology, vol. 29(4), pp. 874-889.

- **Kotoky, S.**, Dalal, A., and Natarajan, G., Effects of Specularity and Particle-Particle Restitution Coefficients on the Recirculation Characteristics of Dispersed Gas-particle Flows Through a Sudden Expansion, Advanced Powder Technology (Accepted for publication).

- **Kotoky, S.**, Dalal, A., and Natarajan, G., Effects of particle diameter on the fluidization characteristics of bubbling gas-solid fluidized beds, (Manuscript under preparation, to be submitted to Particuology).

Book Chapter

- **Kotoky, S.**, Dalal, A., and Natarajan, G., 2017, Eulerian-Eulerian Modeling of Dispersed Laminar Gas-Particle Flows over an unstructured grid, Fluid Mechanics and Fluid PowerContemporary Research (Springer), 09/2017, pages 1101-1110; DOI; https://doi.org/10.1007/978-81-322-2743-4_104.

International Conference

- Manik, J., Parmananda, M., **Kotoky, S.**, Borgohain, P., Dalal, A. and Natarajan, G.,2017, Lessons from Anupravaha: Towards a General Purpose Computational Framework on Hybrid Unstructured Meshes for Multi-Physics Applications, Paper No. CHT-17-209, ICHMT International Symposium on Advances in Computational Heat Transfer, Napoli, Italy.

- **Kotoky, S.**, Dalal, A., and Natarajan, G., 2016, Numerical Study of Effects of Particle Diameter and Particle Volume Fractions on Dispersed Gas-Particle

Flows Through Vertical Channels, Paper No: 214, 6th International Congress on Computational Mechanics and Simulation, IIT Bombay, India.

- **Kotoky, S.**, Dalal, A., and Natarajan, G., 2015,Numerical Simulation of Laminar Gas- Particle Flow through a vertical channel and over a backward facing step , Paper No: F- FM-049, 68th Annual Session of Indian Institute of Chemical Engineers (CHEMCON conference 2015), IIT Guwahati, India.

- **Kotoky, S.**, Dalal, A., and Natarajan, G., 2014, Eulerian-Eulerian Modeling of Dispersed Laminar Gas-Particle Flows over an unstructured grid, Paper No: 522, 5th International and 41st National Conference on Fluid Mechanics and Fluid Power, IIT Kanpur, India.